FUNCTIONALIZED IRON OXIDE SUPPORTED ON GRAPHENE OXIDE FOR HYPERTHERMIA APPLICATION

UMAR AHMAD ABULFATHI

DISSERTATION SUBMITTED IN FULFILMENT OF THE REQUIREMENTS FOR THE DEGREE OF MASTER OF ENGINEERING SCIENCE

DEPARTMENT OF CHEMICAL ENGINEERING
FACULTY OF ENGINEERING
UNIVERSITY OF MALAYA
KUALA LUMPUR

2021

UNIVERSITY OF MALAYA

ORIGINAL LITERARY WORK DECLARATION

Name of Candidate: UMAR AHMAD ABULFATHI

Matric No: KGA180026 (17198353/01)

Name of Degree: Master of Engineering Science

Title of Project Paper/Research Report/Dissertation/Thesis ("this Work"):

FUNCTIONALIZED IRON OXIDE SUPPORTED ON GRAPHENE OXIDE FOR HYPERTHERMIA APPLICATION

Field of Study: Reaction Engineering

I do solemnly and sincerely declare that:

(1) I am the sole author/writer of this Work;
(2) This Work is original;
(3) Any use of any work in which copyright exists was done by way of fair dealing and for permitted purposes and any excerpt or extract from, or reference to or reproduction of any copyright work has been disclosed expressly and sufficiently and the title of the Work and its authorship have been acknowledged in this Work;
(4) I do not have any actual knowledge nor do I ought reasonably to know that the making of this work constitutes an infringement of any copyright work;
(5) I hereby assign all and every rights in the copyright to this Work to the University of Malaya ("UM"), who henceforth shall be owner of the copyright in this Work and that any reproduction or use in any form or by any means whatsoever is prohibited without the written consent of UM having been first had and obtained;
(6) I am fully aware that if in the course of making this Work I have infringed any copyright whether intentionally or otherwise, I may be subject to legal action or any other action as may be determined by UM.

Candidate's Signature Date: 11/06/2021

Subscribed and solemnly declared before,

Witness's Signature Date: 15/6/2021

Name:

Designation:

ABSTRACT

Cancer is one of the major causes of death globally (9.6 million in 2018). Magnetic hyperthermia therapy (MHT), a cancer therapy carried out at cellular level, has prospects in reducing these death rates. It is based on the concept that; magnetic nanoparticles (MNPs) deposited at cancer sites generate heat when exposed to an alternating current magnetic field and consequently destroy only the cancer cells by exploiting their vulnerability to heat. Thus, flaws like damage to healthy tissues and multidrug resistance associated with conventional treatments are avoided. As a challenge, using MNPs in their bare form can result in phagocytic capture, reducing their general tolerance in MHT. Henceforth, the surface of bare MNPs is modified. Unfortunately, such modification significantly reduces its heating efficiency, which implies a decline in MHT performance. This study curbed these challenges by fabricating a new magnetic hybrid nanostructure (MHNS); it mainly comprises Fe_3O_4 nanoparticle (FeNPs; one of the unique phases of MNPs), polyethylene glycol (PEG; a temperature-responsive surfactant) and graphene oxide (GO) nanoplatform. In a facile stagewise *ex-situ* approach, FeNPs was synthesized, functionalized with PEG (denoted as FAP), and finally grafted onto GO to form the MHNS. Optimizing the process by varying the composition loading reflects in the magnetic behavior; saturation magnetization values of 68.36, 60.89 and 40.76 emu/g were recorded for FeNPs, FAP and MHNS, respectively. All the VSM magnetization curves overlapped completely (S-shape), implying superparamagnetic behavior. Accordingly, these indicate successful functionalization and grafting. Interestingly, these indications also conform with the size increase (9.24, 11.97 and 12.25 nm, respectively) observed from XRD analysis and the detection of Fe, C, O and N elements by FESEM-EDX instrument. The presence of FeNPs in the synthesized products was affirmed by the consistent appearance of peculiar IR-band (around 550 – 578 cm^{-1} which was assigned to Fe – O vibration) in all the FTIR spectra. As aimed herein, the heating capacity of the

MHNS quantified by specific absorption rate (SAR) should be efficient. It was observed to depend on concentration, composition, viscosity, magnetic field strength and for the first time pH. Grafting functionalized FeNPs (FAP) onto GO nanoplatform (which supports clustering the FAP) at 4:1 ratio improved the heating efficiency by 1.7-fold; dispensed 2-fold heat at simulated tumor microenvironment pH (4.5 – 6.98) compared to healthy cells microenvironment pH (> 7); timely generate significant amount of heat for prolonged period and reached 10 ^{o}C maximum temperature rise at 1.5 mg/mL, 15 kA/m and 316 kHz. These introduced a smart self-control attribute that could only yield the required thermal sensitization. Lastly, the SAR-viscosity relationship shows that SAR only drops with intense rise in heating medium viscosity (760-fold) and remains roughly constant at lower viscosities (η < 34 mPa.s), an indication that the heating mechanism is dominated by Néel relaxation. This relationship implies that the MHNS can perform in complex media like lymph and Cerebro Spinal Fluid (η < 6 mPa.s). These results pave the way for fabricating new MHT materials, efficient at lower concentrations and cellular level pH.

Keywords: Fe_3O_4 synthesis, GO grafting, saturation magnetization, field-induced magnetic heating, SAR-pH dependence

ABSTRAK

Kanser adalah salah satu penyebab utama kematian global (9.6 juta pada tahun 2018). Terapi hipertermia magnetik (MHT), satu terapi kanser yang dilakukan pada peringkat sel, mempunyai potensi dalam mengurangkan kadar kematian ini. Terapi ini adalah berdasarkan konsep bahawa; nanopartikel magnetik (MNP) yang melekat pada lokasi barah dapat menghasilkan haba apabila terkena medan magnet arus bolak-balik dan akibatnya hanya memusnahkan sel-sel barah yang sensitif terhadap haba. Oleh yang demikian, kelemahan-kelemahan yang dikaitkan dengan rawatan konvensional seperti kerosakan pada tisu yang sihat dan ketahanan terhadap pelbagai ubat dapat dielakkan. Cabaran penggunaan MNP dalam bentuk asal adalah apabila ia dapat menyebabkan penangkapan fagosit yang mengurangkan toleransi umum partikel MNP dalam terapi MHT. Oleh sebab itu, permukaan MNP yang asal perlu diubah suai. Malangnya, pengubahsuaian sedemikian mengurangkan kecekapan pemanasan partikel MNP dengan ketara, seterusnya boleh mengakibatkan penurunan prestasi MHT. Untuk mengatasi cabaran ini, kajian ini menghasilkan struktur nano hibrid magnetik (MHNS) baru yang terdiri daripada nanopartikel Fe_3O_4 (FeNPs; salah satu fasa MNP yang unik), polietilena glikol (PEG; surfaktan hidrofilik peka suhu) dan nanoplatform grafena oksida (GO). Dalam pendekatan mudah berperingkat ex-situ, FeNP disintesis, difungsikan dengan PEG (dilambangkan sebagai FAP), dan akhirnya dicantumkan ke GO untuk membentuk MHNS. Mengoptimumkan proses dengan mengubah komposisi muatan mempengaruhi tingkah laku magnet material; dimana nilai magnetisasi tepu 68.36, 60.89 dan 40.76 emu/g masing-masing telah direkodkan untuk FeNP, FAP dan MHNS. Semua lengkung magnetisasi VSM didapati bertindih sepenuhnya (bentuk-S) yang menunjukkan tingkah laku superparamagnetik. Hal ini menunjukkan pemfungsian dan cantuman yang berjaya. Menariknya, petunjuk ini juga bertepatan dengan peningkatan saiz (masing-masing 9.24, 11.97 dan 12.25 nm) yang diperhatikan dari analisis XRD dan pengesanan elemen Fe, C,

O dan N oleh instrumen FESEM-EDX. Kehadiran FeNP dalam semua produk yang disintesis diperhatikan oleh penampilan jalur penyerapan unik yang konsisten di semua spektrum FTIR sekitar 550 dan 578 cm^{-1}. Seperti yang ditujukan di sini, kapasiti pemanasan MHNS yang diukur dengan kadar penyerapan tentu (SAR), haruslah efisien. Ia diperhatikan bergantung pada kepekatan, komposisi, kelikatan, kekuatan medan magnet dan untuk pertama kalinya bergantung pada pH. Melekatkan FeNP yang telah difungsikan (FAP) ke GO nanoplatform (yang menyokong pengelompokan FAP) pada nisbah 4:1 meningkatkan kecekapan pemanasan sebanyak 1.7 kali ganda; mengeluarkan haba 2 kali ganda pada pH persekitaran mikro tumor yang disimulasi (4.5 – 6.98) dibandingkan dengan pH persekitaran mikro sel yang sihat (> 7); menghasilkan lebih banyak haba untuk jangka masa yang panjang pada waktu yang tepat; dan mencapai kenaikan suhu maksimum 10 ºC pada 1.5 mg / mL, 15 kA / m dan 316 kHz. Ini memperkenalkan ciri-ciri kawalan diri pintar yang hanya dapat menghasilkan pemekaan terma yang diperlukan. Akhir sekali, hubungan SAR-kelikatan menunjukkan bahawa nilai SAR hanya berkurangan dengan peningkatan kuat pada kelikatan medium pemanas (760 kali ganda) dan kekal hampir tidak berubah pada kelikatan yang lebih rendah ($\eta <$ 34 mPa.s); seterusnya menjadi petunjuk bahawa mekanisme pemanasan didominasi oleh kelonggaran Néel. Ini membuktikan bahawa, MHNS dapat berfungsi dengan baik dalam media kompleks seperti limfa dan Cerebro Spinal Fluid ($\eta < 6$ mPa.s). Hasil kajian ini membuka jalan untuk pembuatan bahan MHT baru.

ACKNOWLEDGEMENTS

First and foremost, all praises and thanks be to ALLAH, the CHERISHER, the SUSTAINER, the PROVIDER for one and all, the one who gave me the opportunity to complete this work and overcome all the huddles on my path. I want to express utmost gratitude to my supervisors, Professor Dr. Wan Mohd Ashri Bin Wan Daud, Dr. Muhamad Fazly Bin Abdul Patah and my co-supervisor, Dr. Faisal Abnisa, for their guidance, patience, kindness, and encouragement; it is a privilege to have you all.

Many thanks to the technicians in the Department of Chemical Engineering: Mr. Muhammad Kamalrul Ariffin Bin Mohd Shariffuddin, Mr. Azaruddin Bin Ibrahim, Ms. Fazizah Binti Abdullah, and Ms. Azira Binti Idris. I also like to acknowledge the University of Malaya for supporting the work through "University of Malaya Research Grant" and "Fundamental Research Grant Scheme".

I am greatly indebted to my dear parent, Alh. Umar Hambali and Hajia Memunat Umar, your supply of prayers and parental care remain the best ever. My gratitude also goes to my siblings, Dr. Idris Umar Hambali, Engr. Dr. Hambali Umar Hambali, Shuaibu Umar Hambali and Saratu Umar Hambali, for their mentorship and family support. My special thanks to Ahmed Halilu and Abdulyekeen Kabir Abogunde; your brotherly and friendly contributions inspired me a lot. Finally, my appreciation goes to all my friends, colleagues, and well-wishers.

TABLE OF CONTENTS

LIST OF FIGURES

LIST OF TABLES

LIST OF SYMBOLS AND ABBREVIATIONS

ACMF	:	Alternating Current Magnetic Field
APTES	:	(3-Aminopropyl)triethoxysilane
DMDO	:	Dimethyl Sulfoxide
EDC	:	1-Ethyl-3-(3- dimethylaminopropyl)carbodiimide
f	:	Frequency
FA	:	Bare FeNPs modified with APTES
FAP	:	FA functionalized with PEG
FeNPs	:	Fe_3O_4 Nanoparticles
FESEM	:	Field Emission Scanning Electron Microscopy
FESEM-EDX	:	Field Emission Scanning Electron Microscopy with Energy Dispersive X-ray Spectroscopy
FTIR	:	Fourier-Transform Infrared Spectroscopy
GO	:	Graphene Oxide
H	:	Magnetic field strength (amplitude)
ILP	:	Intrinsic loss power
IONPs	:	Iron oxide nanoparticles
m	:	Mass fraction of FeNPs in the medium
MANPs		Magnetic alloy nanoparticles
MHNS	:	Magnetic Hybrid Nanostructure
MHT	:	Magnetic Hyperthermia Therapy
MMONPs	:	Magnetic Metal Oxide Nanoparticles
MNPs	:	Magnetic Nanoparticles
MRI	:	Magnetic Resonance Imaging
M_S	:	Saturation Magnetization

NHS	:	N-hydroxysuccinimide
NIR	:	Near-Infrared Radiation
NPs	:	Nanoparticles
PEG	:	Polyethylene Glycol
ROS	:	Reactive oxygen species
SAR	:	Specific absorption rate
SAR_f	:	*f* normalized SAR
SAR_H	:	*H* normalized SAR
SBF	:	Simulated Body Fluid
SDGs	:	Sustainable Development Goals
VSM	:	Vibrating Sample Magnetometer
XRD	:	X-ray Diffraction
C	:	Specific heat capacity

LIST OF APPENDICES

CHAPTER 1: INTRODUCTION

1.1 General Introduction

Cancer is the second major cause of death globally, with an estimate of 9.6 million deaths in the year 2018 (Wild, Weiderpass, & Stewart, 2020). The most affected sites include the lungs, breast and prostate (McGuire, 2016). Fortunately, it is not communicable like the deadly 2019 novel coronavirus disease (COVID-19) (Mbugua, Njenga, Odhiambo, Wandiga, & Onani, 2021). As a noncommunicable disease, the United Nations has a target within the Sustainable Development Goals (SDGs) agenda (Targe 3.4) to reduce the death rate by one-third by 2030 (Bennett et al., 2018). The availability of effective, efficient and affordable treatment is crucial in this regard (Wild et al., 2020).

Several conventional methods for treating cancer, such as chemotherapy, surgery, and radiation therapy, have many limitations (multidrug resistance, alopecia, fatigue and damage to healthy tissues). The fact that cancer cells are more vulnerable to high temperature compared with healthy cells led to the discovery of magnetic hyperthermia therapy (MHT); their susceptibility is primarily attributed to oxygen deficiency (hypoxia) caused by poor vasculature and blood flow (Beik et al., 2016; Field & Bleehen, 1979; H. Zhou et al., 2019). Consequently, thermal energy retained within the cancer cellular matrix denatures the proteins and inhibits its metabolism and proliferation (Field & Bleehen, 1979; Soukup, Moise, Céspedes, Dobson, & Telling, 2015; Sugumaran, Liu, Herng, Peng, & Ding, 2019). Unlike other conventional methods for treating cancer, MHT is carried out at a cellular level rather than a tissue or organ level. Thus, the therapy is not constrained by heat sink effects, tissue depth and hindrance or reflection of the heat by bone structures and hence provides more guided focus heating, which justifies its efficacy over conventional treatments (Beola, Gutiérrez, Grazú, & Asín, 2019; Pillai et al., 2015).

Magnetic hyperthermia therapy (Hyperthermia is a Greek-derived word: hyper means "over" and *thermē* means "heat") could be defined as the clinical use of heat to selectively halt or eradicate cancer cells without harming the neighboring healthy cells (Soleymani et al., 2020). It is achieved by control increase of temperature between 5 to 19 ^{o}C at the affected sites using magnetic nanoparticles (MNPs) and alternating current magnetic field (ACMF) to generate the heat and navigate the MNPs to the targeted cells (Albarqi et al., 2019). The temperature rise can either lead to thermal ablation (10 – 19 ^{o}C) or thermal sensitization (5 – 10 ^{o}C). The latter scenario is preferential for MHT (Albarqi et al., 2019; Alegret, Criado, & Prato, 2017; Ito et al., 2004; Andreas Jordan, Scholz, Wust, Schirra, et al., 1999; Nielsen, Horsman, & Overgaard, 2001; Wust et al., 2002). Thermoablation could yield widespread necrosis, coagulation, or carbonization depending on the precise temperature (Andreas Jordan, Scholz, Wust, Fähling, & Roland, 1999).

Generally, MHT is based on the concept that MNPs delivered at the affected site can generate heat when exposed to an ACMF and/or near-infrared radiation (NIR). In either case, MNPs are acting as the source of heat; when exposed to ACMF, they generate heat by absorbing radiofrequency power created by oscillating magnetic field through different mechanisms such as Brown relaxation, hysteresis loss, Néel relaxation and eddy current (Moroz, Jones, & Gray, 2002); while on exposure to NIR, heat is generated due to photothermal effect. ACMF has more profound penetration power than NIR. Alternatively, NIR may be applicable for patients with near surface tumors (Rodríguez-Rodríguez, Salas, & Arias-Gonzalez, 2020; Schrand, Stacy, Payne, Dosser, & Hussain, 2011; Shi, Sadat, Dunn, & Mast, 2015).

Experimentally, the heating performance of MNPs is quantified by a parameter called specific absorption rate (SAR); some authors also called it specific loss power, specific heat power, or specific power loss (Ganesan, Lahiri, Louis, Philip, & Damodaran, 2019;

R. Hergt et al., 2004; A. Jordan et al., 1993; Soetaert, Kandala, Bakuzis, & Ivkov, 2017; Wildeboer, Southern, & Pankhurst, 2014). SAR is defined as thermal energy generated per unit mass of MNPs (measured in Watt per gram). The magnitude of this parameter could be influenced by: MNPs properties such as saturation magnetization (M_S), surface chemistry and also heating parameters such as frequency and amplitude of the applied ACMF (Rudolf Hergt, Dutz, & Röder, 2008; R. Hergt et al., 2004; M. Ma et al., 2004; Urtizberea, Natividad, Arizaga, Castro, & Mediano, 2010).

MNPs are inorganic and zero-dimensional materials composed of magnetic elements such as Fe, Ni, Co, and their respective oxides. Appropriately enough, the commonest of these is Fe_3O_4 nanoparticle (FeNPs). Superior magnetization, biodegradability, availability (available in soils, rocks, bacteria, human body, and even on mars surface), low cost, photothermal effect, theranostic capability and promising biochemical properties makes it a better candidate for MHT (C Blanco-Andujar, Teran, & Ortega, 2018; Espinosa et al., 2016; Goossens, Wielant, Van Gils, Finsy, & Terryn, 2006; Gupta & Gupta, 2005; Shi, Bedford, & Cho, 2011; Shi et al., 2015; Silva, Andrade, Silva, Valladares, & Aguiar, 2013).

1.2 Research Problem Statement

Modifying the surface of bare FeNPs has been shown to play definite roles in its general tolerance in MHT application. It improves physiological response, prolongs circulation time (residence time) by avoiding immediate phagocytic capture and provides functional groups for further derivatization. Unfortunately, such modification significantly reduces its SAR (heating efficiency), implying a decline in MHT performance. Therefore, efforts to improve the MHT performance of FeNPs are necessary.

The heating efficiency of FeNPs could be enhanced by appropriately functionalizing the bare FeNPs with a temperature-responsive polymer or surfactant such as polyethylene glycol (PEG) and graft them onto graphene oxide (GO) nanoplatform to form a magnetic hybrid nanostructure (MHNS). Utilizing the large surface of GO nanoplatform (which will act as a support) ensures clustering and bulk availability of functionalized FeNPs at the required cellular region, improve the contacting surface and thus, enhances SAR. Another challenge that arises here is the functionalization and grafting method.

Several methods have been trailed in developing MHNS of various compositions. They are herein classified as either *in situ* (one-pot) or *ex-situ* (multistage) approaches. However, the major trend is that: (i) the end products lack the ability to generate optimum heat that can potentially kill the cancer cells; and (ii) some of the prerequisites for preparing an MHNS that could withstand stable MHT performance involves the use of stringent experimental parameters and special experiment conditions such as elevated temperature, pressure and continuous flow of argon, nitrogen or other inert gases and even adding toxic chemicals like hydrazine. Given the above, this study will explore the possibility of synthesizing an efficient MHNS in a facile approach.

1.3 Aim and Objectives of the Research

The aim of this research is to synthesis an MHNS (GO-FeNPs-PEG) that is capable of generating heat when subjected to ACMF. The objectives of this study are:

1. To synthesize superparamagnetic bare FeNPs using the coprecipitation method and functionalize it with polyethylene glycol (PEG). Furthermore, graft the functionalized FeNPs onto graphene oxide nanoplatform (GO), which will act as a support to form a magnetic hybrid nanostructure (MHNS).
2. To characterize the synthesized MHNS in terms of its physicochemical and magnetic properties using XRD, FTIR, FESEM-EDX, and VSM analyses.

3. To estimate the performance of the synthesized MHNS in magnetic hyperthermia therapy (MHT) by measuring its SAR under the influence of ACMF and observe how the magnitude could be influenced by concentration, viscosity and magnetic field strength.

1.4 Scope of the Research

The present study is limited to synthesizing MHNS mainly composed of FeNPs, PEG and GO using an *ex-situ* approach and estimating its heating performance under the influence of ACMF.

In line with the above, the MHNS are synthesized by a facile four-step coprecipitation approach: synthesis of bare FeNPs, followed by silanization of the bare FeNPs with (3-Aminopropyl)triethoxysilane (APTES) to promote its interfacial behavior, then functionalization with PEG and finally grafting the PEG functionalized FeNPs onto GO nanoplatform. Furthermore, the approach was fine-tuned by systematically varying FeNPs, APTES, PEG and GO loading. All these reaction steps were maintained in natural atmospheric conditions. The crystal structure, morphology, magnetic property and other physicochemical properties of the products obtained at each reaction step were validated by characterization techniques such as XRD, FTIR, FESEM-EDX and VSM. Lastly, the synthesized MHT materials were subjected to ACMF to evaluate their heating performance (SAR) in relation to composition, concentration, background warming, heating medium viscosity, frequency and magnetic field strength applied. Also, for the first time, the SAR-pH dependence has been established herein. Collectively, the results obtained from these techniques provide prospects and synergistic information towards developing functional MHNS for cancer therapy at a cellular level.

1.5 Dissertation outline

This dissertation is structured into five chapters. The following is an overview of each chapter:

1. ***Chapter 1: Introduction***

This chapter gives a general background of the research. It highlights the challenges obstructing the spread of magnetic hyperthermia therapy as the next-generation cancer therapeutics and a possible way to address them. The aim, objectives, and scope of this research work were also pointed out.

2. ***Chapter 2: Literature Review***

This chapter presents a comprehensive review of magnetic hyperthermia therapy (MHT). Based on the information retrieved from the reviewed literature, an informative explanation is provided sequentially, covering the concept of MHT, synthesis of FeNPs and the approaches for developing a magnetic hybrid nanostructure (MHNS) for MHT. Furthermore, various characterization techniques and necessary parameters often studied in validating the performance of MHNS were also discussed.

3. ***Chapter 3: Materials and Methodology***

This chapter gives the details of materials, chemicals, synthesis method, characterizations and performance evaluation techniques employed in this study.

4. ***Chapter 4: Results and Discussion***

In this chapter, a comprehensive and comparative explanation concerning the preparation of MHNS, its characterization and heating performance in relation to the aim and objectives of this study were discussed.

5. ***Chapter 5: Conclusions and future work***

All conclusions and recommendations for future work are highlighted in this chapter.

CHAPTER 2: LITERATURE REVIEW

2.1 Materials for Magnetic Hyperthermia Therapy (MHT)

MHT is based on the concept that magnetic nanoparticles (MNPs) delivered to cancer sites can generate heat when exposed to ACMF or NIR, thus selectively destroying the cancer cells without harming nearby healthy cells (Albarqi et al., 2019; Yu et al., 2020; Q. Zhang, Liu, et al., 2017). The heat is generated in an ACMF via Brownian and Néel relaxations (both impactful at superparamagnetic size regime however, the former could exceed 250 nm); hysteresis loss (prompted by shifting of magnetic walls, which is often in non-superparamagnetic particles); or eddy current (impactful at centimeter or larger scale) (Ganesan et al., 2019; Mahmoudi, Bouras, Bozec, Ivkov, & Hadjipanayis, 2018; Shi et al., 2015; Sugumaran et al., 2019). On the other hand, the recently discovered photothermal effect of MNPs (specifically FeNPs) enables heat generation in a NIR environment (Rodríguez-Rodríguez et al., 2020). Although ACMF is preferable due to its greater penetration power, NIR may be beneficial for near-surface tumors and patients who are susceptible to magnetic fields, such as those who have pacemakers (Shi et al., 2015).

As mentioned earlier, the heating efficiency in MHT is quantified by SAR (Raouf et al., 2020). SAR is influenced by the magnitude of ACMF strength (amplitude) and frequency. Taking into account the safety and threshold of factors like eddy current side effects, the product of the magnetic field strength and frequency applied should not exceed $5 \times 10^9\ Am^{-1}s^{-1}$ according to Rudolf Hergt and Dutz (2007) criterion. SAR also depend strongly on the type of MNPs used (Mahmoudi et al., 2018; Martinez-Boubeta et al., 2013). MNPs are inorganic metallic nanoparticles with a zero-dimensional structure (Ranjan et al., 2018). There are different types of MNPs applicable for MHT. Herein, they are classified structurally as magnetic alloy nanoparticles (MANPs, for example, $Li_xZn_xCo_{x-0.1}Fe_{x+2}O_4$, Fe–Co–Au and $Ni_{1-x}Zn_xFe_2O_4$) and magnetic metal oxide

nanoparticles (MMONPs). Iron oxide nanoparticles (IONPs) are the commonest of all and belong to the latter classification (Barrera et al., 2020; Beola et al., 2019; Kharisov et al., 2012; H. J. Kim & Choi, 2019; Niederberger, 2007).

There are 16 to 17 distinct structural types of IONPs, which can be classified into three groups: oxide-hydroxides, hydroxides and oxides (Pedersen, 2006). The first two groups are compounds composed of Fe, O, and OH, whereas the third group is only composed of Fe and O elements. The prominent examples of oxides include Fe_3O_4 (magnetite), FeO (wüstite) and Fe_2O_3 (hematite), are (Cornell & Schwertmann, 2003). A vivid description of MNPs structural classification, groups and notable examples are summarized in Figure 2.1. From the majority of literature reviewed, MMONPs, precisely Fe_3O_4 nanoparticles (FeNPs), are commonly used for MHT because of their remarkable physicochemical properties (Beola et al., 2019; Weihong Chen, Wen, Zhen, & Zheng, 2015).

Table 2.1 summarizes the physicochemical properties of different MMONPs widely used in MHT. As compared to other MMONPs, FeNPs appeared favorable due to its: low cost, availability (they can be found in soils, rocks, several species of bacteria, the human body, and even the surface of Mars), biodegradability, superparamagnetic behavior, superior thermal conductivity and high M_S. For instance, its M_S is approximately 200 times stronger than hematite; this could rise from the absence of cation vacancies in its lattice and antiferromagnetic interaction between tetrahedral and octahedral sublattice (Manohar & Krishnamoorthi, 2017; Stojanovic, Dzunuzovic, & Ilic, 2018).

Still on, decreased tumor cell viability has been correlated with the generation of reactive oxygen species (Domenech, Marrero-Berrios, Torres-Lugo, & Rinaldi, 2013). FeNPs has recently been shown to enhance reactive oxygen species (ROS) generation, which can further be increased under the influence of ACMF (Xiaowei Ma et al., 2019). Such FeNPs activity in a tumor microenvironment will amplify the therapeutic effects. In

addition to all of these, FeNPs can be synergistic if used as a vehicle for the delivery of drugs and other materials without losing its MHT capacity (Mohanta, Saha, & Devi, 2018; Soetaert et al., 2017; Q. Zhang, Liu, et al., 2017).

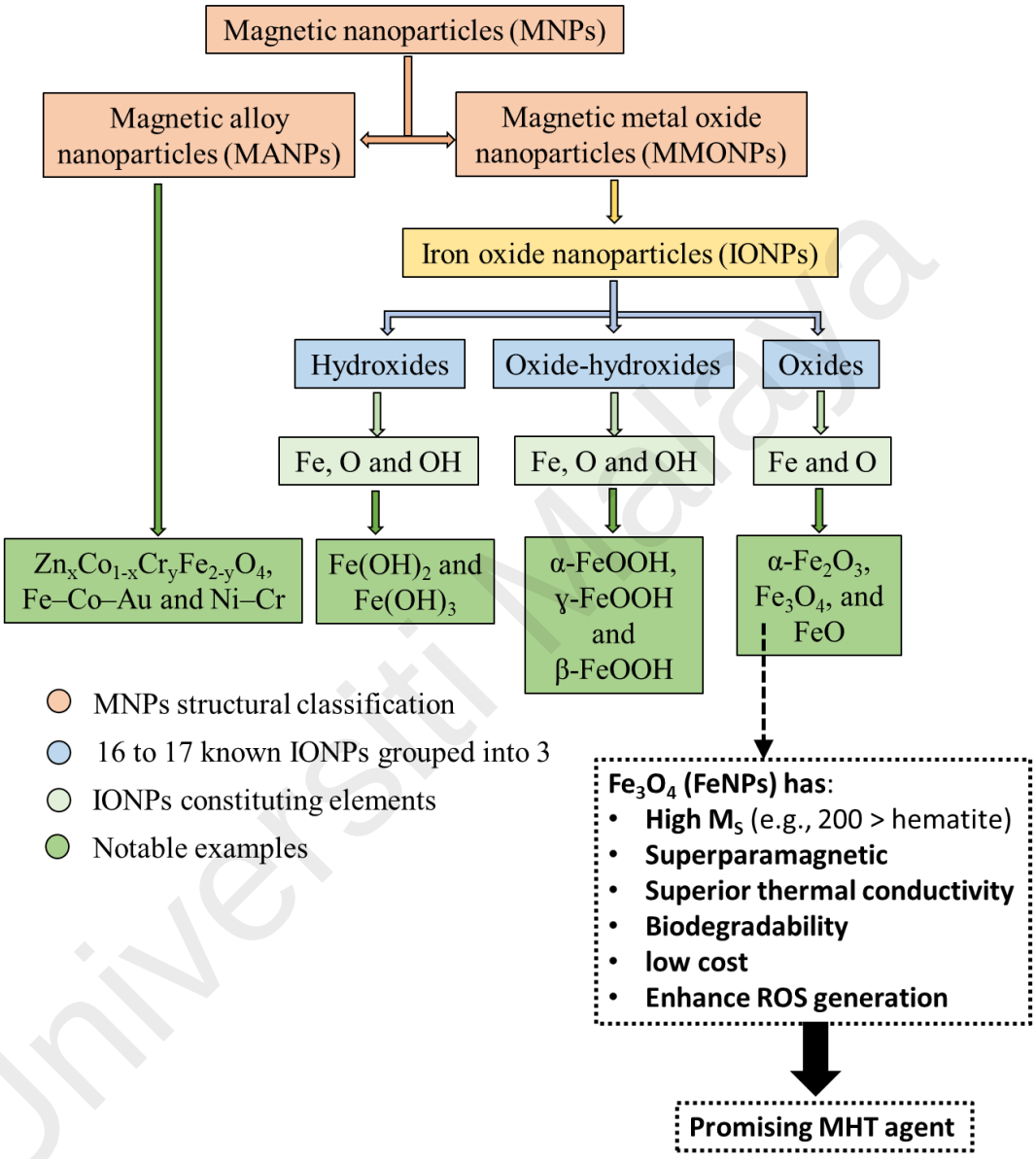

Figure 2.1: A scheme summarizing magnetic nanoparticles (MNPs) structural classification, groups, and some notable examples.

Table 2.1: Physicochemical properties of magnetic metal oxide nanoparticles (MMONPs) commonly used for MHT.

MMONPs	Thermal Conductivity (W/mK)	M_S (emu/g)	Size (nm)	Surface Area (m^2/g)	Reference
Fe_3O_4	0.60 – 0.97	40 – 81	20 – 30	40 – 60	(Han, Luo, et al., 2018; Y. Huang et al., 2018; S. Shen et al., 2018; Upadhyay, Soin, & Roy, 2014)
γ-Fe_2O_3	0.57 – 0.72[+]	52 – 60	19 – 32	68	(da Silva Júnior, de Oliveira Pinheiro, Moreira, de Souza, & de Lima, 2017; Manoukian et al., 2019; Syed, Garg, & Sarkar, 2018; Zahedi, Ansari, Wu, Bencharit, & Moshaverinia, 2017)
$MnFe_2O_4$	0.62 – 0.76	33 – 55	9 – 30	66	(Diana, Humberto, & Jorge, 2019; Karaman, Karaipekli, Sarı, & Biçer, 2011; Qian, Li, Feng, & Nian, 2017; Tang et al., 2017; J.-W. Wang et al., 2018; Q. Zhou et al., 2018)
$NiFe_2O_4$	0.60 – 0.75	25 – 45	12 – 30	26 – 90	(Goodship & Jacobs, 2009; Khan, Hamadneh, & Khan, 2017; Xue, Zhong, Gao, & Wang, 2016; Q. Zhu, Bao, Zhang, Yu, & Lu, 2018)
$COFe_2O_4$	0.60 – 0.85	37 – 62	10 – 22	58	(Marcano et al., 2010; Ramezanzadeh, Ghasemi, Mahdavian, Changizi, & Moghadam, 2015; Ramya et al., 2006; Rask, Knopp, Olesen, Holm, & Rades, 2016)
$MgFe_2O_4$	0.55 – 0.75[++]	8.10 – 16.90	16 – 50	72 – 110	(García-Peña, Díaz, Rodriguez-Gattorno, Betancourt, & Zumeta-Dube, 2018; Y. L. Hong, Ryu, Jeong, & Kim, 2019; Hsan, Dutta, Kumar, Bera, & Das, 2019; Marcano et al., 2010)
CO_3O_4	0.65 – 0.77[+++]	14.30 – 52.37	20 – 35	32.10 – 37.42	(Bandi, Ravuri, Peshwe, & Srivastav, 2019; Weihong Chen et al., 2015; N. Huang, Lim, Chia, Yarmo, & Muhamad, 2011; Low, Lai, Abd Hamid, Chong, & Liu, 2015; Parvez et al., 2014; Sahne, Mohammadi, & Najafpour, 2019; Xu et al., 2016)

[+]10 to 35 ^oC, [++]@ 2 v% $MgFe_2O_4$/ethylene glycol, [+++]@ 15% water mixture, M_S = saturation magnetization, MMONPS = magnetic metal oxide nanoparticles.

However, despite all of the remarkable properties of FeNPs mentioned above, using it in its bare form presents some significant challenges that limit its efficacy in MHT: low circulation time, physiological response and colloidal stability; phagocytosis; and blockage of blood vessels, which usually arises during in vivo stage if agglomerates are large. Accordingly, various surface modifications of bare FeNPs have been shown to curb these challenges. Unfortunately, such modifications significantly reduced its heating efficiency (SAR) which leads to two major issues: (i) inability to generate optimal heat that can potentially destroy the cancer cells selectively, and (ii) frequent administration of large volume of FeNPs (Beola et al., 2019; Bielas, Hornowski, Paulovičová, Rajňák, & Józefczak, 2020; Kumar, Chauhan, Jha, & Kuanr, 2018; Martinez-Boubeta et al., 2013; Rodrigues et al., 2016). Therefore, efforts to improve the heating efficiency of FeNPs for MHT application are necessary.

Summing up observations from the literature reviewed, the limitations above (drop-in SAR being the foremost) could be overcome by two main modifications: (i) functionalizing the bare FeNPs with temperature-responsive polymer coatings (or surfactants) that has the ability to undergo conformational changes during ACMF induction heating; and (ii) then grafting the functionalized FeNPs onto a carbon-based platform that has a large surface area to form a magnetic hybrid nanostructure (MHNS). These will alter the surface chemistry of the bare FeNPs and potentially avert the drawbacks (Beola et al., 2019; Mahmoudi et al., 2018; Mai et al., 2019; Tuček et al., 2016).

It is worthwhile to mention that such MHNS should retain the superparamagnetic behavior of the embedded FeNPs. By implications, MHNS with superparamagnetic behavior possesses a large magnetic moment and behaves like a giant paramagnetic atom with a quick on and off response to applied magnetic fields (Obaidat, Issa, & Haik, 2015).

Losing this unique ability results in the agglomeration of MHNS in the absence of magnetic fields, and the diffusibility of the MHNS to the required cellular region will be hampered. Thus, it creates possible capillaries blockage because smaller-sized NPs are optimum for cellular uptake (Q. Feng et al., 2018).

Carbon-based materials such as graphene oxide (GO), graphene quantum dots (GQDs), carbon dots (CDs), carbon nanotubes (CNTs) and fullerenes have been demonstrated to be applicable in biomedical applications. Among these, graphene carbon-based materials (like GO and GQDs) are exceptional due to their lower levels of impurities (Eivazzadeh-Keihan et al., 2019). For example, CNTs have one major downside; low water solubility (Masotti & Caporali, 2013). However, their hollow structure makes them suitable for drugs and imaging agent carriage (Zuo, Wu, Zhang, & Gao, 2018). According to a feasibility study, grafting FeNPs onto CNTs results in a significant decrease in M_S value (from a bulk value between 85-100 emu/g_{FeNPs} to only 8.2 emu/$g_{FeNPs-CNTs}$). However, with an improvement in M_S value, the inductive heating capacity of MHNS could be enhanced (Krupskaya et al., 2009; Obaidat et al., 2015; Zhao, Zeng, Xia, & Tang, 2009).

GQDs contains graphene nanoparticles with layer dimensions less than 10 nm and displays a graphene quantum effect (Alegret et al., 2017). Quantum dots generally pose toxicity; therefore, it is not viable to use them in healthy cells (Tiwari et al., 2020). However, due to its large optical absorptivity, GQDs could be better for bioimaging. This is the main difference between GQDs and GO (and other fluorescent materials). The poor emissive properties of GO are attributed to its functional groups, resulting in sp^2 hybridized clusters that cause localized non-irradiative electron-hole pairs. Nonetheless, due to quantum confinement and edge effects, GO could be cleaved into smaller

nanoparticles with photoluminescence properties (Muthurasu, Dhandapani, & Ganesh, 2016; Seger & Kamat, 2009; D. Yang et al., 2009).

GO is a polar and single-atomic layer thick nanoparticle with lateral dimension up to tens of micrometers (J. Kim et al., 2010). It is derived from graphite via a wet or dry medium approach. It has various oxygen-containing functional groups (The edge contains carbonyl, hydroxyl and carboxylic while the basal plane contains hydroxyl and epoxy), which makes it amphiphilic; precisely, hydrophilic edges and a more hydrophobic basal plane (Beola et al., 2019; Depan, Girase, Shah, & Misra, 2011; Eda & Chhowalla, 2010).

GO has recently shown efficacy in: rendering some hydrophobic MNPs to hydrophilic; acting as a dispersing agent to process insoluble materials such as graphite, QD and CNT in an aqueous solvent; providing significant electrostatic repulsion against aggregation induced by strong magnetic dipole-dipole interactions between MNPs; compensating the poor dielectric loss of ferrimagnetic iron oxide nanorings; and amplifying the FeNPs ROS generation under the influence of ACMF (J. Kim et al., 2010; Lin et al., 2020; X. Liu et al., 2019; X. Liu et al., 2020; Yongxiu Yang, Huang, Qian, Gao, & Liang, 2020). Coupled with the above and its physicochemical properties presented in Table 2.2, GO is inexpensive to synthesize, biocompatible, nontoxic, has a large surface area, dispersible and soluble in water and other organic solvents (Q. Zhang, Wu, et al., 2017). Considering these remarkable properties, GO qualifies as excellent support for functionalized FeNPs.

On the other hand, noticeable polymers with the capabilities mentioned above are presented in Table 2.3 alongside their physicochemical properties. On inspection, PEG is considered to be outstanding among its counterpart owing to its: physicochemical properties, stealth characteristics, long safety history in humans, higher thermosensitivity, absence of antigenicity and immunogenicity, and ability to undergo conformational changes during applications. In addition, it is worthwhile to mention that PEG serves as

a glue for attaching the FeNPs onto GO, and at the same time, acts as a surface functionalizing agent for improving biostability and bioavailability, which will make the resultant MHNS hardly recognized by macrophages when administered (Dadfar et al., 2019).

In essence, developing an MHNS by grafting PEG functionalized FeNPs onto GO nanoplatform could improve the efficacy of FeNPs during MHT. However, another issue that arises here is the approach for fabricating the MHNS. The approach trailed has a direct effect on the MHNS performance in MHT. Sequentially, in the subsequent sections, explanations are provided regarding the synthesis of FeNPs and the approach for its functionalization and grafting onto GO nanoplatform to yield the proposed MHNS.

Table 2.2: Physicochemical properties of graphene oxide (GO).

Physicochemical properties	Value	Comments	Reference
Density (kg/m^3)	901 – 879	-At 0.01-0.02% mass of GO in DI water. -Concentration is slightly inversely proportional to density because the density of DI water is higher than the dispersed GO.	(Anin Vincely & Natarajan, 2016)
Color	Yellowish-brown, dark brown - mud-brown, blackish-brown	-Color change with the degree of reduction.	(Alam, Sharma, & Kumar, 2017; Alazmi, Rasul, Patole, & Costa, 2016)
Thermal conductivity (w/mk)	2 – 1000	-It declines monotonically with a rise in the degree of oxidation.	(Mahanta & Abramson, 2012; Schwamb, Burg, Schirmer, & Poulikakos, 2009; Yi Yang et al., 2019; H. Zhang, Fonseca, & Cho, 2014)
Surface area (m^2/g)	1650 – 1800	-Decreases with an increase in water content.	(Szabó, Tombácz, Illés, & Dékány, 2006)
Mobility (cm^2/v/s)	850	-Significantly lesser than pristine graphene	(Kobayashi, Kimura, Chi, Hirata, & Hobara, 2010; Xiaosong Wu et al., 2008; Q. Zhang, Wu, et al., 2017)
Thickness (nm)	0.8 – 2.0	-GO is much thicker than graphene due to oxygen-containing functional groups on both the edge and basal plane.	(Wufeng Chen, Yan, & Bangal, 2010; S. Shen et al., 2018)
Breaking strength (n/m)	30	-Smaller than (~14%) graphene.	(Zandiatashbar et al., 2014)
Young's modulus (tpa)	0.1 – 0.4	-Less than GO (~1), hence can be easily modified at mild conditions.	(Zandiatashbar et al., 2014)
Functional group	Hydroxyl, epoxy, carbonyl, and carboxylic	-Hydroxyl and epoxy (at the basal plane). Carbonyl, hydroxyl and carboxylic (at the edge)	(Hossain et al., 2012; Thalib, Mustapha, Feng, & Mustapha, 2020)

Table 2.3: Physicochemical properties of commonly used polymers.

Polymer/ surfactants	Thermal conductivity (W/mK)	Solubility	Melting point (°C)	Density (g/cm^3)	Viscosity (kg/m.s)	Advantages	Reference
PEG	0.24 – 0.32	Many organic solvent, nonpolar environment, and water	43 – 65	0.99 –1.03	0.002 – 0.007	-Nontoxic, improves biostability, blood circulation time and internalization efficiency of NPs	(da Silva Júnior et al., 2017; Gupta & Curtis, 2004; Karaman et al., 2011; S. Liu, Guo, & Xie, 2012; Manoukian et al., 2019; Qian et al., 2017; Suk, Xu, Kim, Hanes, & Ensign, 2016; Syed et al., 2018; Tang et al., 2017; Zahedi et al., 2017)
Dextran	–	Water	274	0.90 – 1.35	0.1 – 1.0	-Stabilizes NPs in colloidal solution and increases blood circulation time	(Berry, Wells, Charles, & Curtis, 2003; Diana et al., 2019; J.-W. Wang et al., 2018; Q. Zhou et al., 2018; Q. Zhu et al., 2018)
PVA	0.31	Water	200 – 230	1.19 – 1.31	0.323	-Reduce coagulation and improve monodispersity of NPs	(Altaf et al., 2021; Goodship & Jacobs, 2009; Shan, Xing, Luo, Liu, & Chen, 2003; Xue et al., 2016)
PVP	0.11 – 0.12	Water and organic solution	155 – 170	1.20 – 1.18	0.002	-Stabilizes NPs in colloidal solution and increases blood circulation time	(D'Souza, Schowen, & Topp, 2004; Khan et al., 2017; Ramya et al., 2006; Rask et al., 2016)

2.2 Synthesis of Iron Oxide (Magnetite) Nanoparticles

There are three different routes to synthesis FeNPs: (i) biological route, (ii) chemical route, and (iii) physical route (Hasany, Ahmed, Rajan, & Rehman, 2012; Revia & Zhang, 2016). The following subheadings give a comparative explanation regarding these routes.

2.2.1 Biological route

The biological route is greener and eco-friendlier in comparison to physical and chemical routes. It does not involve the use of hazardous and expensive chemicals and materials (Fatemi, Mollania, Momeni-Moghaddam, & Sadeghifar, 2018). In general, two materials are frequently used in this route: microbial-derived products such as fungi, bacteria, enzymes, and even the microorganisms themselves; and different parts of plants such as seed, fruit, plant extracts and tissues (Aksu Demirezen, Yıldız, Yılmaz, & Demirezen Yılmaz, 2019; Iravani, 2019; Radini, Hasan, Malik, & Khan, 2018; Shafaei, Babaei, Shahvelayati, & Honarmand Janatabadi, 2019).

Reduction/oxidation are the major reactions involved in this route, and the resulting NPs are highly biocompatible (Fatemi et al., 2018). Despite the fact that the route is facile, inexpensive, and eco-friendly, the NPs obtained have low stability and significant tendency to aggregate. Additionally, the route is inflexible in terms of obtaining NPs of desired shape and size. However, these setbacks could be minimized by optimizing parameters such as reaction time, concentration, and type of material, which are critical for microorganism growth and cellular activities. Nonetheless, the precise reaction mechanism of this route is yet to be profoundly described because it is at the development stage (Iravani, 2019). Hence, this environmentally friendly route needs more exploration.

2.2.2 Physical route

The physical route includes methods such as pulsed laser ablation, pyrolysis and powder ball milling. In the pulsed laser ablation method, the reaction is triggered by a

pulsed laser beam wherein a target material is submerged in a liquid solution. The pulsed laser beam will irradiate the target material and cause it to ablate under atmospheric conditions, resulting in a desired composition change in the solution (Amendola & Meneghetti, 2013; M.-L. Chen, Gao, Chen, Pang, & Zhang, 2018). By changing the liquid solution or target material, different phases of MMONPs can be obtained (Crivellaro, Guadagnini, Arboleda, Schinca, & Amendola, 2019). The limitations of this method include the difficulty of controlling particle size, which is a major setback for MHT application; however, the lack of toxic chemical precursors makes the end product less harmful to healthy cells as compared to the chemical route (Amendola & Meneghetti, 2013; Rodio et al., 2017).

On the other hand, the pyrolysis method is another physical route harnessed to obtain homogeneous NPs. The method involves an interaction between a laser and a gaseous flow of iron precursors. Bomatí-Miguel, Zhao, Martelli, Di Nunzio, and Veintemillas-Verdaguer (2010) produced ultrafine iron NPs via this method. They achieved the synthesis by subjecting a flowing mixture of gases to heat using a continuous wave of CO_2 laser, which initiates and sustained the reaction. The two critical parameters for producing large NPs with a size above 20 nm are carrier gas flux and pressure. As for NPs within superparamagnetic size regime (< 26 nm), the temperature at which the precursors was evaporated is pivotal (Bomatí-Miguel et al., 2010). Generally, FeNPs obtained via this method are pure, homogeneous and in good shape. However, the method is limited by high energy and volume requirements (Muhammad et al., 2019).

2.2.3 Chemical route

In comparison to biological and physical routes, the chemical route is often explored because the various synthesis methods involved are relatively straightforward, inexpensive, yield-maximizing, and easily scalable (LaGrow et al., 2019). There are many

synthesis methods under the chemical route: electrochemical, hydrothermal, solvothermal, coprecipitation, sonochemical, thermal decomposition, and poly methods (Bunge et al., 2019; Dutta et al., 2018; Jana, Chen, & Peng, 2004; Köçkar, Karaagac, & Özel, 2019; Setyawan & Widiyastuti, 2019; Z. Shen, Wu, & Chen, 2016; Xiaoge Wu, Xu, & Zhu, 2019). Among all, the coprecipitation method is the most frequently used. Nevertheless, in the following subheadings, all these methods will be discussed.

2.2.3.1 coprecipitation method

As mentioned above, the coprecipitation method is the most frequently used among all chemical methods for synthesizing FeNPs (Ali et al., 2016; LaGrow et al., 2019). The method is facile, less toxic, inexpensive and yields a high amount of FeNPs. However, before using the obtained FeNPs for MHT, some limitations such as poor FeNPs size distribution, morphology and surface chemistry need to be curbed (Z. Shen et al., 2016). Typically, the coprecipitation method involves mixing iron precursors and a base (sodium and ammonia solution are commonly used) at a mild or elevated temperature. The base can be added all at once (quickly), resulting in a rapid rise in solution pH or gradually over time, resulting in a slow rise in solution pH. The former is favorable for large-scale or continuous processing, as it significantly reduces processing time (LaGrow et al., 2019).

The rate at which the base is added to the iron precursors may influence the coprecipitation reaction. For example, a study showed that by adding a base continuously at a slow rate, akaganeite nucleates then transform to FeNPs through goethite (Ahn, Kim, Yang, Lee, & Kim, 2012); however, by adding the base all at once at a high rate, an additional pathway is formed (ferrous hydroxide nucleated and through lepidocrocite, transformed to FeNPs). The study concludes that the divergent reaction pathways occurred due to pH inhomogeneity before homogeneous mixing is achieved.

Additionally, when the base is added abruptly (all at once), both pathways coexist but are dominated by the goethite – FeNPs transformation in most cases.

A recent work studied the mechanism of FeNPs synthesis, and the outcome is in line with the above conclusion (LaGrow et al., 2019). The study used sodium carbonate in place of a strong base; this reduces the growth kinetics. Thus, the kinetic can be studied easily (Cristina Blanco-Andujar, Ortega, Pankhurst, & Thanh, 2012). When the base and precursor were mixed, two initial phases were observed: ferrihydrite and iron hydroxide carbonate plates. Both are crystalline and primarily formed by Fe^{3+} and Fe^{2+}, respectively. The former was the seed that finally formed FeNPs, while the latter was the source of iron ions that cause the growth and phase change. Hence, the study concludes that no growth and formation of FeNPs without Fe^{2+} in the solution. Additionally, the amount of ferrihydrite in the end product depends on the number of ions in the reaction.

A major observation from the literature is that, in coprecipitation method, essential properties like FeNPs shape or saturation magnetization (M_S) can be controlled by parameters such as reaction time, temperature, order of reacting species and pH (Mürbe, Rechtenbach, & Töpfer, 2008; Unsoy et al., 2015; Vayssieres, Chanéac, Tronc, & Jolivet, 1998). Generally, the coprecipitation reaction is more likely to be favored in basic pH range (9 – 13), ions ratio of 2:1 ($Fe^{+3/+2}$), and maintaining an oxygen-free environment (Alazmi et al., 2016; Nihal Saad Elbialy, Fathy, & Khalil, 2014; Nihal Saad Elbialy, Fathy, & Khalil, 2015; Nihal S Elbialy et al., 2019; Koushkbaghi, Jafari, Rabiei, Irani, & Aliabadi, 2016; Rodrigues et al., 2018; Rodrigues et al., 2016; J. Sun et al., 2007).

Figure 2.2 depicts different reaction conditions for synthesizing FeNPs via the coprecipitation method. The general reaction is represented by equation (1).

$$Fe^{2+} + 2Fe^{3+} + 8OH^- \rightarrow Fe_3O_4 + 4H_2O \quad (1)$$

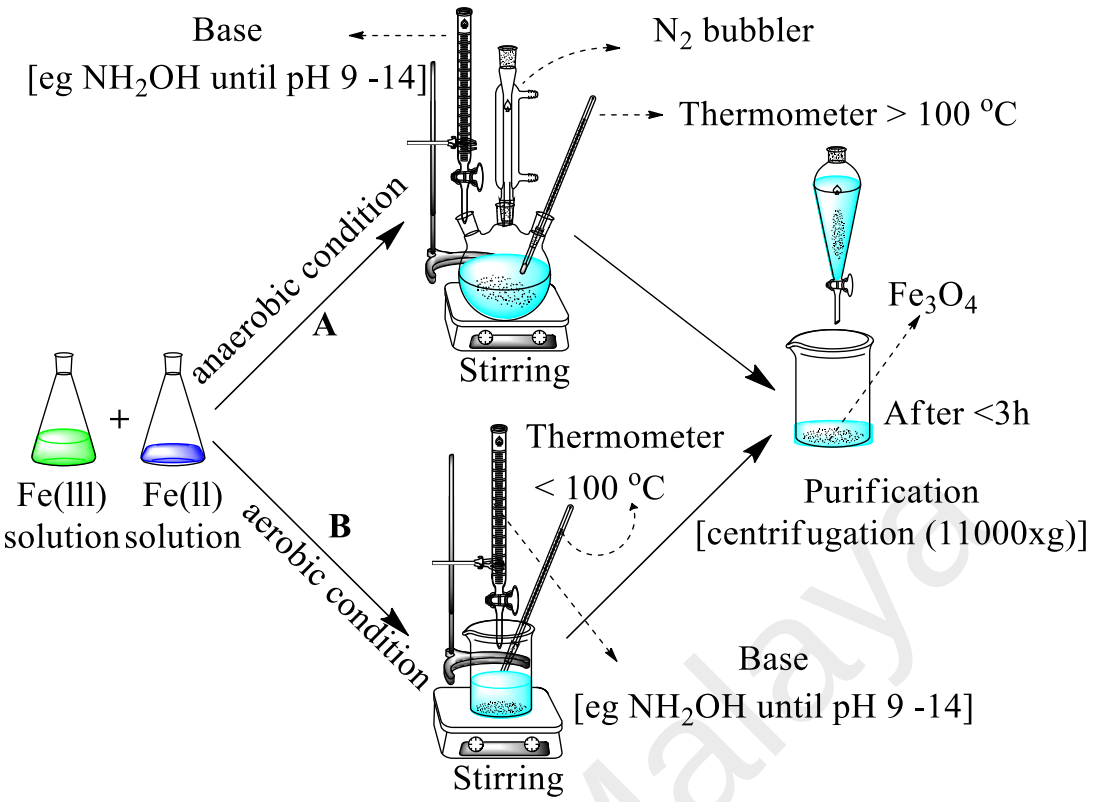

Figure 2.2: A schematic illustrating the reaction conditions for synthesizing FeNPs via coprecipitation method.

As stated above (in the materials for MHT section), other phases of FeNPs also exist. They could simply be synthesized by adjusting the reaction conditions of the described coprecipitation method. The reaction is susceptible to oxygen; a phase change is likely to occur if exposed to oxygen (Noqta, Aziz, Usman, & Bououdina, 2019). For example, studies showed that equation (1) could further oxidize to bernalite ($Fe(OH)_3$) or maghemite when exposed to oxygen via equation (2) and (3), respectively; in addition, critical oxidation of Fe^{2+} to Fe^{3+} is likely via equation (4) (D. K. Kim, Zhang, Voit, Rao, & Muhammed, 2001; Yamaura et al., 2004). The likelihood strongly depends on the reaction temperature and kinetics. If it occurs, forming maghemite or bernalite becomes favorable via equations (5) and (6), respectively (forming maghemite is more difficult compared to hematite under thermal dehydration conditions).

$$4Fe_3O_4 + O_2 + 18H_2O \rightarrow 12Fe(OH)_3 \quad (2)$$

$$4Fe_3O_4 + O_2 \rightarrow 6Fe_2O_3 \quad (3)$$

$$Fe^{2+} + 0.5H_2O + 0.25O_2 \rightarrow Fe^{3+} + OH^- \quad (4)$$

$$2Fe^{3+} + 6OH^- \rightarrow \gamma\text{-}Fe_2O_3 + 3H_2O \quad (5)$$

$$Fe^{3+} + 3OH^- \rightarrow Fe(OH)_3 \quad (6)$$

In another effort, the effect of external conditions such as pressure was examined by J. Yang et al. (2014). They prepared FeNPs (magnetite) in two different coprecipitation setups, one in an open beaker and the other in a closed beaker. They observed faster particle growth in the latter setup; this yielded larger FeNPs compared with the former setup. To elucidate the rationale behind this divergence, they proposed equations 7 – 11:

$$NH_3 \cdot H_2O \rightarrow NH_4^+ + OH^- \quad (7)$$

$$Fe^{3+} + 3OH^- \rightarrow Fe(OH)_3 \quad (8)$$

$$Fe(OH)_3 \rightarrow FeOOH + H_2O \quad (9)$$

$$Fe^{2+} + 2OH^- \rightarrow Fe(OH)_2 \quad (10)$$

$$Fe(OH)_2 + 2FeOOH \rightarrow Fe_3O_4 + 2H_2O \quad (11)$$

OH^- and NH_3 obtained from $NH_3 \cdot H_2O$ evaporate continuously in the open beaker set up during the growth process. In contrast, they are trapped in the closed beaker and consequently raise the pressure inside the beaker; additionally, the high amount of OH^- in the closed beaker will increase FeNPs precipitation.

2.2.3.2 thermal decomposition method

The thermal decomposition method has been reported for synthesizing FeNPs, although it is less common than coprecipitation or hydrothermal methods (Koushkbaghi et al., 2016). It is a non-aqueous method and mainly involves the use of heat, organometallic compounds and stabilizing surfactants (Weihong Chen et al., 2015; Dutta et al., 2018; Jana et al., 2004). Generally, precursors like ferric acetylacetonate or iron pentacarbonyl are decomposed at extreme temperatures in a high boiling point organic solvent (or just heat in a solvent-free process). The feeding rate, type of precursor and solvent used would determine the morphology and particle size distribution of the end product; typically, the use of organic solvent increases the possibility of keeping apart the nucleation from the growth, which helped in avoiding high reactivity of iron ion(s) (Arias et al., 2018; Z. Shen et al., 2016). The advantage of this method is that the FeNPs obtained have good particle size distribution and high M_S value. However, the FeNPs retain some solvent, making it toxic and more hydrophobic; thus, they are less biocompatible and not the best for MHT (Z. Shen et al., 2016).

2.2.3.3 poly method

The polyol method is another approach for preparing FeNPs with controlled size and shape (Koushkbaghi et al., 2016). The method is similar to the thermal decomposition method. The main difference between them is that more hydrophilic FeNPs are obtained in the polyol approach. Also, the polyol solvents may serve as reducing or stabilizing agents. Although the FeNPs are water-soluble, removing organic solvents or surfactants used during the polyol process is difficult (Z. Shen et al., 2016).

2.2.3.4 hydrothermal method

The hydrothermal method is an aqueous process that involves the use of reactors or sealed containers that can withstand high pressure (>2000 psi) and temperature (100 –

250 ºC). These reaction conditions are relatively harsh compared with methods like coprecipitation (Halilu et al., 2016; Rodrigues et al., 2016). In a recent study, FeNPs was successfully synthesized by hydrothermal method; a solution of ferrous and ferric ions was mixed with a base (ammonium hydroxide) and kept in a sealed autoclave for 12 h at 160 ºC. After the reaction, it was cooled naturally and dried overnight at 60 ºC to obtain powdered form FeNPs (Köçkar et al., 2019). An earlier study conducted by Hasany et al. (2012) investigate the influence of residence time and concentration of precursors on morphology and particle size distribution. They found that increasing the concentration of precursors will increase particle size distribution, and for a shorter residence time, more monodispersed particles will be produced. Apart from being water-soluble, the FeNPs obtained from this method is more crystalline because of the harsh process condition. Nevertheless, this method is more expensive and difficult to scale up due to the high pressure and temperature involved (Z. Shen et al., 2016).

2.2.3.5 solvothermal method

This method is similar to the hydrothermal method; the main difference is that, in the hydrothermal method, water is used as a solvent, while in the case of the solvothermal method, organic solvents are used. A reported experiment used ethylene glycol and diethylene glycol as solvents (Bunge et al., 2019). In the experiment, a mixture of the organic solvent, ferric chloride and sodium salts were kept in an autoclave reactor for 10 hours at 200 ºC. After purification and drying, FeNPs were obtained. This method generates better monodisperse particles with controlled shape and crystallinity than the hydrothermal method. However, the particles are more hydrophobic and toxic, thus less biocompatible (Z. Shen et al., 2016).

2.2.3.6 sonochemical method

The sonochemical method (also called ultrasound irradiation) is considered a green and easy approach for synthesizing FeNPs (Noqta et al., 2019). It is attributed to high-intensity ultrasonication. The frequency and intensity of the sonication may be used to control the quality of particles synthesized (Arias et al., 2018). These sonochemical parameters were studied using a 40 kHz ultrasonic bath and 20 kHz ultrasonic probe sonicators (Xiaoge Wu et al., 2019). Briefly, in the experiment, for each of the equipment, a mixture of organic solvent, ferric chloride and sodium salt was sonicated for 1 h at 40 – 45 ^{o}C. FeNPs from the 20 kHz probe was observed to be more uniform in size with fine distribution. Although this method appears facile and time-saving, the growth mechanism is not yet explicated (Koushkbaghi et al., 2016).

2.2.3.7 electrochemical method

The electrochemical formation of FeNPs was previously understudied, but this has changed in recent years, owing to the necessity to develop environmentally friendly methods (Hasany et al., 2012; Lozano, Casillas, de León, Walsh, & Herrasti, 2017). The flow of electric current via a setup of two or more electrodes submerged in an electrolyte solution is the essential aspect of this method. Redox reaction occurs at the solution-electrode interface; in the end, FeNPs precipitates from the electrolyte solution (Setyawan & Widiyastuti, 2019). The reaction can take place at low temperatures and can be modulated by adjusting the potential difference at the solution-electrode interface (Setyawan & Widiyastuti, 2019).

Lozano et al. (2017) investigated the mechanism involved in this approach. They discovered that the two main electrochemical reactions at the anode and cathode are ion dissolution and water reduction (equations 12 and 13). The former provided Fe^{2+}, which in the basic media precipitates into $Fe(OH)_2$ and further oxidized by dissolved oxygen in

the solution to generate γ-FeOOH as shown in equation 15 (the oxidation occurred due to oxygen diffusion from the environment). Finally, it went through a catalyzed topotactic process to form the FeNPs. The reactions (12) to (16) summarized their proposed mechanism. In particular, equation 16 represents the maghemite-magnetite phase transformation.

$$Fe \rightarrow Fe^{2+} + 2e^{-} \quad (12)$$

$$2H_2O + 2e^{-} \leftrightarrow H_2 + 2OH^{-} \quad (13)$$

$$Fe^{2+} + OH^{-} \rightarrow Fe(OH)_2 \quad (14)$$

$$3Fe(OH)_2 + O_2 \rightarrow 2\gamma FeOOH + Fe(OH)_2 + 2H_2O \quad (15)$$

$$2\gamma FeOOH + Fe(OH)_2 \rightarrow Fe_3O_4 + 2H_2O \quad (16)$$

In a nutshell, the electrochemical method is green and could be easier to controlled (Rahimdad, Khalaj, Azarian, & Nematollahi, 2019). However, its main downsides include low production rate, complicated to design (setup), and particle size are usually greater than 26 nm which makes them less superparamagnetic thus not the best for MHT (Farazi, Vaezi, Molaei, Saeidifar, & Behnam-Ghader, 2018; Rahimdad et al., 2019).

2.3 Preparing a Magnetic Hybrid Nanostructure (MHNS)

As summarized in Table 2.4, MHNS of various compositions has been reported for many applications via different methods. The composition of such MHNS can be grouped into three architectures: (a) bare MNPs functionalized with polymers/surfactants; (b) bare MNPs supported on GO to form GO-MNPs; and (c) GO-MNPs (i.e., architecture b) wrapped with polymers/surfactants. For example, Han, Wang, et al. (2018) reported architecture “a” by modifying the surface of FeNPs (MNPs) with four-arm polyethylene glycol dendrimer for cellulase immobilization. Albert, Abdullah, and Shiroshaki (2018)

engineered architecture “b” by decorating IONPs (MNPs) onto GO for potential drug delivery application. X. Liu et al. (2020) and Sugumaran et al. (2019) fabricated architecture “c” by supporting a bare ferromagnetic NPs (MNPs) on GO and then wrapped them in polymeric surfactants; they obtained the best MHT performance above the safety limits for *Hf* and superparamagnetic size. However, as aforementioned, efficient MHT performance includes heating below *Hf* safety limit and preserving the superparamagnetic attributes.

The various methods for preparing MHNS are classified into two main approaches: *in situ* (one-pot) and *ex-situ* (multistage). The classification is based on the architecture of the MHNS and the process stages involved in its synthesis (Table 2.4). The following subheadings will provide a comprehensive overview of these approaches.

2.3.1 *Ex-situ* approach

The *ex-situ* approach is a multistage process wherein at least the MNPs and/or the carbon support are initially synthesized separately before functionalization and grafting. For the initial stage, various methods are available; they have been discoursed in the previous headings. At the later stage, carbon supports such as GO is used without functionalization since it has no apparent cytotoxicity. However, it can also be functionalized if desired.

Generally, active double bonds and oxygen-containing groups are introduced to the surface of the as-synthesized MNPs to functionalize them. As for the GO, the available oxygen-containing functional groups on both the basal plane (hydroxyl and epoxy groups) and the edge (carbonyl, hydroxyl and carboxyl groups) are utilized for the grafting; it is viable to activate them first before the grafting (Table 2.4).

Weihong Chen et al. (2015) developed an MHNS composed of bare FeNPs, PEGylated GO and doxorubicin for imaging and drug delivery (architecture b) via this approach. The GO was first modified with PEG before grafting the FeNPs on top through an amide bond formed by a condensation reaction. Briefly, the GO nanoplatform modification was achieved by first adjusting the pH of its aqueous solution to 8 using triethylamine before adding 1-ethyl-3-(3- dimethylaminopropyl)carbodiimide (abbreviated as EDC), N-hydroxysuccinimide (abbreviated as NHS) and then the PEG. Finally, the reacting solution was then stirred for 48 h at RT and washed several times before anchoring the FeNPs via the formation of amide bond by EDC condensation reaction.

In a similar study conducted by He et al. (2010), an amino group was introduced to FeNPs to facilitate grafting with the carboxylic functional groups on the GO using EDC and NHS. The end product was found applicable as an absorbent for removing cationic dyes in water. The major distinction between these studies is that the former used PEG-modified GO, whereas the latter used pure GO. In conclusion, the *ex-situ* approach is more time-consuming due to the multistage processes involved. However, as an advantage, the approach allows the morphology and properties of the MHNS (such as size, shape and FeNPs loading) to be rationally tailored to suit a particular application (Layek & Nandi, 2013; Yin, Shah, Chhowalla, & Lee, 2015).

Table 2.4: Summary of different methods for preparing MHNS.

Materials			MHNS Properties	Synthesis			Application	Reference
Metal	**Support**	**Polymer**	**Size (nm)/shape**	**Approach**	**Method**	**Procedure**		
Fe_3O_4	GO	polysaccharides	-	*In situ*	layer-by-layer (LBL)	Polysaccharides (incubated on each other one at a time, 30 min) + GO- Fe_3O_4 (0.01 mg/mL of GO, 60 min) + washing	Hyperthermia and chemotherapy	(Deng et al., 2016)
Fe_3O_4	GO	PEG (6arm)	~ 50-300	*In situ*	Ultrasonication	PEG 25 mg + (GO- Fe_3O_4) + ultrasonication (10 min) + EDC + stirring (overnight, RT) + centrifugation (14800 rpm, 10 min) + washing with DI water	Cancer theranostics	(Xinxing Ma et al., 2012)
Fe_3O_4	GO	PEG (4arm)	-	*In situ*	Ultrasonication and stirring	GO- Fe_3O_4 (10 mL, 1 mg/mL) + 4arm PEG NH_2 (2 mL, 5 mg/mL, 10K or 5K) + sonication (25 ^oC, 3 h) + EDC 2 mg + ultrasound (5 min) + EDC 2.6 mg + stirring (12 h) + washing with DI water + vacuum drying (40 ^oC)	Cellulase immobilization	(Han, Luo, et al., 2018)
Fe_3O_4	GO	PEG	-	*In situ*	Coprecipitation	$FeCl_3 \cdot 6H_2O$ (800 mg) + $FeCl_2 \cdot 4H_2O$ (300 mg) + GO-PEG 40 mL (1 mg/mL) + heating (85 ^oC) + NH_4OH (to pH 10) + rapid stirred (45 min) + centrifugation (4000 rpm, 15 min) + HNO_3 + heating (~ 100 ^oC, 1h)	Drug delivery and MIR	(M.-L. Chen et al., 2018; Ghavami, Mohammadi, Koohi, & Kassaee, 2014)

Table 2.4, continued

Materials			MHNS Properties	Synthesis			Application	Reference
Metal	**Support**	**Polymer**	**Size (nm)/shape**	**Approach**	**Method**	**Procedure**		
Fe_3O_4	-	PEG (1500Da)	> 200	*Ex-situ*	Graf-to	Fe_3O_4 + APTES in C_7H_8 (24 h, 80 °C) + COOH-PEG1500 + C_7H_8 (24 h, 80 °C) + washing with C_2H_6O + freeze-dry (24 h)	Drug delivery and hyperthermia therapy	(Dabbagh et al., 2019; Gil, Castro, & Mano, 2013)
Fe_3O_4	GO	-	-	*Ex-situ*	Covalent bonding	GO mg + H_2O 60 mL + ultrasonication (3 h) + EDC 10 mg + NHS 8 mg stirring (30 min) + ultrasonication (30 min) + Fe_3O_4 20 mg + ultrasonication (30 min) + stirring (80 °C, 1 h) + magnetic separating and washing	Absorbent for removing cationic dyes in water	(He et al., 2010)
Fe_3O_4	-	PEG	346	*Ex-situ*	Coprecipitation	DOX-HCl 20 mg + OA-Fe_3O_4 + C_6H_{14} (~1 mL) + H_2O 30 mL + ultrasonication + CS-PEG (10 mL, 4 mg/mL) + CH_3COOH (pH 5) + NaOH (1 M) + (24 h) + magnetic separation + washing with water + freeze drying (under vacuum)	Drug delivery and MRI	(Xie, Du, Li, & Liu, 2019)
Fe_3O_4	GO	pluronic F-127	160 - 205	*Ex-situ*	Stirring	GO-Fe_3O_4 5mg/mL + HNO_3 1 mol/L (3 h) + washing + drying overnight (60 °C) + pluronic F-127 40 mg/mL + stirring (5 h, RT) + centrifugation (13 000 rpm, 20 min)	Hyperthermia and chemotherapy	(Rodrigues et al., 2018)

Table 2.4, continued

Materials			MHNS Properties	Synthesis			Application	Reference
Metal	**Support**	**Polymer**	**Size (nm)/shape**	**Approach**	**Method**	**Procedure**		
Fe_3O_4-Au	-	PEG(Thiolated-PEG) /	24/spherical	*Ex-situ*	Stirring	Thiolated-PEG (0.02 mg/mg Fe_3O_4-Au) + Fe_3O_4-Au + stirring (24 h) + DOX (1 mg/mg Fe_3O_4-Au) + stirring (4 h) + magnetic separation	Drug delivery, PTT, MRI	(Nihal S Elbialy et al., 2019)
Fe_3O_4	-	PEG	11/cubic	*In situ*	Single step thermal decomposition	iron (III) acetylacetonate 1 g + $Na_3C_6H_5O_7$ 2 g + PEGdiacid (5 mL in 30 mL of PEG) + stirring (30 min, 70 ^oC) + heat (230 ^oC + 5 h)	Drug delivery and hyperthermia	(Dutta et al., 2018)
Fe_3O_4	GO	PEG	4-250/spherical and cubic	*Ex-situ*	Solvent evaporation	Fe_3O_4 + tetrahydrofuran (5 mg/ml) + GO (5 mg/ml) sonication (5 min) + homogenization (8 min) + heating (30min, 80 ^oC to remove excess THF) + washing (DI water) + PEG + bath sonication (10 min) + EDC (10 mg/ml) + NHS (8 mg/ml) + stirring (>1000 rpm) + dialysis	MHT	(Sugumaran et al., 2019)

Table 2.4, continued

Materials			MHNS Properties	Synthesis			Application	Reference
Metal	**Support**	**Polymer**	**Size (nm)/shape**	**Approach**	**Method**	**Procedure**		
Fe_3O_4	-	PEG	~15/spherical	*Ex-situ*	Stirring	PEG-400 (50 mL) + Fe_3O_4 (500 mg) + stirring (4 h) + centrifugation (3000 rpm, 10 min) + separation + centrifugation (14000 rpm, 15 min) + overnight drying (45 ^oC)	Drug delivery	(Mohanta et al., 2018)
Fe_3O_4	-	PEG (2000)	26 – 93/spherical	*Ex-situ*	Solvent evaporation	PEG2000 (1 g melted at 90 ^oC) + DOX 0.3 g + stirring (1 h, 60 ^oC) + Fe_3O_4 (3 g) + $CHCl_3$ + stirring + heating (90 ^oC) + evaporation of $CHCl_3$ (6 h) + hot water + magnetic separation + washing with distilled hot water (RT)	Thermo-chemotherapy	(Q. Zhang, Liu, et al., 2017)
-	GO	PEG, PLA	60	*Ex-situ*	Stirring	PEG-NHS (20 mL, 20 mM) + FA + stirring (1 h, 4^{o}C). 20 mL of the was incubated with incubated with Cur-CMC/PVP GO (1 h, 4 ^{o}C)	Anticancer nano-drug delivery	(Sahne et al., 2019)
Fe_3O_4	-	PEG, PLA	179 – 203/spherical	*Ex-situ*	Sonication	DOX-HCl (1g in 0.5 mL of water) + C_3H_6O -DMC 4 mL (50:50) + PLA-PEG-PLA 20 mg + Fe_3O_4 (20 mg) + EPPT-FITC + sonication (30 s, 0 ^{o}C) + PVA 30 mL + stirring (5 min) + evaporation + centrifugation (30 min, 16602 x g) + washing and filtration	Drug delivery and MRI	(Amani, Begdelo, Yaghoubi, & Motallebinia, 2019)

Table 2.4, continued

Materials			MHNS Properties	Synthesis			Application	Reference
Metal	**Support**	**Polymer**	**Size (nm)/shape**	**Approach**	**Method**	**Procedure**		
Fe_3O_4	-	PEG, PVA	105 – 140/dendritic	*Ex-situ*	Double emulsion	Fe_3O_4 (dispersed in 3 mL distilled water) + PEG (150 mg) CUR (1.5 mg) + CH_2Cl_2- C_3H_6O (10 mL, 1:3) + ultrasonication (until oil phase formed) + PVA 80 mL + ultrasonication (30 s) + magnetic separation + washing + freeze draying (3 days)	Drug delivery (cervical cancer)	(You, Liu, Fang, Xu, & Zhang, 2019)
Fe_3O_4	GO	-	100 – 190/spherical	*In situ*	Electrosp inning process	PAN (10 wt%) + DMF + stirring (6 h, 30 °C) + Fe_3O_4 -GO (5 wt% to PAN) + stirring (24 h, 30 °C) + voltage (20 kV) to fabricate the nanofibers on the PET over collector	Separation of lead and chromium ions in membrane systems	(Koushkbaghi et al., 2016)
Fe_3O_4	-	PAA	250 – 650/spherical	*In situ*	Modified solvother mal	$FeCl_3.6H_2O$ 6 g + EG 150 mL + ultrasonication + CH_4N_2O (9 g) +PAA 6.5g + sonication (30 min) + heating (7 h, 220 °C) + cooled (RT) + washed (DI water) + vacuum drying (7 h, 70 °C)	Hyperthermia and MRI	(Ganesan et al., 2019; Li, Gu, & Zhang, 2012)
Fe_3O_4	GO	-	-	*Ex-situ*	Simple emulsion	GO 40 mg + $CHCl_3$ 14 ml + $C_{18}H_{35}NH_2$ 5 mL + sonication (1 h) + Fe_3O_4 80 mg + $CHCl_3$ 5 mL + sonication (30 min) + overnight draying + washing with C_3H_6O + open air drying (2 h)	Drug delivery	(Albert et al., 2018)

Table 2.4, continued

Materials			MHNS Properties	Synthesis			Application	Reference
Metal	**Support**	**Polymer**	**Size (nm)/shape**	**Approach**	**Method**	**Procedure**		
Fe_3O_4	-	Fucan polysaccharide	10/ quasi-spherical	*Ex-situ*	Adsorption	Fe_3O_4 100 mg + fucan 50 mg/mL + stirring (16 h, 25 ^oC) + washing with distilled water + draying at RT	Biomedical	(Silva et al., 2013)
Fe_3O_4	GO	PVDF (polyvinylidene fluoride)	-	*In situ*	Magnetic field-induced casting	Casting solution containing 9 wt% PVDF, 1 wt% MGO, 2 wt% LiCl, 4 wt% PEG 2000 and 84 wt% DMAc were coated as function layer (50 μm) with a magnetic field (400–500 Gs, 120 s exposure)	Membrane separation	(Y. Huang et al., 2018)
-	GO	PEG and polyacrylamide	-	*Ex-situ*	Covalent bonding	Methacrylic GO + PEG-dimethacrylate (or acrylamide and N,N'-methylenebisacrylamide) + sonication (1 min) + $(NH_4)_2S_2O_8$ (0.1% w/v) + tetramethylethylenediamine (0.01% v/v) + 1 h reaction time .	Biomedical	(Jang, Hong, & Cha, 2017)
Fe_3O_4	-	PEG	30 – 34/spherical	-	Stirring	Fe_3O_4 -PEG (commercially obtained) + glutaraldehyde 100 μL + Triptorelin (0.1 mg/mL in DI water, aka 15.3 nmol) + stirring (overnight, 4 ^oC)	Drug delivery and MIR	(Hu et al., 2018)

Table 2.4, continued

Materials			MHNS Properties	Synthesis			Application	Reference
Metal	**Support**	**Polymer**	**Size (nm)/shape**	**Approach**	**Method**	**Procedure**		
Fe_3O_4	-	PEG	~ 15	*In situ*	Coprecipitation	$FeCl_2 \cdot 4H_2O$ and $FeCl_3 \cdot 6H_2O$ (1:2) + DI water (30 mL) + PEG + stirring	Bio separation, drug targeting and diagnostic analysis	(J. Yang et al., 2014)
Fe_3O_4	-	PEG (4arm)	-	*Ex-situ*	Stirring	Fe_3O_4-NH_2 0.2mg + glutaraldehyde 2 mL + anhydrous methanol 38 L + mechanical agitation (12 h, 25 °C) + washing with anhydrous methanol + 4-arm-PEG-NH_2 + stirring (12 h, RT) + $NaBH_3CN$ (100 mg at 4 h interval) + washing + vacuum dying (12 h, 50 °C)	Support for cellulase immobilization	(Han, Wang, et al., 2018)
-	GO	poly (L-lysine)	130/spherical	*Ex-situ*	Stirring	GO (2 mg) + poly (L-lysine) 8 mg + KOH 10 mg + distilled water + vigorous stirring (24 h, 70 °C) + centrifugation to remove poly (L-lysine)	Chemo-photothermal treatment of breast cancer	(Hashemi et al., 2018)

PTT = photothermal treatment, PVP = poly N-vinylpyrrolidone, CMC = carboxymethylcellulose, FA = folic acid, PTX = paclitaxel, Fluorescein isothiocyanate = FITC, CUR = curcumin, PET = Polyethylene terephthalate, EG = ethylene glycol, DEG = diethylene glycol, PAA = polyacrylic acid, DOX = Doxorubicin, CTAB = cetyl trimethyl ammonium chloride.

2.3.2 *In situ* approach

The *In situ* approach is a one-pot grafting process. The approach involves co-fabricating GO-FeNPs and wrapping them with a suitable surfactant or polymer to form an MHNS in a single step. The common methods used in this approach include solvothermal synthesis, thermal decomposition, electrochemical synthesis and coprecipitation are (Dutta et al., 2018; Y. Huang et al., 2018; Kumar et al., 2018; Xinxing Ma et al., 2012; Zubir, Yacou, Motuzas, Zhang, & Diniz da Costa, 2014). According to the literature (Table 2.4), these methods have some drawbacks. Sonochemical ultrasonication and sol-gel methods, for example, have the potential to degrade GO quality (Kumar et al., 2018). The former can result in low output, and the quality of the support is reduced due to intense sonication. Thermal annealing increases defects on GO in the latter case. However, it is worth noting that a moderate amount of defects on GO enhance its solubility, allowing it to serve as a FeNPs stabilizer (Bai & Shen, 2012). Another example is that of the alkaline medium used in the coprecipitation method. It could deplete the functional groups on GO, resulting in a reduction in dispersibility.

Nonetheless, several studies have investigated electrochemical synthesis as a potential method. Generally, there are two possible setups for this method: (i) GO may be assembled on electrodes and then submerge in an electrolytic solution containing FeNPs precursors, or (ii) an electrolytic solution containing GO may be prepared, then immerse iron rods to save as anode and cathode. The latter setup was recently explored by Kumar et al. (2018). They prepared an electrolyte solution using NaCl and DI water and mixed it with an aqueous solution of GO. Two iron rods were then submerged into the solution before passing a pulsating DC voltage (7V) which causes oxidation at the anode (equation 17); at the cathode, H_2O starts reducing (equation 18). As $Fe(OH)_2$ starts forming at the anode due to the OH^- diffusing from the cathode (equation 19), GO is getting attach to it instantaneously. The voltage was removed after few minutes, and the solution was further stirred until the color finally changed from

reddish-brown to black. The color change indicates the formation of Fe_3O_4, resulting from equation 21. To fabricate architecture "c," the GO-FeNPs obtained may perhaps be wrapped with PEG by ultrasonication.

Anode: $Fe \rightarrow Fe^{2+} + 2e^{-}$ (17)

Cathode: $H_2O + 2e^{-} \rightarrow H_2 + 2OH^{-}$ (18)

Diffusion of OH^{-} : $Fe^{2+} + 2OH^{-} \rightarrow Fe(OH)_2$ (19)

Formation of FeOOH: $3Fe(OH)_2 + ½\ O_2 \rightarrow Fe(OH)_2 + FeOOH + H_2$ (20)

Formation of Fe_3O_4: $Fe(OH)_2 + FeOOH \rightarrow Fe_3O_4 + 2H_2O$ (21)

In addition to the electrochemical method, other methods such as solvothermal synthesis and amidation have also been studied. Recently, Han, Luo, et al. (2018) fabricated MHNS with architecture "c" composition for cellulase immobilization by grafting bare FeNPs onto GO and wrapping them with 4arm-PEG via amide formation. Briefly, they heated a mixture of ferrous sulfate heptahydrate, ferric chloride hexahydrate and carboxylated GO for 1h at a temperature of 60 ºC. The mixture was further sonicated for 3 h after adding 4arm-PEG-NH_2. Finally, EDC was added and stirred for 12 h to obtain a black product (MHNS). Figure 2.3 illustrates the schematics for preparing the MHNS. In another effort, a product with high stability in physiological solutions was obtained via solvothermal method (Xinxing Ma et al., 2012). Briefly, the method proceeds by ultrasonicating a mixture of solutions, GO-FeNPs and 6arm-PEG, for a few minutes. EDC was then added to the homogenized solution and further stirred overnight at RT.

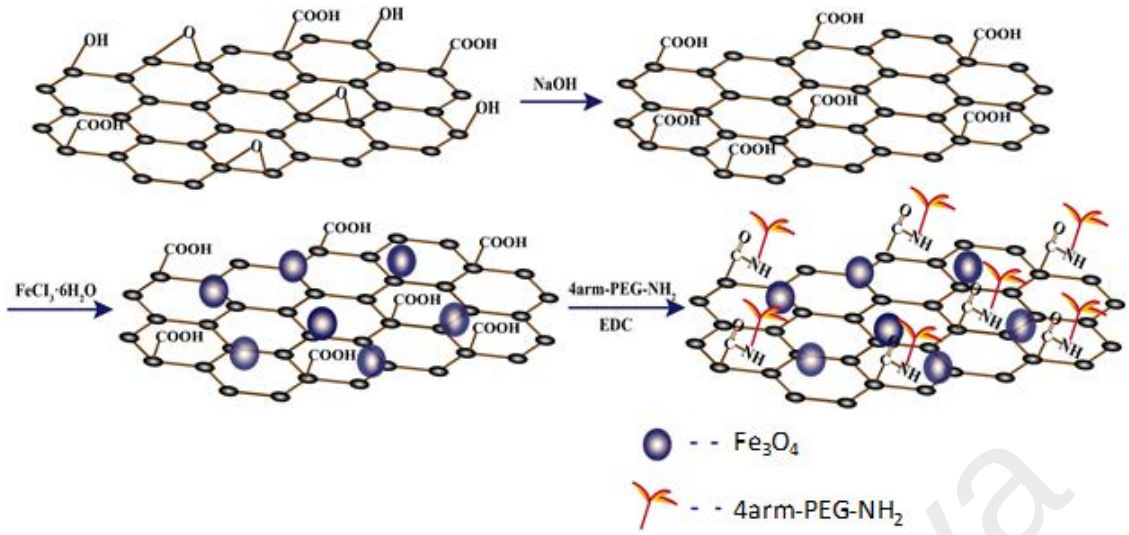

Figure 2.3: Schematic illustration of MHNS preparation via *in situ* ultrasonication method. Reproduced from Han, Luo, et al. (2018), Copyright (2018), with permission from Elsevier.

In summary, the *in situ* method involves one process stage and thus makes it a less time-consuming process and, of course, an added advantage over the *ex-situ* approach. However, unfortunately, the ability to control the size, shape, and morphology is also reduced, making the *ex-situ* approach more appropriate when controlling these characteristics is highly required, as the case is with MHT.

2.4 Characterizing Magnetic Hybrid Nanostructure (MHNS)

To validate the successful preparation of MHNS and to ensure its potentiality for MHT, precise characterization is necessary. Characterization techniques such as X-ray Diffraction (XRD), Fourier Transform Infrared Spectroscopy (FTIR), Scanning Electron Microscopy (SEM), and Vibrating Sample Magnetometer (VSM) have been applied in acquiring information about the elemental-chemical composition, crystal structure, size, magnetic property and other physicochemical properties. In few cases, some of these properties can be assessed by more than one technique; thus, combinatorial characterization augments the

limitations of each technique (Hawkins & Williams, 1992; Santoyo Salazar et al., 2011; X.-F. Zhang, Liu, Shen, & Gurunathan, 2016).

The major parameters studied in the characterization of MHNS are surface chemistry, magnetic behavior and specific absorption rate (SAR). The heating efficacy during MHT is influenced by magnetic behavior (saturation magnetization) and SAR (Kumar et al., 2018). Given the above, investigating these properties is the first step after preparing MHNS. In view of this, the different characterization techniques (with particular emphasis on SAR) necessary for validating the successful preparation of MHNS will be discussed in the following subheadings.

2.4.1 Ligand binding/composition/crystal structure of MHNS

Characterizing the crystal structure, ligand binding, and composition provides the necessary information needed for evaluating the functional aspect of MHNS. The foremost analytical techniques used in ascertaining these properties include FTIR, XRD and Raman spectroscopy. Collectively, the results obtained from these techniques provide synergistic information that augments their mere individual limitation. Each of these techniques may provide more than a piece of information about the MHNS (Tuček et al., 2016). The XRD analysis, for example, provides information on crystalline structure and the mean crystalline gain size. Analyzing the crystal structure mainly relies on the patterns of diffraction. Each MHNS constituent has a diffraction pattern that uniquely determined its identity.

Han, Luo, et al. (2018) studied the crystal structure of GO-FeNPs-PEG using XRD and FTIR techniques. They compare the XRD diffraction pattern of GO, GO-FeNPs, GO-FeNPs-4armPEG5000 and GO-FeNPs-4armPEG10000. From their results presented in Figure 2.4 A, it could be noticed that only one strong diffraction peak, which was consistent with the (002) representation of GO, appeared in carve “a” at 9.8 ^{o,} and it diminishes as PEG and FeNPs are

incorporated. This decline is due to GO poor degree of crystallinity compared to FeNPs (Kumar et al., 2018). The diffraction peaks in curve “b” are similar to curves “c” and “d,” suggesting that the crystal attribute of FeNPs was preserved throughout the grafting process. Also, the presence of PEG did not alter the diffraction peaks, although it is worthwhile to mention that the stretch observed at angles 10 to 30 ^{o} in curves “c” and “d” was caused by the amorphous phase PEG (You et al., 2019).

In summary, Han, Luo, et al. (2018) reveals that the crystal structure of FeNPs would be intact after grafting, indicating successful loading of the FeNPs onto GO nanoplatform. Buttressed by other similar research (Arsalani et al., 2019; Farazi et al., 2018), diffraction peaks between diffraction angle 35 ^{o} to 36 ^{o}, corresponding to (311), are usually the highest reflection. However, their intensities reduce with the presence of GO and PEG.

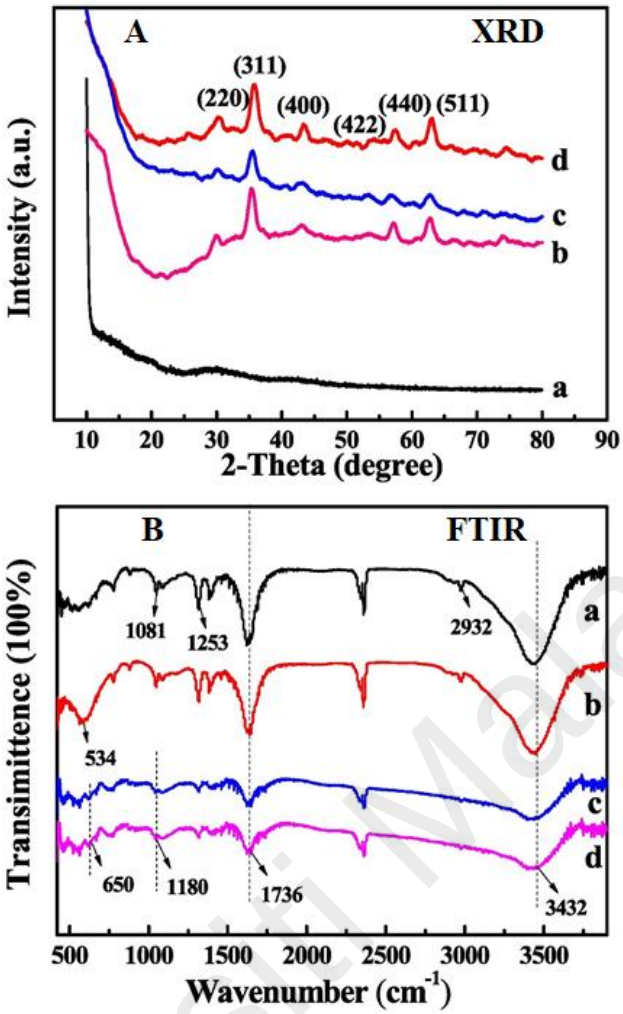

Figure 2.4: XRD patterns and FTIR spectra for (a) GO, (b) GO-FeNPs, (c) GO-FeNPs-4armPEG5000, (d) GO-FeNPs-4armPEG10000. Adapted from Han, Luo, et al. (2018) with permission from Elsevier.

Still on, after successfully confirming the crystal structure using XRD technique, Han, Luo, et al. (2018) further investigates the functional groups present on the MHNS using FTIR technique. The technique is often used to provide information regarding interaction and molecular structure; such information indicates the existing functional groups. The technique usually records spectra generated within the mid-infrared region when the sample absorbs infrared radiation. This record tells the position of bands relative to their nature and strength thus, providing evidence on the specific functional group present. The appearance and disappearance of each functional group have implications.

The study conducted by Han, Luo, et al. (2018) compares the diffraction pattern of GO, GO-FeNPs, GO-FeNPs-4armPEG5000 and GO-FeNPs-4armPEG10000. From the FTIR spectra they reported (presented in Figure 2.4 B), the appearance of Fe-O bonds in curve "b" confirms the covalent grafting of FeNPs onto the GO surface. Vibration peaks at 1736 cm^{-1} that appeared in all the curves were caused by an oxygen-containing functional group of GO (epoxy) thus, indicating the presence of GO. The successful coating of GO-FeNPs surface with PEG was confirmed by $–NH_2$ and C–N peaks (650 and 1180 cm^{-1}) that appeared at similar points in plots "c" and "d". The similarities of these two plots also indicate that the molecular weight of PEG has no substantial effect on the FTIR spectra; although, when the PEG volume is varied, it may alter the spectra (Mohanta et al., 2018). Apart from these studies, other researchers have published papers devoted to MHNS FTIR investigation; this current study reviewed them and presented in Table 2.5 the infrared radiation vibrational assignments for most common functional groups associated with GO-FeNPs-PEG (MHNS).

2.4.2 Size of magnetic hybrid nanostructure

XRD, TEM and SEM are commonly used for characterizing the size of MHNS (Mourdikoudis, Pallares, & Thanh, 2018). These techniques can also be used to provide other information. As mentioned earlier, XRD provides information about crystalline structure. In another instance, TEM can provide information regarding growth kinetics monodispersity and aggregation. The TEM has more advantages than SEM in determining the size of samples because it affords better spatial resolution and gives additional analytical measurements. Its major disadvantage is that the sample preparation takes a longer time.

The two most frequently used techniques in determining size are TEM and XRD. The size obtained from the former is usually larger than the latter, particularly when the MHNS is large

enough (>50 nm) to contain more than one crystal boundary on its surface. Despite this fundamental difference, both techniques generally describe the size of MHNS.

Table 2.5: FTIR vibrational assignments for most prevalent functional groups found in a magnetic hybrid nanostructure containing PEG, GO and FeNPs.

Functional Groups	IR-bands (cm^{-1})	Comments	Reference
O-H	3995-3100	Appearance suggests the presence of absorbed water on the oxide.	(Mohanta et al., 2018; Sahne et al., 2019; Shaghaghi, Khoee, & Bonakdar, 2019)
Fe-O	639/580-570	Appearance indicates the presence of FeNPs on GO.	(Dutta et al., 2018; You et al., 2019; Q. Zhang, Liu, et al., 2017)
C=O	1850-1750/1650-1600	Instigated by the epoxy groups on GO. Intensity decreases; PEGylation is achieved.	(Amani et al., 2019; Anbarasu, Anandan, Chinnasamy, Gopinath, & Balamurugan, 2015; Cao et al., 2019; B. Feng et al., 2008; Iannazzo et al., 2017)
C-N	1460-1291	Indicates bonding of PEG to GO.	(Han, Luo, et al., 2018; Han, Wang, et al., 2018; G. Wang et al., 2018)
C-H	3000-2800/1460-1342	Related to bonds in PEG and suggest PEGylation.	(Hu et al., 2018; Rodrigues et al., 2018; Shaghaghi et al., 2019; Xie et al., 2019)
C=C	1680-1600	Instigated by GO.	(Rodrigues et al., 2018)
C-O	1765-1722/1130-1093	Intensity decreases after PEGylation.	(Amani et al., 2019; Y. Huang et al., 2018; Shaghaghi et al., 2019)
C-O-C	1351-1230/1114-1102	An intense signal shows high PEGylation achieved.	(Amani et al., 2019; Hu et al., 2018; Xie et al., 2019)

The XRD analysis can be used to estimate the mean crystalline gain size via Scherrer's equation (equation 22); often, this equation is erroneously referred to as the Debye-Scherrer's equation (Ganesan et al., 2019; Holzwarth & Gibson, 2011). Analyzing the crystal structure usually depends on the diffraction patterns formed. Each constituent of MHNS has a diffraction

pattern that uniquely defined its identity. From the intense diffraction peaks obtained, the size (up to about 100 – 200 nm) can be estimated using equation 22; this is because peak broadening decreases as the crystalline size increases (Holzwarth & Gibson, 2011).

$$D = \frac{K\lambda}{B\cos\theta} \tag{22}$$

Where:

D = Crystallite size.

K = Crystallite shape factor.

λ = X-ray wavelength.

B = Full width at half-maximum.

TEM analysis was used by Han, Luo, et al. (2018) to study the morphology of MHNS synthesized via an *ex-situ* approach; Figure 2.5 presents the TEM image. Figure 2.5 A shows that the GO nanoplatform was lamellar and had folds that accommodate and promote the uniform attachment of FeNPs (this ability prevents the mutual agglomeration of NPs). In Figures 2.5 C and D, a significant shadow appeared because the PEG layer covered the GO surface. This shows that the PEG modification and the formation of GO-FeNPs-PEG were successful. A similar outcome was reported by Kumar et al. (2018) when they deposited bare FeNPs onto GO nanoplatform via *in situ* approach. Still on, from Figure 2.5, the TEM size could be seen ranging between 10 to 21 nm; it was slightly higher than the estimated XRD size. Generally, within such a range, the MHNS superparamagnetic behavior is preserved. Table 2.4 shows the various sizes and shapes of MHNS reported in the literature. Although some literature reported dendritic and cubic shapes, the majority obtained spherical shapes.

In addition to verifying that MHNS is fabricated successfully, proper characterization could determine the feasibility of MHNS for MHT application. As discussed before, the drawbacks of MHNS in MHT include poor loading of FeNPs onto GO nanoplatform and biocompatibility issues. Improving grafting techniques to optimize FeNPs loading enhances thermal energy generated; thus, the cancer cell can be destroyed in a short period of time. Eventually, this will reduce the quantity of MHNS administered and minimize the possible side effects at the clinical stage (Kumar et al., 2018).

In summary, particle size between 10 – 80 nm is adequate for MHT and other applications like drug delivery. A blockage could occur with larger-sized NPs because their penetration to the target cellular region could be hindered (Mohanta et al., 2018). Besides, NPs above 200 nm size tend to form aggregates in the liver, especially when administered orally. The PEG layer coating is very much helpful in reducing issues like phagocytoses. Optimizing it can keep MHNS in the desired size range, maximize FeNPs loading, and keep its biocompatibility and magnetic property intact (Mohanta et al., 2018).

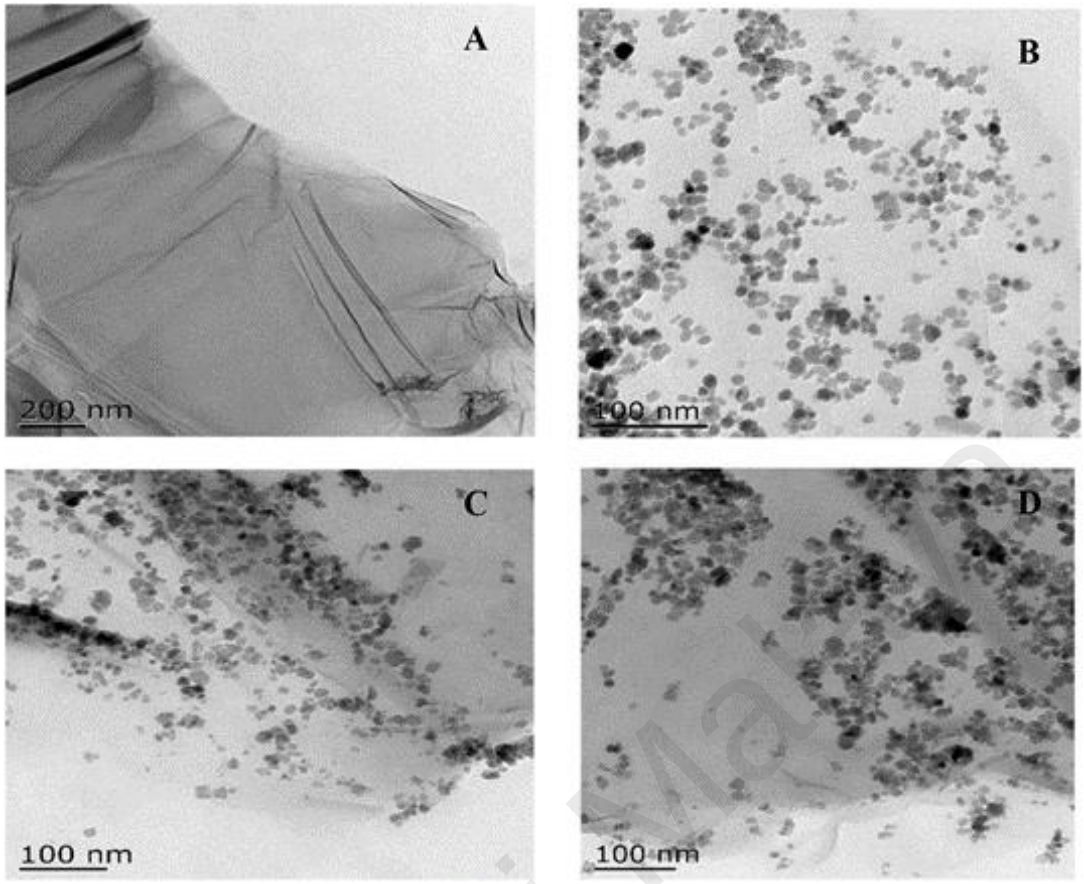

Figure 2.5: TEM images of (A) GO, (B) FeNPs deposited on GO (C) GO-4armPEG5000 modified FeNPs deposited on GO, (D) 4armPEG10000 modified FeNPs deposited on GO. Reprinted from Han et al. (2018), Copyright (2018), with permission from Elsevier.

2.4.3 Magnetic properties of magnetic hybrid nanostructure

VSM analysis is often used to analyze the magnetic properties of MHNS at a specified temperature. The magnetic behavior is primarily due to the FeNPs embedded in the MHNS. As summarized in Figure 2.6, the magnetic properties are defined by the measured coercivity ($H_{C;}$ the amount of external coercive field required to normalize magnetization to zero), remanence (M_r; induced magnetization remaining after removing an applied external magnetic field), saturation magnetization (M_S) and superparamagnetic behavior of the MHNS. Superparamagnetism is the responsiveness of the MHNS to an applied magnetic field without retaining any magnetism after removing the applied field. M_S, on the other hand, is the maximum magnetization obtainable when the MHNS is subjected to an external magnetic field

at a temperature below Curie temperature. The inductive heating property of MHNS could improve with an increase in M_S value (Zhao et al., 2009). It is seen in Figure 2.7 (b) that M_S depends on temperature; it increases as the magnetic dipoles align with the applied field (see "saturation magnetic moment" illustration in Figure 2.6) and could reach its highest value at 0 K where all the thermal vibrations would have significantly diminished (Kolhatkar, Jamison, Litvinov, Willson, & Lee, 2013). The superparamagnetic behavior of FeNPs is preserved below the critical size limit. Generally, increasing FeNPs size beyond the critical limit will improve the M_S (Anbarasu et al., 2015); however, the superparamagnetic behavior may change to ferromagnetic as a result. Typically, FeNPs usually has lower M_S than its bulk form; the M_S of the bulk usually varies between 85 to 100 emu/g (Cabrera, Gutierrez, Menendez, Morales, & Herrasti, 2008; Tai, Lai, & Abdul Hamid, 2016).

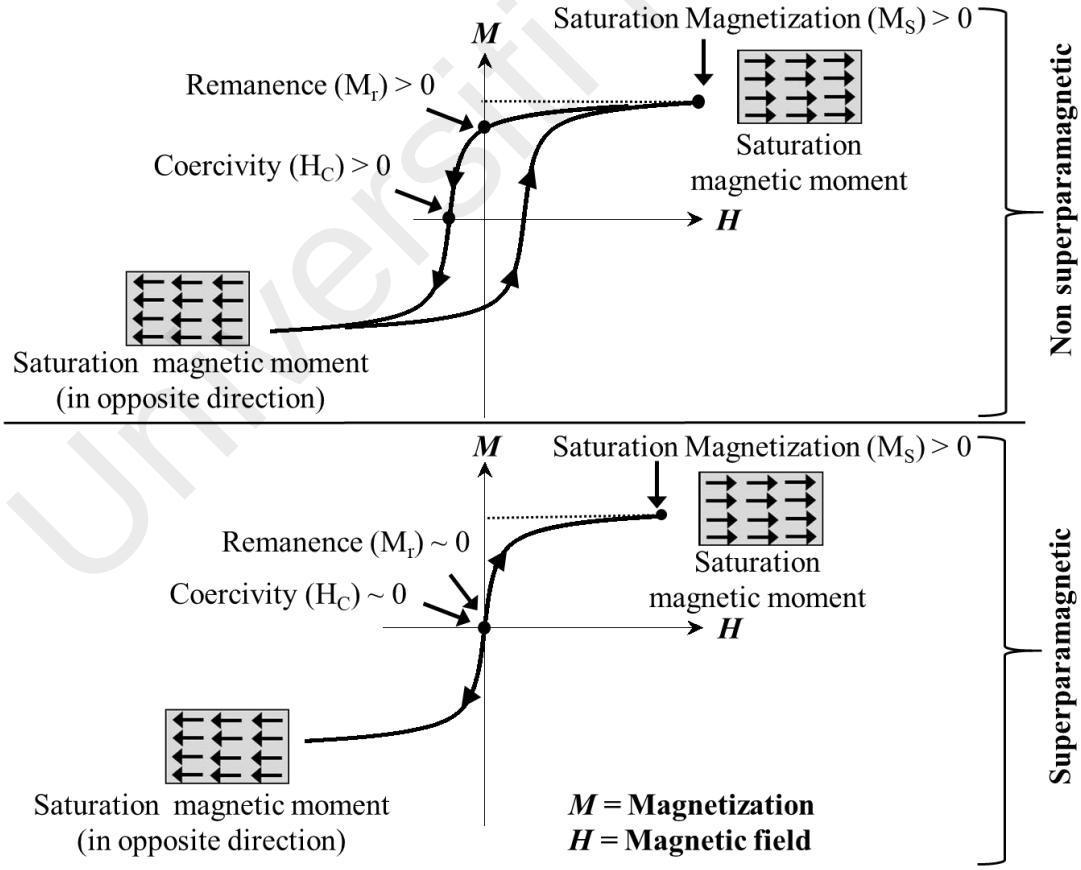

Figure 2.6: Schematic illustration of coercivity (H_C), remanence (M_r), saturation magnetization (M_S) and superparamagnetism.

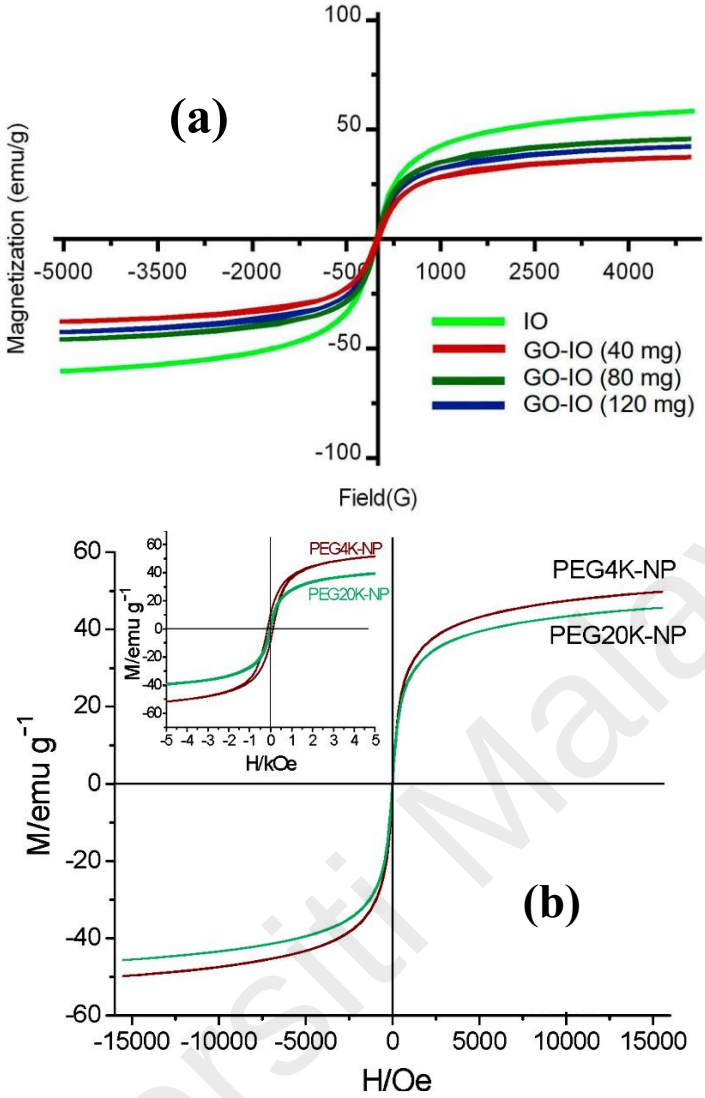

Figure 2.7: (a) Magnetic hysteresis loops for bare FeNPs (OI) loaded onto GO at various amounts. Reprinted from Albert, Abdullah, and Shiroshaki (2018) with permission from Elsevier. (b) Magnetic hysteresis loops for PEG (with different molecular weight) functionalized FeNPs recorded at 80 K (top inset) and 300 K (middle). Adapted from Mukhopadhyay, Joshi, Chattopadhyay, and De (2012). Copyright (2012) American Chemical Society.

Figure 2.7 and Table 2.6 reveal that the M_S of bare FeNPs typically lie within 40 to 80 emu/g and can decline when GO, PEG, and other surfactants are successfully incorporated; this is an indicator of successful grafting. It was demonstrated by Rodrigues et al. (2018) that when bare FeNPs was effectively loaded onto GO nanoplatform, the M_S reduced by almost 10%. Kumar et al. (2018) reported a similar reduction at loading 3:1 (FeNPs:GO); however, it dropped to

37.5% at equal loading (1:1). In another instance, Dutta et al. (2018) recorded 18.3% drop in M_S when FeNPs was successfully modified with PEG. Their observation is consistent with a previous study (Tai et al., 2016). The impact of PEG shape, molecular weight and amount (loading) on magnetic property is further illustrated in Table 2.6. Accordingly, the PEG loading and molecular weight have a more negative impact on M_S than the shape; with star-shaped PEG, the drop in M_S is more significant than linear-shaped PEG. In all cases, a reduction in M_S could be due to diamagnetic property of PEG, cation vacancies, spin canting effects or FeNPs surfaces disorder (Amani et al., 2019; Martinez-Boubeta et al., 2013; Noh et al., 2012; Tai et al., 2016).

According to Tables 2.4, 2.6 and Figure 2.7, the magnetic behavior of MHNS can be influenced by: type of iron precursors used for synthesizing FeNPs; size, shape and amount of FeNPs loaded on GO; shape and molecular weight of PEG; and type of polymer/surfactants used. When subjected to a uniform magnetic field, the magnetization curve of superparamagnetic MHNS will follow an S-shape pattern with an overlapping hysteresis loop. Furthermore, the M_S of MHNS is higher when the size or amount of loaded FeNPs is larger. It may significantly decrease with the successful attachment of FeNPs onto GO nanoplatform and when the amount and molecular weight of polymer/surfactant is increased. Compared with the PEG shape, the latter scenario has more significance in decreasing M_S. Finally, the temperature rise during MHT could be higher for MHNS with a higher M_S value (Ganesan et al., 2019). It is worthwhile to mention that other analytical techniques like Mössbauer spectroscopy or superconducting quantum interference device (SQUID) could provide some information regarding the magnetic behavior of MHNS. However, based on the majority of the literature reviewed, the magnetic behavior of MHNS is widely analyzed with VSM due to its simplicity.

Table 2.6: Saturation magnetization (M_S) of FeNPs before and after modification.

M_S before (emu/g)	**M_S After (emu/g)**	**Decrease (%)**	**Reference**
41 - 82	6.5 - 54	84 - 34	(Sugumaran et al., 2019)
39.6	22.5[a]	43.2	(Han, Luo, et al., 2018)
	15.8[b]	60.1	
42.41	32.2	24	(Amani et al., 2019)
45.0	33	26.7	(Han, Wang, et al., 2018)
49 ± 3	34 ± 5	30 ± 5	(Dabbagh et al., 2019)
55.0	30	45.5	(Shaghaghi et al., 2019)
60.0	16	73.3	(Metin, Aydoğan, & Meral, 2014)
60.6	49.5	18.3	(Dutta et al., 2018)
62.0	51	17.7	(Anbarasu et al., 2015)
63.0	60[c]	4.8	(Khoee, Saadatinia, & Bafkary, 2017)
	58[d]	7.9	
	47.5[e]	24.6	
64.0	48	25	(Farazi et al., 2018)
67.3	43.2	35.7	(Weihong Chen et al., 2015)
71.1	50	29.8	(Q. Zhang, Liu, et al., 2017)
77.7	69.8	10.2	(Rodrigues et al., 2018)
	22.4[f]	71.3	
	43.5[f]	44.3	
78.0	48.8[f]	37.5	(Kumar et al., 2018)
	61.9[f]	20.7	
	66.6[f]	14.7	
80.2	65 ± 2	18 ± 2	(Tai et al., 2016)

a = PEG 5000 MW, b = PEG 10000 MW c = star shaped PEG, d = PEG 1000 MW, e = PEG 2000 MW, f = GO:FeNPs (1:0.5; 1:0.75; 1:1; 1:2; 1:3, respectively), MW = molecular weight.

To sum up the discussions from this literature review section, there is a pressing need to overcome the challenges of using bare FeNPs in MHT, the potential next-generation cancer treatment. All things considered, an effective way proposed to address this is to rationally synthesis a magnetic hybrid nanostructure (MHNS). This could be achieved by functionalizing the FeNPs with a temperature-responsive polymer coating that could undergo conformational changes during MHT and thereafter graft the functionalized FeNPs onto a support material that has a large surface area.

In this study, polyethylene glycol (PEG) and graphene oxide (GO) are chosen as polymer coating and support material, respectively, because of their remarkable physicochemical properties. PEG has stealth characteristics, long safety history in humans, higher thermosensitivity, absence of antigenicity and immunogenicity, and the ability to undergo conformational changes during applications. On the other hand, GO has recently shown efficacy in rendering some hydrophobic MNPs to hydrophilic; acting as dispersing agent to process insoluble materials such as graphite, QD and CNT in aqueous solvent; providing significant electrostatic repulsion against aggregation induced by strong magnetic dipole-dipole interactions between MNPs; compensating the poor dielectric loss of ferrimagnetic iron oxide nanorings; and amplifying the FeNPs ROS generation under the influence of ACMF.

There are various methods for synthesizing and grafting the FeNPs, PEG, GO to form the MHNS. This study will explore the *ex-situ* coprecipitation method because it is green, fast, facile and does not include the use of special or stringent experimental conditions such as elevated temperature or high-pressure vessel. More so, it allows the control of the MHNS characteristics such as morphology, M_S and size, which are relevant to MHT performance.

CHAPTER 3: MATERIALS AND METHODOLOGY

3.1 Materials

All the chemicals and materials used in this study are listed in Table 3.1. They are all supplied by EMC^2 Technology or Biotek Abadi. Except stated otherwise, distilled water was used as solvent throughout the experiment. The equipment used during the syntheses and characterization is presented in Table 3.2.

Table 3.1: List of chemicals and materials used in this study.

Chemicals and Materials	Grade/Purity (%)	Brand
Acetone	≥ 99.5	R&M
Ammonia hydroxide	25	Merck
APTES	≥ 98.0	Sigma-Aldrich
Buffer solutions (pH 4,7 and 9)	MQ 300	Merck
Chloroacetic acid	Synthesis	Merck
EDC	Commercial	Sigma-Aldrich
Ethanol	≥ 99.7	R&M
Graphene oxide nanosheet	99.3	US Research Nanomaterials
Iron II chloride tetrahydrate	EMSURE	Merck
Iron III chloride hexahydrate	EMSURE	Merck
Methanol	≥ 99.9	Friendemann Schmidt
N-Hydroxysuccinimide (NHS)	Synthesis	Merck
Polyethylene glycol	1500 K	Merck
Strong Neodymium magnet bar	N35	EMC^2
Toluene	≥ 99.3	Sigma-Aldrich

EDC = N-(3-Dimethylaminopropyl)-N′-ethylcarbodiimide hydrochloride, APTES = 3-aminopropyl triethoxysilane.

Table 3.2: List of equipment used for the study.

Equipment	Application
For characterization	
Fourier transform infrared spectroscopy (FTIR, Perkin Elmer)	Harmonics
X-ray diffraction (XRD, PANalytical X'Pert Pro powder instrument)	Crystal structure
Vibration sample magnetometer (VSM, Lake Shore 7400 Series)	Magnetic behavior (properties)
Field Emission Scanning Electron Microscope and energy dispersive X-ray (FESEM-EDX, Zeiss Auriga)	Morphology and elemental information
For magnetic hyperthermia therapy performance evaluation	
Alternating current magnetic field (ACMF) generator (Easy Heat 8310, Ambrell, UK)	Magnetic field-induced heating measurements
Fiber optic temperature probe (I652, Luxtron and Fluoroptic, USA)	Temperature measurement
For syntheses	
Dryer (memmert)	Sample drying
Water bath sonicator (Branson, 3200)	Homogenizing solutions
Digital hygro-thermometer probe (VAKIND)	Temperature and humidity measurement
Beakers (SCHOTT Duran: 50, 100 and 250 mL)	Reactions
Vials	Sample storage
Magnetic stirrer (wisestir MSH-20D)	Reactions
pH meter (Mettler Toledo Deita 320)	pH measurement
pH strips (Merck, MColorpHast)	pH measurement
Analytical balance (AND GF-300)	Mass measurement
Fume hood cabinet (IRYAS, Laboratory hood)	Reaction
Water distiller (Favorit W4L)	Distill water generation

3.2 Methodology

Figure 3.1 presents the methodology flow diagram. In line with the first objective of this study, a magnetic hybrid nanostructure (MHNS) composed of FeNPs, PEG and GO was synthesized in a facile four-step coprecipitation *ex-situ* approach: bare superparamagnetic FeNPs was initially synthesis; followed by silanization with APTES and then functionalization with PEG (PEGylation); and lastly, grafting the PEG functionalized FeNPs onto GO nanoplatform to form the MHNS. At each of these stages, the obtained products were characterized as stated in the second objective. For the last objective, performance evaluation, the products with the desired characteristics were subjected to ACMF at various amplitudes (magnetic field strengths) and frequencies. The typical experimental processes proceeded as detailed out in the following subheadings.

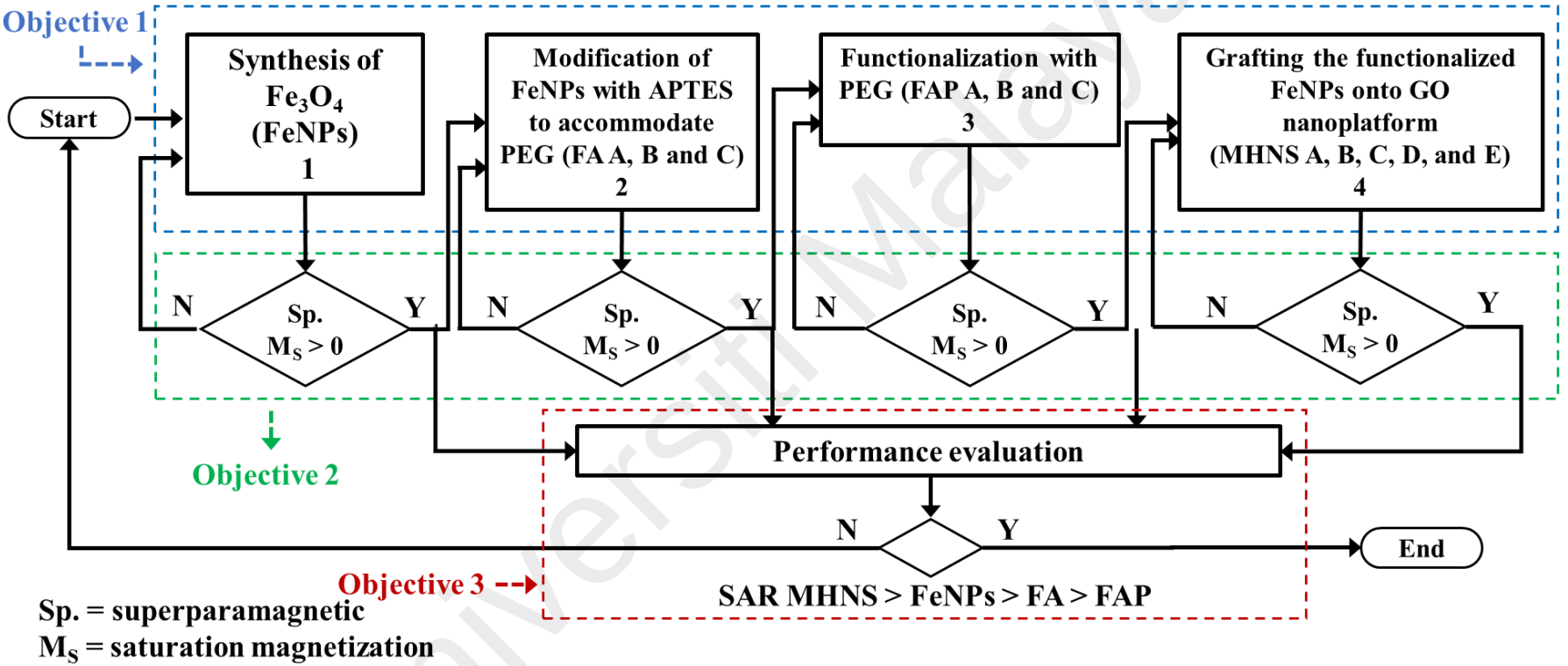

Figure 3.1: Methodology flow diagram.

3.2.1 Magnetic hybrid nanostructure (MHNS) preparation

3.2.1.1 synthesizing FeNPs

Bare superparamagnetic FeNPs were synthesized by a simplified coprecipitation method. A schematic illustration is presented in Figure 3.2 (a). Typically, Iron II chloride tetrahydrate and Iron III chloride hexahydrate were each dissolved in 25 mL distilled water to form a solution (2:3 ratio). The solutions were mixed for 5 min to form a light brown color solution at 700 rpm. The solution pH was then adjusted to ~10 by adding ammonia solution (NH_3 aq). As a result, the color of the solution starts changing to dark brown. The reaction was further continued for 30 min for more effective collision, and a black-colored precipitate (FeNPs) was obtained. The precipitates were collected and washed three times with acetone and distilled water to remove the unreacted precursors and finally dried overnight.

3.2.1.2 functionalizing FeNPs

A graphical procedure for functionalizing bare FeNPs is shown in Figure 3. 2 (b and c). A solvent consisting of toluene and methanol was prepared in an equal volume ratio (50 mL each). The desired amount of the as-prepared FeNPs (5 g, 7 g and 10 g) was dispersed in the solvent and sonicated for 30 min to form a homogeneous solution to which 1.8 g of APTES (~2 mL) was later added. The solution was stirred at 700 rpm for 5 h under ambient atmosphere. The product obtained (denoted as FA A, FA B and FA C) were magnetically separated and washed with acetone and distilled water three times to remove unreacted APTES and then dried overnight at mild condition. Finally, the PEGylation was achieved by dispersing PEG and the silanized FeNPs (at 1:1, 1:2 and 1:3 loading) in 50 mL ethanol and sonicated for 5 min. The solution was further stirred for 24 h at 700 rpm. The suspension was allowed to sediment with the aid of a strong magnet, and the supernatant was discarded. The solid residue was washed three times with acetone

and distilled water to remove the excess surfactant. The final products (PEG-APTES-FeNPs), denoted as FAP A, FAP B and FAP C, were dried at 40 °C for 24 h.

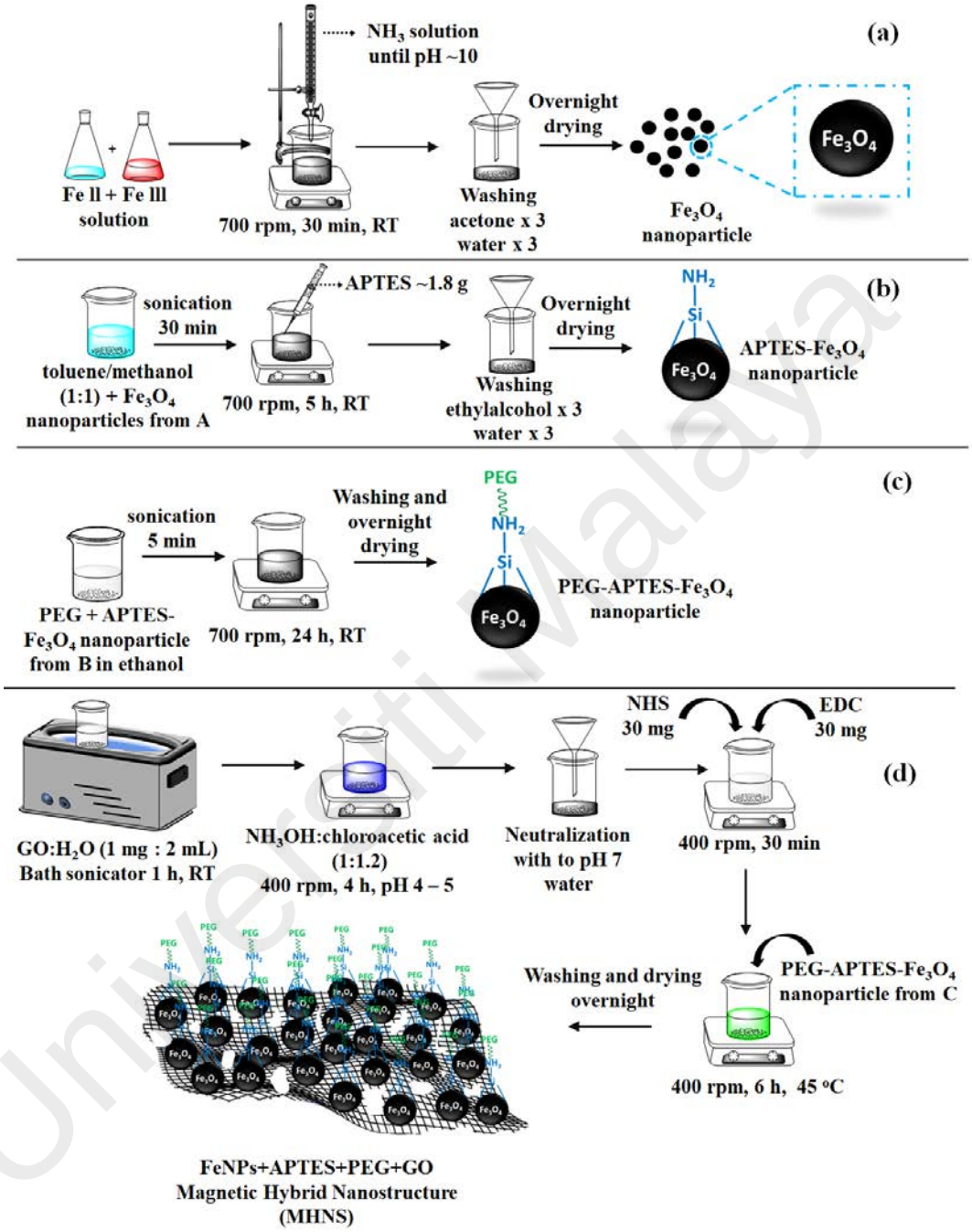

Figure 3.2: The schematic depicts the facile synthesis of FeNPs (a), the functionalization of the FeNPs with APTES and PEG (b and c), and the grafting of the functionalized FeNPs-APTES-PEG onto GO nanoplatform to form the MHNS (d). Appendix A contains images of the synthesized samples.

3.2.1.3 grafting functionalized FeNPs onto GO to form MHNS

Grafting the functionalized FeNPs onto GO nanoplatform to form MHNS proceed as depicted in Figure 3.2 (d). Accordingly, an aqueous solution containing a desired amount of GO was sonicated for 1 h to form a homogenous solution. NH_3OH and chloroacetic acid (ratio 1.0:1.5) were added to the GO suspension and stirred at 400 rpm in other to activate the GO. The pH of the solution was maintained between 4 – 5 (see Appendix B for details on pH variation within the reaction time) and then neutralized with distilled water after 4 h stirring. The activated GO was recovered by filtration. To accommodate the functionalized FeNPs, an equal amount of NHS and EDC (30 mg) were added to the aqueous suspension of activated GO and sonicated for 30 min. After that, the desired amount of functionalized FeNPs (FAP) was added (at 1:1, 1:0.5, 1:2, 1:3 and 1:4 GO:FAP C loadings; denoted as MHNS A, MHNS B, MHNS C, MHNS D and MHNS E respectively; MHNS A is the control). The reaction was continued for 6 h at 45 ºC. Finally, the MHNS formed were recovered by a strong magnetic bar after repeated washing and then dried at 40 ºC overnight.

3.2.2 Magnetic hybrid nanostructure characterization

The magnetic properties (such as the M_S, H_C and M_r) of the synthesized samples were measured at room temperature using a vibrating sample magnetometer (VSM, Lake Shore 7400 Series). The samples were analyzed in powdered form and subjected to a uniform magnetic field, oscillating between ±8 kOe. The Fourier transform infrared (FTIR Perkin Elmer) spectra were recorded between 500 – 4000 cm^{-1} to acquire data regarding the interaction and molecular structure of the samples. The Morphology and elemental matrix were characterized by Field emission scanning electron microscopy and energy dispersed X-ray (FESEM-EDX Zeiss Auriga). The solid powders X-ray diffraction (XRD) studies were performed using XRD PANalytical X'Pert Pro powder instrument. The diffraction

patterns were ascertained at 25 °C, wavelength (λ) of 1.5406 Å, Bragg's angle between 5 – 90 ° with a step size of 0.02 ° and a scan step time 5 – 6 min at 40/40 (KV/MA).

3.2.3 Measurement and evaluation of magnetic hybrid nanostructure (MHNS) performance

In a typical magnetic field-induced heating measurement and performance evaluation illustrated in Figure 3.3, selected samples synthesized from the described protocols were dispersed in the desired solvent (i.e., heating media: glycerol, phosphate buffers and distilled water with different viscosities) and aided with sonication to give a concentration of 0.2 – 20 mg/mL. The selected samples were FeNPs, FA B, FAP C, MHNS A, MHNS B, MHNS C, MHNS D, MHNS E, plain GO and blank solvents (i.e., plain solvents without any hyperthermia material). While MHNS A was used as the control, the last two are references. For each of the prepared samples, 4 mL was poured into a glass vial, with a fiber optic temperature probe inserted (I652, Luxtron and Fluoroptic, USA), the vial was then placed at the center of the coil (8 turns helical, internal diameter 2.54 cm, 4.18 cm long) connected to an ACMF generator (Easy Heat 8310, Ambrell, UK). The temperature of the coil was maintained with a continuous water flow.

The diabatic magnetic field-induced heating measurements proceed at 25 ºC and 52 % relative humidity. The initial temperature was stabilized before exposing the samples to ACMF at five different heating parameters (frequency f = 312 – 320 kHz and field strength H = 15 – 35 kA/m denoted as P1, P2, P3, P4 and P5). As the exposure proceeds, the temperature probe inserted was used to measure the rate change of temperature with time until a maximum temperature rise was reached. The performance of each of the samples, at various measurement parameters (the parameters are summarized in Table 3.3), was estimated using equations 23 – 25 (Lanier et al., 2019). The impact of the

heating medium and background warming was initially removed from the heating curves generated.

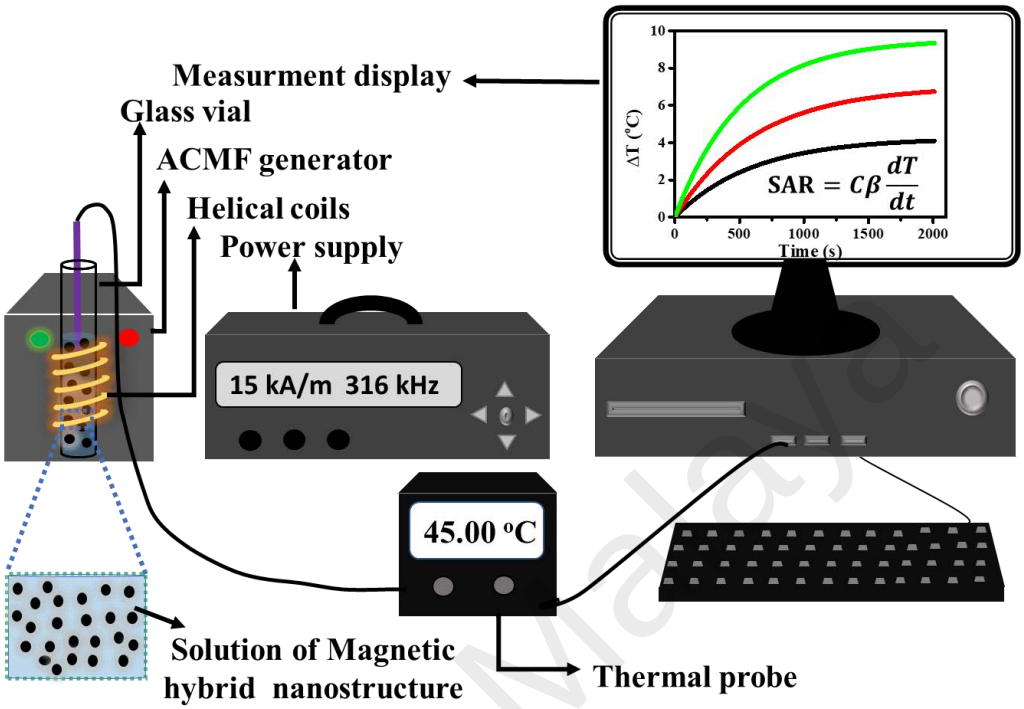

Figure 3.3: Experimental setup illustrating the measurement and evaluation of MHNS performance.

Table 3.3: Summary of parameters modulated during the magnetic field-induced heating measurement and performance evaluation.

Parameters	Value (unit)
Magnetic field strength (*H*)	15, 19, 23, 27 and 35 (kA/m)
Frequency (*f*)	312, 314, 316, 318 and 320 (kHz)
Concentration	0.2, 0.5, 1.0, 1.5, 2.0, 5.0, 10.0, 15.0 and 20.0 (mg/mL)
Viscosity	0.8, 2.7, 4.2,7.2, 33.9 and 612 (mPa.s)
pH	4, 5, 7 and 9
Exposure time	2010 (s)
Heating media	Glycerol, distilled water and phosphate buffers

$$SAR_{\text{Initial slope}} = C\beta\frac{dT}{dt} = \frac{C}{m}\left(\frac{T_X - T_s}{t_X - t_s}\right) \quad (23)$$

$$ILP\ (nHm^2/kg) = \frac{SAR}{f \times H^2} \quad (24)$$

$$\alpha = SAR \times \frac{Hf_{safety}}{Hf_{used}} \quad (25)$$

Where:

$SAR_{\text{Initial slope}}$ = Initial slope-specific absorption rate analytical model.

ILP = Intrinsic loss power.

α = Parameter quantifying SAR relative to *Hf* safety limit.

$\beta = \frac{1}{m}$

C = Specific heat capacity of heating media.

f = Frequency.

H = Magnetic field strength (amplitude).

m = Mass fraction of FeNPs in the heating medium.

$\left(\frac{T_X - T_s}{t_X - t_s}\right)$ = Rate change of temperature with time (*s* is the starting temperature/time and *X* is the stopping temperature/time).

CHAPTER 4: RESULTS AND DISCUSSION

This chapter presents comprehensive and comparative explanations regarding the stagewise preparation of the MHNS, its characterization (using techniques such as VSM, FTIR, FESEM-EDX and XRD analyses) and its MHT performance evaluation.

4.1 Magnetic Hybrid Nanostructure (MHNS) Fabrication

The MHNS was synthesized in a simplified four-step *ex-situ* approach: (i) synthesizing bare superparamagnetic FeNPs, (ii) silanization of the bare superparamagnetic FeNPs with APTES denoted as FA, (iii) functionalizing the FA with PEG denoted as FAP, and finally (iv) grafting the FAP onto GO nanoplatform to form MHNS. All these steps were fine-tuned and performed in sealed beakers and natural atmospheres. Excluding the last step, all the reactions proceed at room temperature (RT), making the reaction relatively facile compared to the literature. Expectedly, no literature exactly matches the described protocols (all the four stages). Hence, a direct comparison could not be made; however, it could be partly (stepwise) match with a few (Table 4.1). Generally, the reactions are green and fast. Most of the reactions presented in Table 4.1 are either carried out at longer period, in inert environment and/or at temperatures above RT. Compromising these have repercussion; it reflects negatively on the MHNS properties, especially magnetic properties like M_S. However, with our facile approach, the property was comparatively high and intact even at lower magnetic field measurements (more discussion under VSM analysis subheading).

Table 4.1: Comparing operating parameters for synthesizing various MHT materials in this work with other literature.

Product	Method					VSM		Size (nm)	Reference
	Temp. (°C)	Time (h)	pH	Inert gas	rpm	Ms (emu/g)	Field (kOe)		
FeNPs	RT	0.5	~10	none	700	68.36	±8	9 – 13	This work
FA	RT	5.5	-	none	700	64.67	±8		
FAP	RT	24	-	none	700	60.89	±8		
MHNS	45	7	4 – 5	none	400	40.76	±8		
FeNPs	80	0.5	-	N_2	-	50	±10	>9	(Y. Liu, Li, Li, & He, 2013)
FA	70	24	-	N_2	-	40	±10		
IONPs	265	2	-	N_2	300	54	±30		
GO-IONPs	80	0.67	-	-	-	6.45 – 18.26	±30	4 – 45	(Sugumaran et al., 2019)
GO-IONPs-PEG	-	24 – 48	-	-	>1000	-	-		
FeNPs	60	~3	10	Ar	-	65.6	±10	40 – 60	(B. Feng et al., 2008)
FA	60	5	-	Ar	-	59.5	±10		
FAP	60	~12	-	Ar	-	39 – 55	±10		
FeNPs	<70	~2	9 – 13	N_2	600 - 1200	41 – 49	±15	10 – 20	(J. Sun et al., 2007)
FeNPs-PEG	<70	~2	-	N_2	-	31 – 40	±15		
FeNPs	200	24	-	-	-	82, 85, 87	±10	217 - 4900	(Fatima, Lee, Yun, & Kim, 2018)
FeNPs	280	2	-	Ar	-	63-80	±10	44	(Dipak Maity et al., 2011)

In the first step, bare superparamagnetic FeNPs precipitates with the addition of NH_3 aq to its premixed precursors. The reaction was aged 30 min for more effective collisions. The precipitating agent was added continuously at a slow rate (0.08 mL/s); adding all at once could result in pH inhomogeneity before achieving complete mixing, affecting the phase transformation (Ahn et al., 2012). During the interval, the solution changed from light brown at pH 3 to black precipitate as the pH approaches 10. The type of precipitating agent used could affect the reaction. Sodium carbonate could slow down the reaction (Cristina Blanco-Andujar et al., 2012). Compared with NH_3 aq, NaOH substantially decreases the M_S; it also influences the size and crystallinity due to pH gradient (R. Y. Hong et al., 2008). With NH_3 aq in the solution, its dissociation into NH_4^+ and OH^- ions are reversible, and the solution pH gradient is maintained at a constant value (Wang et al., 2010). Hence using NH_3 aq can improve the crystallinity, preserve the superparamagnetic size range and increase the M_S. All these correlate with results obtained from XRD and VSM (detail discussion under VSM analysis and XRD analysis subheadings, respectively).

The formation of FeNPs follows a transformation pattern as the pH approaches the basic region: akaganeite phase transforms to magnetite phase (FeNPs) through goethite, hematite and maghemite phases, respectively (Ahn et al., 2012; Das, Hendry, & Essilfie-Dughan, 2011). All these transformations are catalyzed by Fe_2^+ present in the reaction; therefore, Fe_2^+ ion is pivotal for the formation and growth of FeNPs (LaGrow et al., 2019; Rosso, Yanina, Gorski, Larese-Casanova, & Scherer, 2010). These transformations are transient and simultaneous. The physical changes observed during the precipitation (as the NH_3 aq was added, instant formation of some black precipitates was observed) also buttress these points. Nevertheless, further studies should utilize/include *in situ* analyses during the reaction to further support these observations.

The second step involves improving the interfacial behavior of the synthesized bare FeNPs with amine functional group via formation of Fe – O – Si bond with a silane coupling agent (APTES) to accommodate PEG functionalization (PEGylation) in the next stage. As mentioned earlier, these stagewise modifications are necessary to improve FeNPs performance during MHT. Generally, silanization follows a sequence: APTES has three ethoxy groups per molecule and are capable of hydrolyzing into three hydroxyl groups in solvents; and further polycondense with hydroxyl groups from the bare FeNPs (Y. Liu et al., 2013; Yamaura et al., 2004; M. Zhu, Lerum, & Chen, 2012). The reaction fits more with pseudo-second-order kinetic model, and the kinetics is the same with solvents such as ethanol and ethanol-water mixture (Y. Liu et al., 2013). Washing and recovering the APTES modified FeNPs (FA) at the end of the reaction was observed to be more difficult (the process takes more time and could not be achieved via simple filtration method) compared to bare FeNPs obtained at the first stage; hence, the process was aided with a magnet. The difficulty could be due to the fact that the solubility of the bare superparamagnetic FeNPs was improved by APTES (D. Maity, Chandrasekharan, Feng, & Jun, 2010). Nevertheless, the difficulty was much greater during the third stage, where FA was functionalized with PEG.

In the third stage, the PEG functionalized FA (FAP) changed from black to dark brown hydrophilic nanostructure, unlike bare FeNPs, which are less soluble in water (Mukhopadhyay et al., 2012). As discussed previously, agglomerates might cause issues like obstruction of blood vessels, which hampers NPs diffusibility to the desired cellular site during MHT. Interestingly, agglomeration was not observed when the FAP was dispersed in water, acetone, or methanol; this was obvious during the separation and washing steps (even when separation was aided with strong magnets). It is worthwhile to mention that the sedimentation is slower in water than in other solvents. These observations give a glance of evidence for PEGylation and reveal the stable nature of the

FAP in dispersions, which would be beneficial for this study wherein, the hybrid structure is needed to be stable in aqueous and physiological media. The MHNS were finally synthesized in the fourth stage by grafting FAP onto GO nanoplatform. Initially, the GO needs to be activated for effective grafting (L. Zhang, Xia, Zhao, Liu, & Zhang, 2010). These are achievable by incorporating the GO with chloroacetic acid in a strong basic solution (X. Sun et al., 2008). pH range of 4 – 5 favors the activation (see Appendix B for more discussion); in a much lower pH range, the GO is prone to stalking (Zubir et al., 2014).

As discussed in detail under the VSM analysis subheading, when the loading of bare FeNPs, APTES, PEG and GO are modulated, it affects their magnetic behavior; in particular, the M_S reduces when functionalization or grafting is achieved. Herein, this behavior is harnessed in optimizing the stagewise reactions. The results obtained are shown in Figure 4.1. The silanization reaction involves the modification of bare FeNPs with APTES. Different amounts of bare FeNPs (5, 7 and 10 g) were added to 1.8 g APTES to alter the concentration of the solution. Surprisingly, this resulted in a "U-shape" curvilinear pattern as shown in Figure 4.1 a; it implies that the optimum is 7 g FeNPs loading (FA B) and was used for the PEGylation stage.

At the PEG functionalization stage, the loading of PEG to FA B was varied (1:1, 1:2 and 1:3), and as a result, an upside-down "U-shape" curvilinear pattern was obtained (Figure 4.1 b). When compared to the silanization stage, this behavior is inverse (Figure 4.1 a). Therefore, FAP C loading emerged as the optimum, and it was used for the final stage (grafting FAP onto GO nanoplatform).

To finally fabricate the MHNS, various amount of FAP C was grafted onto GO nanoplatform loading 1:1, 1:0.5, 1:2, 1:3 and 1:4 (GO:FAP C). The resultant products were denoted as MHNS A, MHNS B, MHNS C, MHNS D and MHNS E, respectively

(MHNS A is the control). It is seen from Figure 4.1 c that varying FAP C loading causes 27 – 63 % reduction in M_S, which corresponds with the literature (X.-J. Feng et al., 2021; Işıklan, Hussien, & Türk, 2021). As noted previously, the ability of MHNS to generate heat during MHT is attributed to its magnetic properties, which is primarily due to the FeNPs embedded. Therefore, clustering a high amount of FeNPs within the MHNS could amplify the heating ability. In this context, the optimum loading is MHNS E (these findings were later validated during the magnetic field-induced heating measurement and evaluation). To summarize the above discussions, Figure 4.1 d illustrates the optimum fabrication of MHNS in terms of M_S and loading.

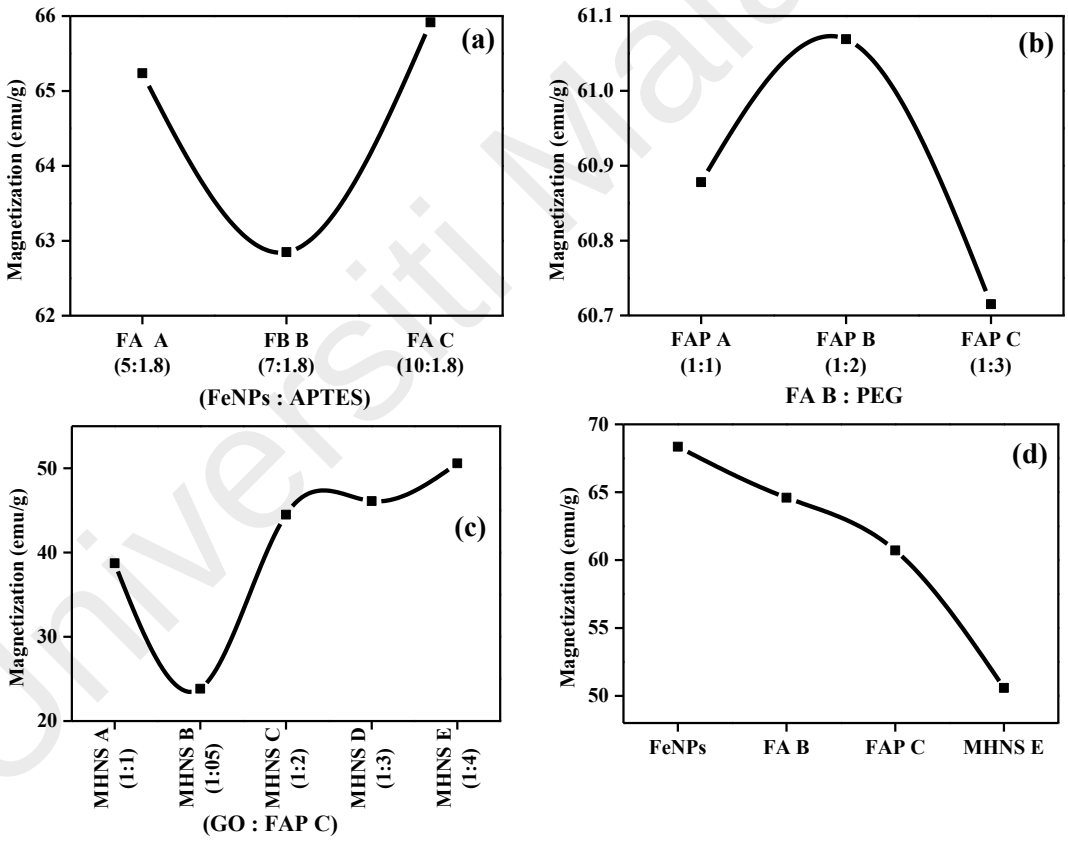

Figure 4.1: Optimization pattern for (a) silanization of the bare FeNPs with APTES denoted as FA, (b) functionalizing the FA with PEG denoted as FAP and finally, (c) grafting FAP onto GO nanoplatform denoted as MHNS and (d) the optimum FeNPs, FA, FAP, and MHNS.

4.2 Characterization of Magnetic Hybrid Nanostructure (MHNS)

4.2.1 Vibrating Sampling Magnetometer (VSM) analysis

The magnetic properties of all the samples obtained were analyzed using VSM analysis at 300 K. The hysteresis loop for each *ex-situ* stage is shown in Figure 4.2. Figure 4.3, on the other hand, summarizes the optimum hysteresis loop, M_S, H_C, and M_r; more details can be found in Appendix C. The pivotal magnetic properties are superparamagnetism, M_S, H_C, and M_r, and they are all temperature-dependent (Mukhopadhyay et al., 2012; Revathy, Varma, & Surendran, 2021). For example, thermal vibrations are significantly low at 0 K; therefore, M_S increase may reach a maximum value when magnetic dipoles align with the applied field (Kolhatkar et al., 2013). In addition, the amount of FeNPs, APTES, PEG, and GO in the reacting solutions could also affect the magnetic properties.

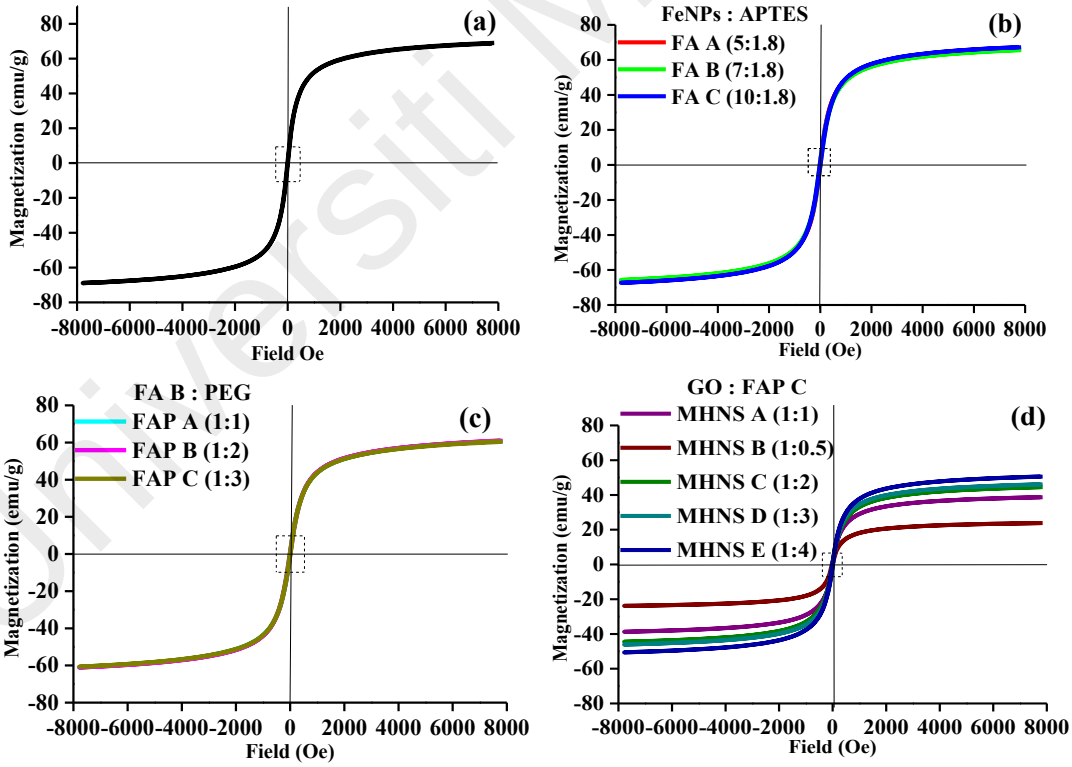

Figure 4.2: VSM magnetization curves for FeNPs (a), APTES modified FeNPs (b), PEG functionalized FeNPs-APTES (c) and FeNPs-APTES-PEG grafted onto GO nanoplatform (d).

As illustrated in Figure 4.2 and Appendix C, all the forward and backward magnetization curves overlapped completely and follow a sigmoidal pattern (S-shape)

with negligible H_C, and M_r; these are indications of superparamagnetic behavior. As illustrated in Appendix C, the maximum H_C coercivity recorded was ca. 10 Oe (sample FA A), and it is much less than ca. 330 Oe reported elsewhere (X. H. Liu, Liu, & Zhang, 2017; Mukhopadhyay et al., 2012); as for the M_r, the maximum was ca. 0.946 emu/g (sample FA A) which is just 4 % of the lowest M_S recorded. At average (considering all samples at varying ratios), M_S values of 68.36 emu/g, 64.67 emu/g, 60.89 emu/g and 40.76 emu/g were recorded for FeNPs, FA, FAP and MHNS, respectively (this indicates that almost 5% APTES and 6% PEG coating was achieved). This decreasing pattern indicates successful functionalization and grafting (X.-J. Feng et al., 2021; Işıklan et al., 2021).

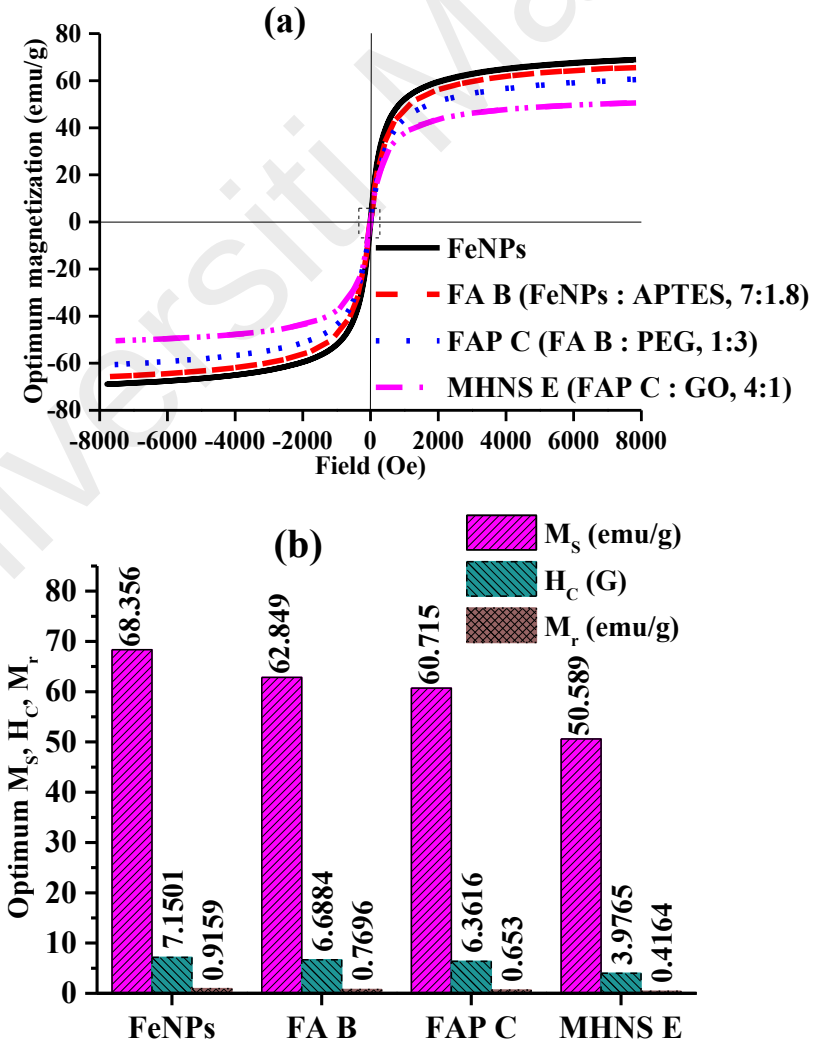

Figure 4.3: Optimum (a) magnetization curve and (b) M_S, H_C and M_r.

Interestingly, the M_S reported in this work is relatively high compared with other reports (Table 4.1). However, few studies reported M_S of almost 70 to 87 emu/g within the size range of 30 – 4900 nm. These nanostructures were synthesized at stringent reaction conditions (temperature 60 – 240 ^oC; time 3 – 24 h; and under N_2 or Ar atmosphere), and the M_S were measured at a relatively higher applied field (±10 k to ±20 k). Such conditions yielded samples with larger sizes and M_S. Further observing the trends, M_S is enhanced with increased particle size; large volume and size could induce bulk FeNPs behavior. However, when the critical size (Dp) is exceeded, the superparamagnetic behavior is compromised (the particles will retain magnetization after removing the applied external field). Thus, a limitation for MHT application.

Accordingly, from the literature surveyed, the M_S obtained herein were well enough for MHT. Furthermore, it was shown that change in magnetic properties is either due to changes in size, surface state, surface disorder or diamagnetic nature of the incorporated particles such as GO nanoplatform (Disch et al., 2012; Fatima et al., 2018; S.-W. Kim et al., 2019; Tan, Zhuang, Peng, & Li, 2008; Yamaura et al., 2004). Since FeNPs size was maintained during the modifications, the reduction in M_S indicates successful functionalization and grafting processes. This also correlates with observations from the XRD and FTIR analyses (more discussion under the headings).

Still on, as a result of varying FeNPs, APTES, PEG and GO loading, the concentration of the reacting solutions changed. It reflects in the degree of silanization, PEGylation and grafting as illustrated in Figure 4.1 and Appendix C. Increasing FeNPs loading lowers the ratio of APTES in the solution; the degree of silanization forms a “U-shape” curvilinear pattern with the measured M_S. The optimum silanization is at the vertex (FA B). As for the PEGylation, an opposite pattern was formed, implying that FAP C is optimum; therefore, it was grafted onto the GO nanoplatform to form the MHNS.

Summing up evidence from Table 4.1 and the discussions from the preparation stages and magnetic studies (VSM analysis), the magnetic properties of FeNPs will be affected by the ratio of ions in solution (Fe_2^+ and Fe_3^+), the precipitating agent used (NaOH or NH_3OH), reaction temperature, amount of the FeNPs embedded in MHNS, and applied field during the magnetic measurements. When effective collisions between Fe_2^+ and Fe_3^+ are hindered, M_S declines; for example, Na^+ ions from NaOH could limit the collisions since it increases the electropositive nature of such solutions (R. Y. Hong et al., 2008). As the embedded FeNPs loading is higher, the M_S also increases (Figure 4.1 c); hence, M_S is proportional to the amount of FeNPs (X.-J. Feng et al., 2021; Işıklan et al., 2021).

Furthermore, as illustrated in Appendix C, the M_S, H_C and M_r of all samples are in good agreement upon successful fabrication. Also, the magnetization curves follow an "S-shape," indicating superparamagnetic behavior. The devaluation of M_S indicates distortion in the crystalline and magnetic order. Finally, it is interesting to mention that all the samples have enough magnetic response (Appendix A).

4.2.2 X-ray Diffraction (XRD) analysis

XRD analysis was performed to acquire information regarding the crystalline structure, particle size and phase mixture of all the synthesized samples. Figure 4.4 presents the diffraction patterns formed. The diffraction patterns for FeNPs were indexed at 30.12, 35.48, 43.12, 57.03, 62.63 and 74.10 °. These peaks correspond to (220), (311), (400), (511), (440) and (533) crystallographic planes, respectively (Halilu et al., 2021). The crystallographic parameters are (i) lattice constant a_0 = 8.33 Å (ii) *d*-spacings: d (220) = 2.96, d (311) = 2.53, d (400) = 2.10, d (511) 1.61, d (440) = 1.48 and d (533) 1.28 Å. As observed, all the prominent diffraction peaks that appeared in FeNPs (Figure 4.4 a) compares with that of FA, FAP and MHNS (Figure 4.4 b – d). These similarities imply that the crystal attribute of FeNPs was preserved throughout the stagewise modification

processes. Nevertheless, the peculiar peak that appeared around 25 to 29 ° in Figure 4.4 (c) was due to the amorphous phase PEG (Mukhopadhyay et al., 2012; Sarı, Biçer, & Alkan, 2020; You et al., 2019). This shows that the functionalization of FeNPs-APTES (FA) with PEG (FAP) was successful.

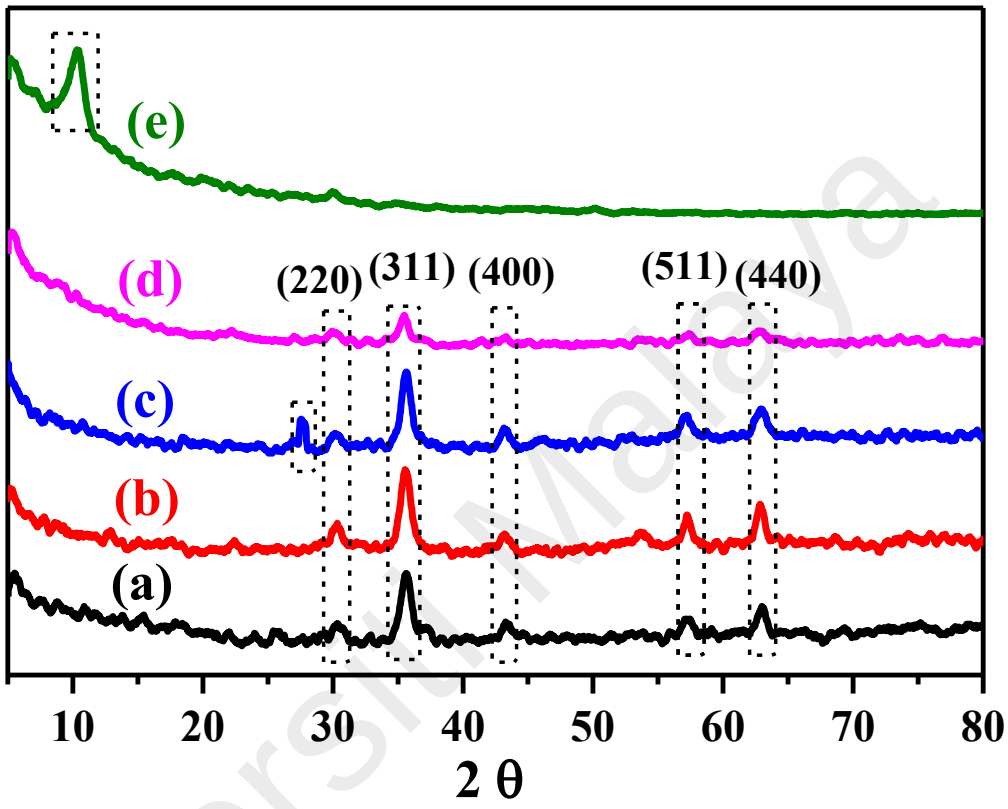

Figure 4.4: XRD patterns for FeNPs (a), APTES modified FeNPs (b), PEG functionalized FeNPs-APTES (c), FeNPs-APTES-PEG grafted onto GO nanoplatform (d) and plain GO nanoparticle (e).

In Figure 4.4 e, only one strong diffraction peak appeared at around 10°, which is consistent with the (002) representation of GO nanoplatform. As observed, it disappeared after grafting FAP onto GO (Figure 4.4 d); this could occur because GO has poor crystallinity compared to FeNPs (Kumar et al., 2018). Generally observing Figure 4.4, the diffraction peaks around diffraction angle 35 ° are the highest reflections but their intensities reduced with the presence of GO (Figure 4.4 d), indicating successful grafting. This observation is in line with similar literature (Arsalani et al., 2019; Farazi et al., 2018).

Furthermore, from the intense peaks obtained, the average particle sizes were estimated using Scherrer's equation (equation 22). They were found to be ca. 9.24, 10.37, 11.97 and 12.25 nm for FeNPs, FA, FAP and MHNS, respectively. These sizes are much less than the critical size (~26 nm), and hence they are within the safe limit for superparamagnetic behavior (Yamaura et al., 2004). As discussed earlier, the sigmoidal pattern from the VSM analysis also demonstrates this behavior. Although the sizes of the functionalized FeNPs and MHNS increased, the M_S dropped instead of increasing. The increase in size shows the incorporation of other particles, while the M_S drop is attributed to the diamagnetic nature of the incorporated particles. In summary, the XRD analysis confirmed the modification of FeNPs with APTES, PEG and its subsequent grafting onto GO nanoplatform without altering its crystal structure, ensuring its ability to respond to ACMF as a potential MHT agent.

4.2.3 Field Emission Scanning Electron Microscope (FESEM) and Energy Dispersive X-ray (EDX)

Figure 4.5 presents the morphology and elemental matrix of FeNPs, FA, FAP and MHNS. As shown therein, there is significant similarity in (a), (b), (c) and (d), implying that a homogeneous phase MHNS is formed. On a similar note, the EDX elementary matrix confirms the four-step *ex-situ* synthesis approach: the presence of only O and Fe in Figure 4.5 (a), pure FeNPs synthesized; the appearance of Si and C in Figure 4.5 (b), attributed to silanization of the pure FeNPs with APTES; the disappearance of C and N in Figure 4.5 (c) due to PEG functionalization; and lastly, the appearance of C and increase in O weight % as a result of the GO carbon-based support (Amir, Halilu, Julkapli, & Ma'Amor, 2020; Mondal, Anweshan, & Purkait, 2020).

In a nutshell, the morphologies and elemental matrixes in Figure 4.5, which correlate with the XRD pattern (Figure 4.4) and FTIR spectra (Figure 4.6), indicate the formation

of FeNPs-APTES-PEG-GO (MHNS). Hence, the desired magnetic hybrid nanostructure (MHNS) is successfully synthesized.

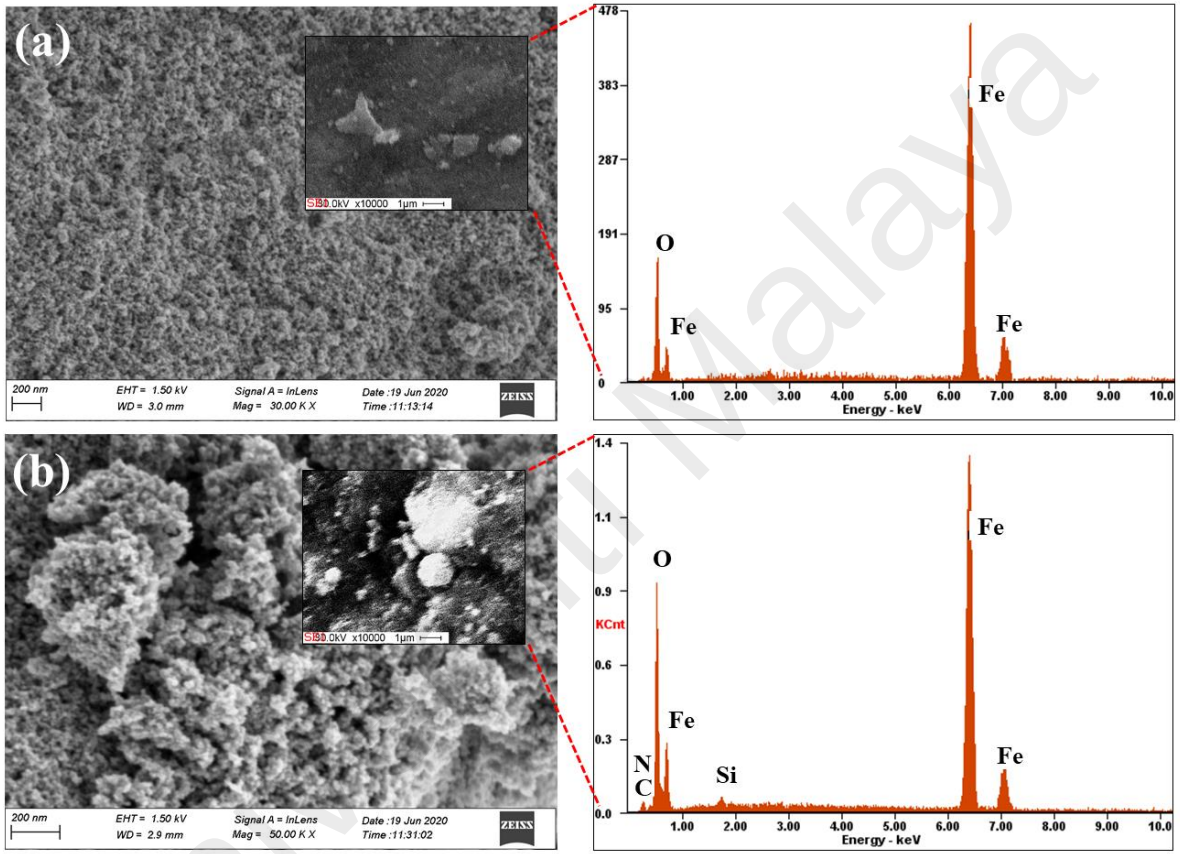

Figure 4.5: FESEM-EDX images of FeNPs (a), APTES modified FeNPs (b), PEG functionalized FeNPs-APTES (c), and FeNPs-APTES-PEG grafted onto GO nanoplatform (d).

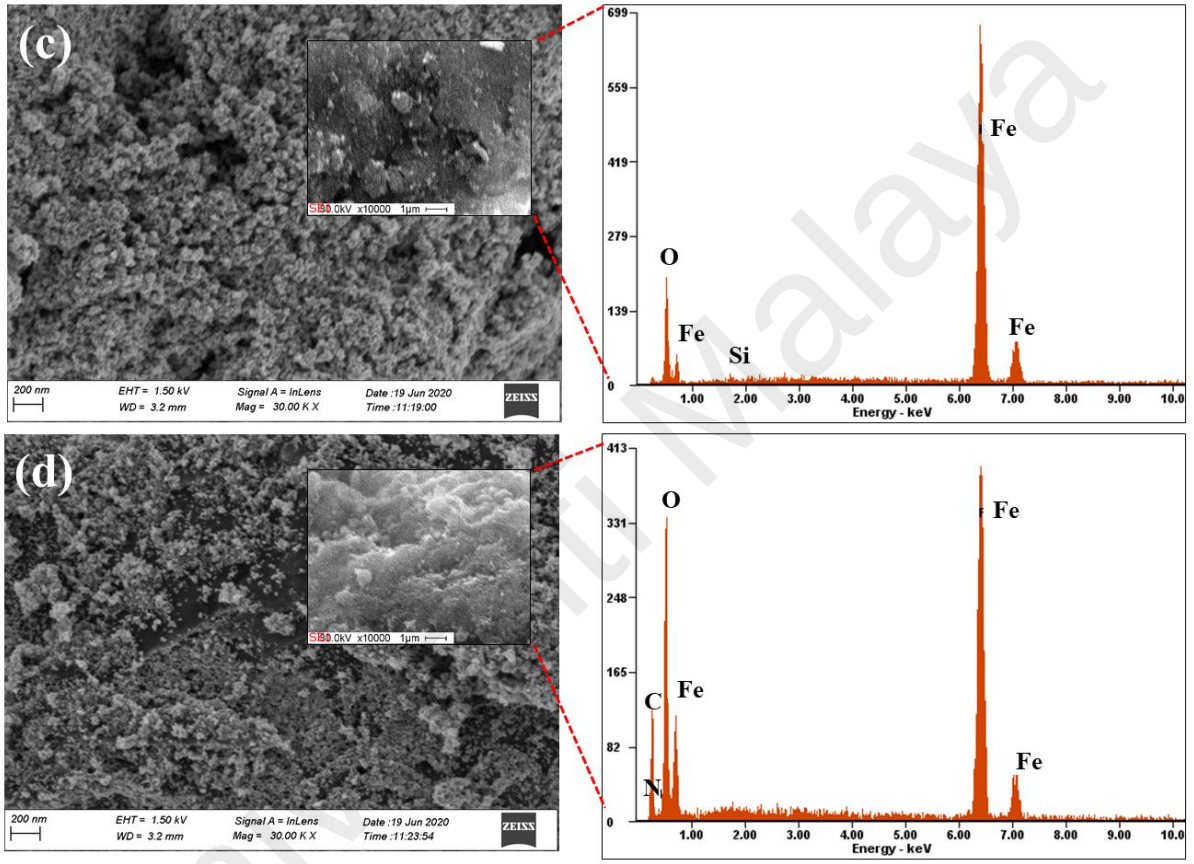

Figure 4.5, continued

4.2.4 Fourier Transform Infrared Spectroscopy (FTIR) analysis

Figure 4.6 and Appendix E presents the FTIR spectra for APTES, FeNPs, FA (FeNPs-APTES), PEG, FAP (FeNPs-APTES-PEG), GO and MHNS (FeNPs-APTES-PEG-GO). The presence of magnetite (O – Fe – O vibration) in all the samples was confirmed by the appearance of two absorption bands around 550 and 578 cm^{-1} in Figure 4.6 (Mukhopadhyay et al., 2012; Yamaura et al., 2004). Expectedly, these bands should not be found in APTES and GO spectra as observed therein. Additionally, the possible perturbation occurring at the diagnostic region of the FeNPs spectra (3180 and 3448 cm^{-1}) is ascribed to the stretching vibration peak of hydroxyl, resulting from the water adsorbed by FeNPs (R. Y. Hong et al., 2008; J. Sun et al., 2007). The formation of FA via Fe – O – Si bond between FeNPs and APTES appears at around 1082 and 808 cm^{-1} (B. Feng et al., 2008; Y. Liu et al., 2013).

The absorption at around 1480 cm^{-1} and 1280 cm^{-1} (– CH and C – C stretching, respectively) indicates the existence of PEG in FAP spectra (X. Yang, Yang, Wu, Yang, & He, 2020). Observing the spectra of the final product, MHNS, and the pure GO, similar vibration peaks appeared in both curves. The vibration peaks at 3438, 2975, 1730 and 1636 cm^{-1} corresponds to – OH, C – H, C = O and C = C stretching vibrations of the GO nanoplatform; for example, the C = O was instigated by the oxygen-containing functional group on the basal plane of the GO nanoplatform (Cao et al., 2019; Han, Luo, et al., 2018). Overall, this analysis agrees with the comments in Table 2.5 and indicates the successful functionalization of bare FeNPs with APTES, PEG and its subsequent grafting onto GO nanoplatform (MHNS).

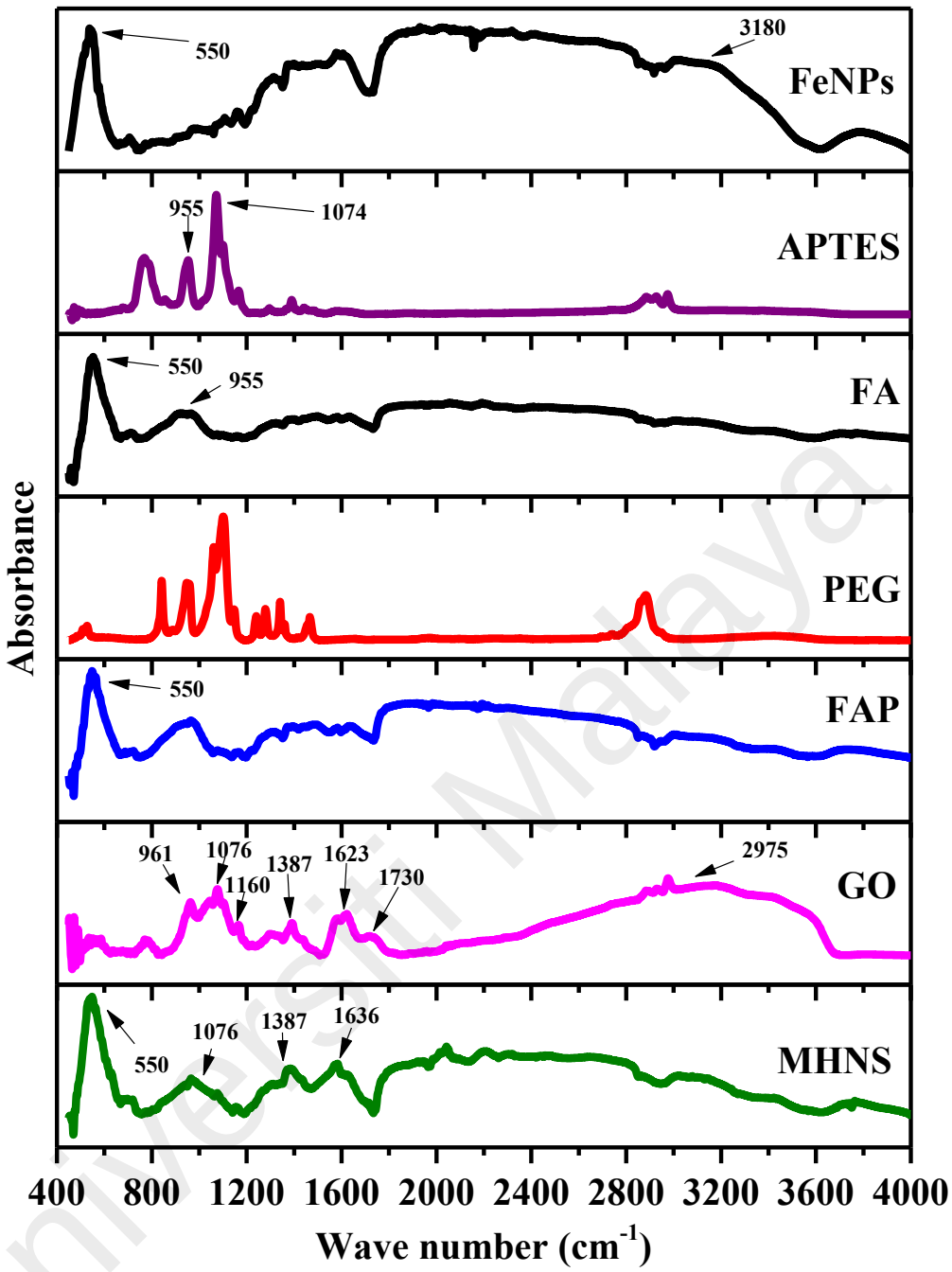

Figure 4.6: FTIR spectra for APTES, FeNPs, APTES modified FeNPs (FA), PEG functionalized FA (FAP), FAP grafted onto GO nanoplatform (MHNS) and plain GO nanoparticles (GO).

In a nutshell, these results (FTIR spectra; XRD diffraction patterns; VSM hysteresis loops; and FESEM-EDX morphologies and elemental matrixes) provided synergetic information that indicates the successful fabrication of superparamagnetic FeNPs-APTES-PEG-GO (MHNS). Hence, the desired MHNS with a potential capability of responding to ACMF is successfully synthesized. Notwithstanding, as mentioned earlier,

understanding the performance of the MHNS under the influence of ACMF is a major challenge to assure its efficacy for MHT and other similar applications. Therefore, the performance (quantified by SAR) of bare superparamagnetic FeNPs, FA, FAP and MHNS in an ACMF were examined to understand their guided heating phenomena in MHT.

4.3 Performance of Magnetic Hybrid Nanostructure (MHNS) under the Influence of Alternating Current Magnetic Field (ACMF)

In an ACMF, an MHNS that has superparamagnetic characteristics undergoes Néel and Brownian relaxations; consequently, the temperature of its immediate vicinity raises. The heat generated between 5 – 10 ^{o}C temperature rises could selectively destroy cancer cells without harming the healthy cells. This is the basic concept of MHT (Albarqi et al., 2019; Ganesan et al., 2019). It worth mentioning that a direct current magnetic field is insignificant for this procedure because the applied magnetic field has a constant direction (Prasad et al., 2013).

Herein, magnetic field-induced heating measurement and evaluation were carried out with samples listed in Table 4.2 to estimate their MHT performance. The results obtained are discussed in this section. In line with the aim of the current study, successfully synthesized MHNS should generate optimum heat when exposed to an ACMF compared to the commonly used modified FeNPs. The heating efficiency of such MHT material is estimated by SAR. Experimentally, to quantify SAR, a solution of MHNS in the desired solvent (heating medium) with a known specific heat capacity is prepared and then subjected to an ACMF at a specific magnetic field strength and frequency (heating parameters). As the heating progresses, a heating curve is generated by recording the rate change of temperature with time within the heating medium for a period of time. From the data set generated, the SAR will finally be estimated using equations 23 – 25.

Table 4.2: Full description of samples used during MHT performance evaluation.

Sample	Description
FeNPs	Bare Fe_3O_4 nanoparticles.
FA B	Bare FeNPs modified with (3-Aminopropyl)triethoxysilane (APTES) at 7:1.8 g FeNPs to APTES loading.
FAP C	FA B functionalized with PEG (polyethylene glycol) at 1:3 FA B to PEG loading.
MHNS A	FAP C grafted onto GO (graphene oxide) nanoplatform at 1:1 GO to FAP C loading (the control).
MHNS B	FAP C grafted onto GO (graphene oxide) nanoplatform at 1:0.5 GO to FAP C loading.
MHNS C	FAP C grafted onto GO (graphene oxide) nanoplatform at 1:2 GO to FAP C loading.
MHNS D	FAP C grafted onto GO (graphene oxide) nanoplatform at 1:3 GO to FAP C loading.
MHNS E	FAP C grafted onto GO (graphene oxide) nanoplatform at 1:4 GO to FAP C loading.
Plain GO	GO (graphene oxide) without FAP C loaded.
Blank solvents	Plain solvents (glycerol, distilled water and phosphate buffers) without any hyperthermia material.

4.3.1 Preliminary performance evaluation

Preliminary studies were conducted to observe the influence of specified frequency *f*, magnetic field strength *H* (amplitude) and heating time (exposure time) during the magnetic field-induced heating measurement.

4.3.1.1 influence of frequency *f* and magnetic field strength *H*

To evaluate the influence of specified *f* and *H* during magnetic field-induced heating measurement, MHNS was subjected to an ACMF at five different heating parameters: *f* = 320, 318, 316, 314 and 312 kHz, and *H* = 15, 19, 23, 27, 35 kA/m denoted as P1, P2, P3, P4 and P5, respectively. The SAR was estimated at each of these heating parameters and correspondingly normalized by the applied *f* (SAR_f) and *H* (SAR_H). Closely observing the patterns in Figure 4.7, it appears that SAR is almost independent of *f* compared to *H*. Hence the heating *f* was maintained at 316 kHz while varying *H* between 15 to 35 kA/m throughout the performance evaluation. This behavior is similar to the observations made by Muela et al. (2016); they investigated the SAR of magnetosomes using a homemade ACMF magnetometer and found that SAR is nearly independent of *f* applied and will continue to rise at $H > 10$ kA/m and possibly remains constant beyond 30 – 35 kA/m.

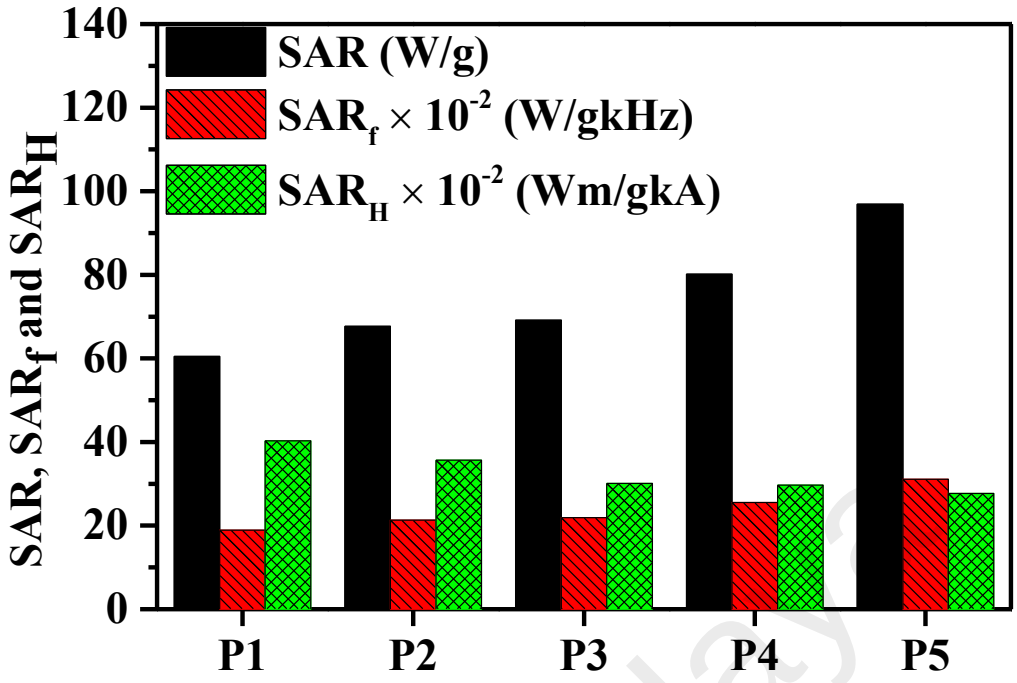

Figure 4.7: SAR varying with five different *f* (320, 318, 316, 314 and 312 kHz) and *H* (15, 19, 23, 27, 35 kA/m) denoted as P1, P2, P3, P4, and P5, respectively applied during magnetic field-induced heating measurement. Comparing with SAR, *f* normalized SAR (SAR$_f$) rises in the same manner while *H* normalized SAR (SAR$_H$) deviates inversely.

4.3.1.2 heating time (exposure time)

The MHNS heating curves presented in Figure 4.8 were obtained from magnetic field-induced heating measurement at *f* = 316 kHz while varying *H* between 15 – 35 kA/m. It can be seen that the rate change of temperature with time were all increasing in a similar pattern: a rapid linear rise in temperature until about 360 s; beyond this point, the rise was slower because of heat loss to the surrounding; and finally, at higher time scale, > 1260 s, a constant temperature change was observed and hence, the maximum temperature rise is reached. These show that 300 to 400 s is sufficient for estimating SAR using equation 23, which is consistent with the literature (Dutta et al., 2018; Rego et al., 2019; Yu et al., 2020).

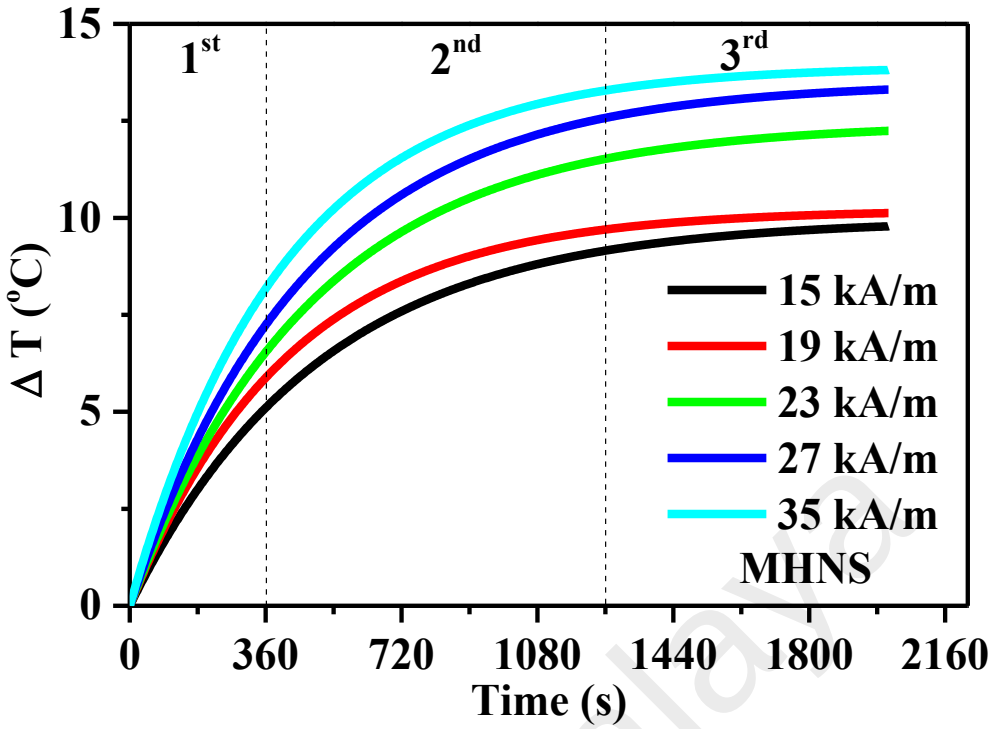

Figure 4.8: Heating curves for MHNS at different *H*. The curve can be sectioned into three intervals: rapid linear rise (0 – 360 s), slow rise (360 – 1260 s), and finally, constant rate (> 1260 s).

4.3.2 Performance evaluation of magnetic hybrid nanostructure (MHNS)

4.3.2.1 MHNS heating curves

Figure 4.9 presents the heating curves for FeNPs, FA B, FAP C, MHNS A, MHNS B, MHNS C, MHNS D, MHNS E and plain GO (full description is summarized in Table 4.2). They were obtained from magnetic field-induced heating measurement at five different heating parameters (f = 316 kHz and H = 15, 19, 23, 27, 35 kA/m). The four main observations from these curves are as follows: (i) all samples were able to cause a linear rise in temperature of their immediate vicinity at all heating parameters (for at least the first 360 s) except the control, plain GO nanoplatform; (ii) the negative behavior of the plain GO indicates its inability to generate or dispense heat, implying that FeNPs was successfully embedded in all the other samples (these conforms with results form the VSM, FTIR, XRD and FESEM-EDX analyses); (iii) the rate of temperature rise tends to intensify as the H increases to 35 kA/m, this implies that SAR of the samples could also

rise since it jointly varies with rate change of temperature, as shown in equation 23; and (iv) physiological temperature ranges between 36 to 37 ^{o}C (Prasad et al., 2013). It follows that a minimum of 5 – 6 ^{o}C and a maximum of 9 – 10 ^{o}C temperature rise is required to achieve the hyperthermia temperature (42 – 46 ^{o}C). For example, at 15 kA/m (the lowest heating magnetic field strength), the functionalized and grafted samples (i.e., FAP C, MHNS C, MHNS D and MHNS E) could reach this target temperature. However, for optimal performance during MHT, reaching the MHT temperature timely is paramount; it improves the heating efficiency, reduces the dosage and exposure time, and eases patient discomfort. As shown in Figure 4.9 (j), the time required to reach MHT temperature (t_{MHT}) tends to rise as the functionalization of bare FeNPs progresses (i.e., 240 and 480 s for FeNPs and FAP C at 15 kA/m, respectively). However, upon successfully grafting the functionalized bare FeNPs (FAP C) onto GO nanoplatform, the time declines. It takes FAP C and MHNS E 480 and 330 s to reach the t_{MHT}, respectively. These make MHNS E the best among all the modified samples in this regard. In a nutshell, GO nanoplatform as support for functionalized FeNPs improves the heating time, which could translate to heating efficiency; however, this can only be confirmed by quantifying the corresponding SAR.

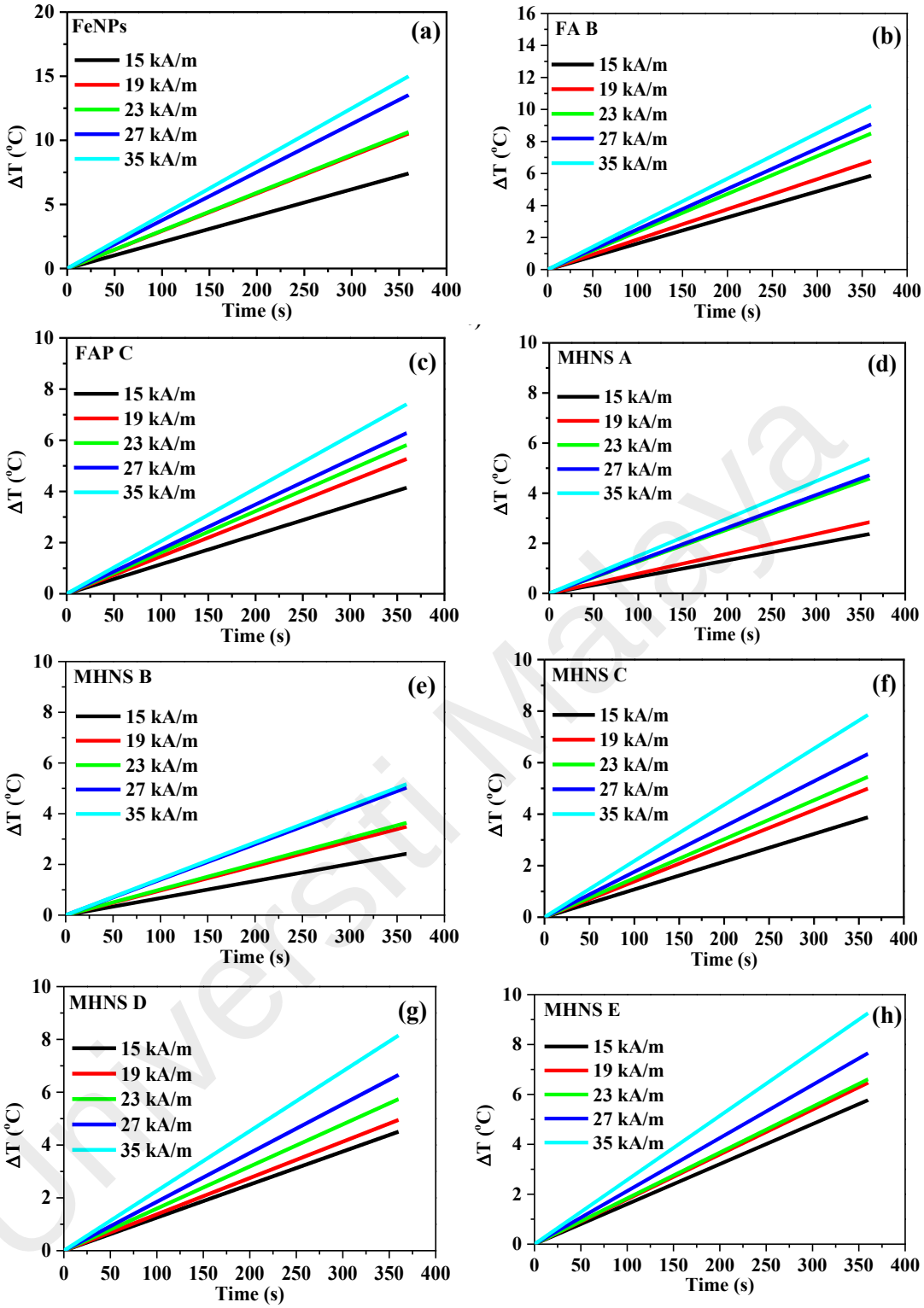

Figure 4.9: Heating curves at five different magnetic field strength (15 – 35 kA/m) for FeNPs (a), APTES modified FeNPs denoted as FA B (b), PEG functionalized FA B denoted as FAP C (c), FAP C grafted onto GO nanoplatform at various GO:FAP C loading; 1:1, 1:0.5, 1:2, 1:3 and 1:4 denoted as MHNS A, MHNS B, MHNS C, MHNS D and MHNS E respectively (d - h), plain GO nanoparticles (i) and time taken to reach hyperthermia temperature at 316 kHz and 15 kA/m (j).

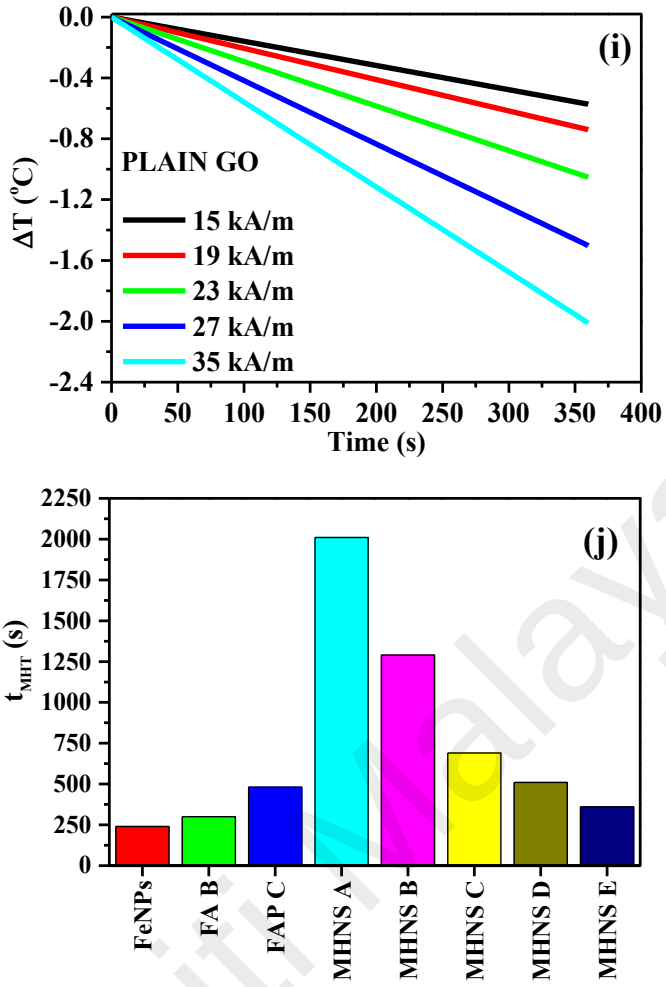

Figure 4.9, continued

4.3.2.2 optimum specific absorption rate (SAR)

Figure 4.10, 4.11 and Appendix E presents the SAR of bare FeNPs, FA B, PEGylated FeNPs (FAP C) and FAP C grafted onto GO nanoplatform at various GO:FAP C loading (1:1, 1:0.5, 1:2, 1:3 and 1:4 denoted as MHNS A, MHNS B, MHNS C, MHNS D and MHNS E respectively; where MHNS A is the control) quantified at five different *H*. Observing Figure 4.10 a, as the surface of the bare FeNPs is being modified, the SAR drops linearly (at average 19 and 40 % drop, respectively) because of the changes in magnetic and physicochemical properties as previously observed by the XRD, FTIR, FESEM-EDX and VSM analyses. This affirmed the aforementioned MHT major challenge (drop-in FeNPs SAR when functionalized). The aim of this study is to improve the SAR. Interestingly, upon grafting the modified FeNPs (FAP C with size < 12 nm)

onto GO nanoplatform, the SAR rises (Figure 4.10 b); taking heating at 15 kA/m for example, comparing the SARs of bare FeNPs (57 W/g), FA B (49 W/g) and FAP C (36 W/g) to MHNS E (60 W/g), the bare FeNPs heating ability has clearly been restored. The heating enhancement indicates that grafting ensures clustering of functionalized FeNPs onto GO nanoplatform and improves the interparticle dipolar interactions. Literature suggests that clustered FeNPs (less than 26 nm) and strong interparticle interaction buttress heating under the influence of ACMF (Dennis et al., 2009; Fu, Yan, Roberts, Liu, & Chen, 2018; Halilu et al., 2020; Jadhav et al., 2019; X. Liu et al., 2019; Pearce, Giustini, Stigliano, & Jack Hoopes, 2013; Rasheed et al., 2020).

As observed with M_S earlier (Figure 4.1), varying the loading of FAP C onto GO nanoplatform also reflects on the SAR. Besides the control (MHNS A) at $H < 19$ kA/m, the SARs of the MHNSs are higher than FAP C at all Hs (15 – 35 kA/m). The sudden rise of MHNS A and MHNS B SARs at higher Hs shows that higher H favors GO attributes. Although the rise in SAR is not directly proportional to M_S, these patterns (in Figure 4.10 b) are similar to the optimization patterns obtained from VSM magnetic studies (Figure 4.1). The divergence is that: (i) MHNS B which has lower M_S, has higher SAR compared to the control (MHNS A), and (ii) MHNS E, which also has lower M_S, has higher SAR compared to FAP C. The peculiarity of the MHNSs is the presence of GO nanoplatform as support which translates to a higher heating surface. This shows that, besides high M_S, clustering FeNPs also improves heating ability.

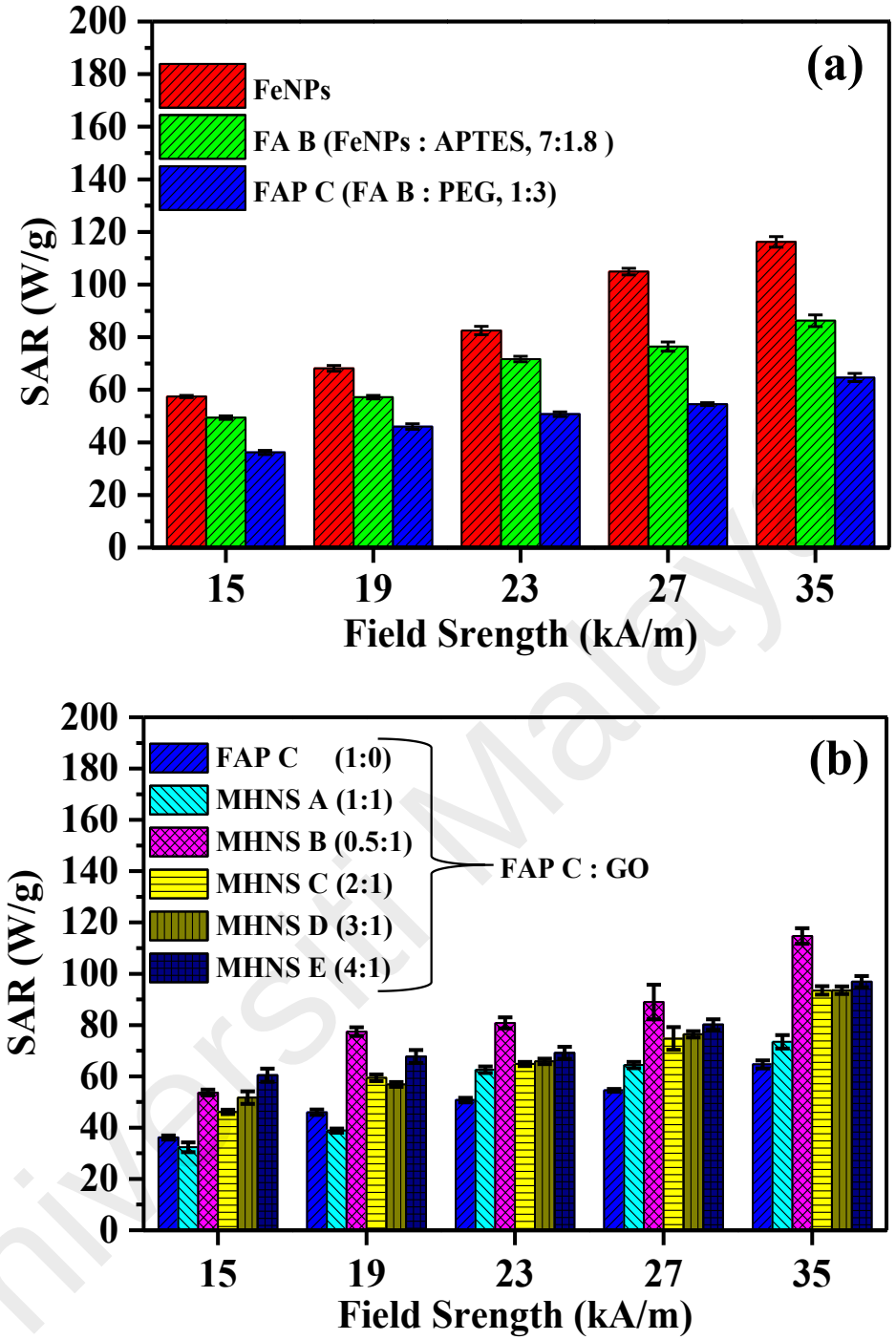

Figure 4.10: SAR quantified at five different *H* for bare FeNPs, FA B, FAP C (a) and MHNS A, MHNS B, MHNS C, MHNS D and MHNS E (b). SAR dropped upon functionalizing the surface of bare FeNPs. It was restored after grafting the functionalized FeNPs onto GO nanoplatform.

Still on, besides the dependence of SAR on sample composition, evidence from Figure 4.10 also shows that the magnitude of SAR depends on *H*; for example, as the magnitude of *H* increases from 15 to 35 kA/m, the SARs also increase. This observation is in line with the preliminary studies and other published reports (Ganesan et al., 2019; Yu et al.,

2020). Admittedly, due to this dependence, it will be quite difficult to directly compare SARs of different or even the same MHNS measured at different heating parameters (*H* and *f)*. Hence, a variable called intrinsic loss power (ILP; equation 24) is suggested for normalizing SAR obtained at different heating parameters (Chang et al., 2018). Hence, the optimum sample and heating parameters can be defined. In essence, SAR quantifies heating capabilities while ILP divulges the optimum by relating the heating parameters and SAR.

Figure 4.11 and Appendix E presents the SAR and ILP estimated (for all samples used in Figure 4.10) at all heating parameters. Take, for example, heating at 15 and 35 kA/m (i.e., minimum and maximum *H*); within the same *H*, both SAR and ILP vary in the same manner (Figure 4.11 a and b). On the contrary, as *H* increases, SAR rises while ILP drops (Figure 4.11 a and b). A similar observation is seen with 19, 23 and 27 kA/m (Appendix E). Therefore, given the above, MHNS E and 15 kA/m are the optimum.

There is no limit of confinement for heating parameters to be applied during induction heating because they vary depending on the type of equipment or properties of coils used; however, considering the safety and threshold of factors such as eddy current side effects as mentioned earlier, the product of *Hf* applied should not exceed $5 \times 10^9\ Am^{-1}s^{-1}$ according to Rudolf Hergt and Dutz (2007) criterion. Accordingly, to quantify heating capabilities relative to the *Hf* safety limit, herein, α (equation 25) was used. Figure 4.11 c summarizes all the α estimated. At *Hf* < safety, MHNS E (61.28 W/g) retained its optimal position, whereas on the other hand, considering *Hf* > safety, MHNS B has higher α (65.37 W/g). Nevertheless, it is clear that, at all heating parameters, MHNS dispenses efficient thermal energy compared to modified FAP C (and even the bare FeNPs in most cases). Table 4.3 compares the performance of some MHT materials in this work (FeNPs,

FA B, FAP C and MHNS E) with the literature; it is evident that the MHT materials reported in this work are outstanding.

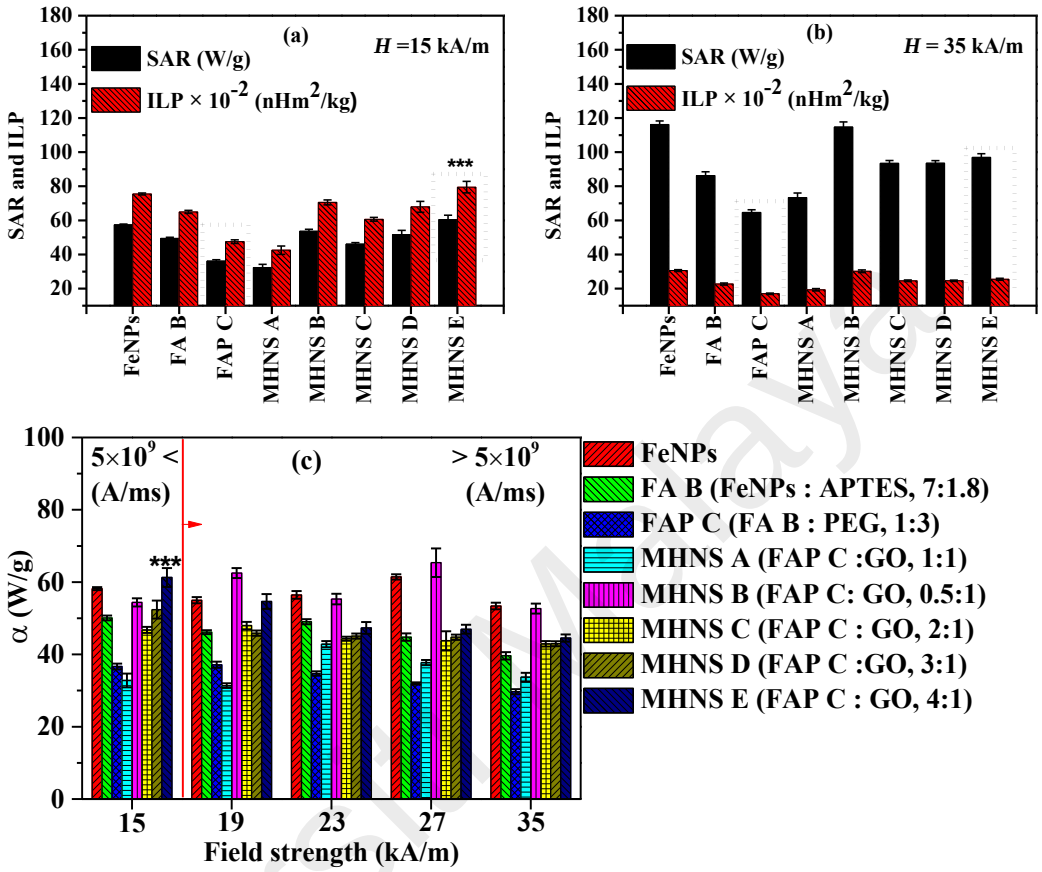

Figure 4.11: Relationship between SAR and ILP at 15 kA/m (a) and 35 kA/m (b). Comparison of SAR relative to *Hf* safety limit at 15 kA/m (c).

Table 4.3: Comparing the performance of some MHT materials in this work with literature. The ***** stands for heating curve duration.

Materials	ILP (nHm^2 /kg)	SAR (W/g)	H x f (A/ms)	α (W/g)	Time* (s)	Reference
FeNPs	0.7549	57.44	4.93×10^9	58.27	360	This work
FA B	0.6497	49.43	4.93×10^9	50.09	360	This work
FAP C	0.4766	36.17	4.93×10^9	36.70	360	This work
MHNS E	0.8399	60.47	4.93×10^9	61.28	360	This work
MNPs-sugar alcohol	0.2103	103.2	1.21×10^{10}	42.53	900	(Gawali, Barick, Barick, & Hassan, 2017)
FeNPs	0.2141	20.00	5.77×10^9	17.34	30	(Bielas et al., 2020)
FeNPs-TMAOH	0.2220	111.0	7.94×10^9	69.92	-	(Lahiri, Ranoo, & Philip, 2017)
$Zn_{0.54}Co_{0.46}Cr_{0.6}Fe_{1.4}O_4$	0.2300	23.24	3.20×10^9	36.32	-	(Yu et al. 2020)
$Li_{0.3}Zn_{0.3}Co_{0.1}Fe_{2.3}O_4$	0.2477	83.00	1.00×10^{10}	41.39	600	(Dalal et al., 2017)
$Li_{0.3}Zn_{0.3}Co_{0.1}Fe_{2.3}O_4$-MWCNT	0.0925	31.00	1.00×10^{10}	15.46	600	(Dalal et al., 2017)
FeNPs	0.2759	34.71	3.98×10^9	43.59	72/60	(Ganesan et al., 2019)
FeNPs	0.2898	118.0	1.13×10^{10}	52.01	600	(Rajan, Sharma, & Sahu, 2020)
FeNPs-aminosilane	0.3648	29.00	4.91×10^9	29.00	300	(Rego et al., 2019)
FeNPs-PEG	0.3873	190.0	1.21×10^{10}	78.31	360	(Dutta et al., 2018)
FeNPs	0.4271	18.50	2.28×10^9	40.57	700	(Fotukian, Barati, Soleymani, & Alizadeh, 2020)
$Co_{0.3}Fe_{0.7}C$	0.4700	46.00	4.79×10^9	49.07	2700	(Gangwar et al., 2019)
γ-Fe_2O_3-SiO_2-CaO	0.5145	159.0	1.29×10^{10}	61.74	180	(Kesse et al., 2020)
Fe_3C	0.5500	53.00	4.79×10^9	55.33	2700	(Gangwar et al., 2019)
$CoFe_2O_4$	0.5784	248.0	1.23×10^{10}	101.2	480	(Kharat, Somvanshi, Khirade, & Jadhav, 2020)
MNP-DA	0.5867	124.0	1.06×10^{10}	58.58	300	(Cervantes et al., 2020)

4.3.2.3 effect of concentration, heating medium, and background warming on SAR

There have been contradicting reports on effect of FeNPs concentration on SAR. Some studies reported SAR increasing with concentration (Andrés Vergés et al., 2008; Piñeiro-Redondo et al., 2011; Rajan S & Sahu, 2020; Salas, Veintemillas-Verdaguer, & Morales, 2013; Sánchez, Rodríguez-Reyes, Cortés-Hernández, Ávila-Orta, & Reyes-Rodríguez, 2021) while others reported inverse variation (Gawali et al., 2017; Ranoo, Lahiri, Vinod, & Philip, 2019; Skumiel et al., 2020) or constant relationship (de la Presa et al., 2012).

The perception of SAR-concentration dependence has generally been studied from an interparticle interactions point of view (Deatsch & Evans, 2014; Dennis et al., 2009; Ranoo et al., 2019); as the concentration increases, these interparticle interactions also intensify and thus alter the NPs response to ACMF which directly affects the relaxations time (Néel and Brownian relaxations) and reflects on the SAR. While various contradicting models have been proposed to describe this SAR-concentration dependence from the aforementioned viewpoint, interestingly, this study was able to point out the possible root cause from a different perspective.

In most magnetic field-induced heating studies reviewed, the impact of heating medium and background warming are often overlooked (Dabbagh et al., 2019; Nikitin et al., 2019; Rego et al., 2019); SAR is computed directly from raw data set instead of normalizing with the blank solvent (i.e., plain solvent without any hyperthermia material). This results in erroneous SAR measurement and evaluation. Figure 4.12 (a) presents the performance of FeNPs at concentrations ranging between 0.2 – 20 mg/mL estimated from both raw and normalized data sets at 15 kA/m. As shown therein: (i) at lower concentrations (< 1 mg/mL), SAR decreases with a rise in concentration when estimated from the raw data set, whereas it increases when estimated from the normalized data set. This perturbation was further affirmed using MHNS at 15 and 35 kA/m (Figure 4.12 b

and c, respectively); (ii) above 1.5 mg/mL, the pattern is similar for both data sets; (iii) the peak SAR is at 2 mg/mL; (iv) beyond 2 mg/ml, SARs for all data sets decreases with rising concentration and converge at 15 mg/mL; (v) it roughly remains constant after that; and (vi) the impact of heating medium and background warming are highly significant at lower concentration (< 1.5 mg/mL). In practice, a lower concentration is preferential for MHT (Albarqi et al., 2019). However, efficient MHT (i.e., higher SAR) has often been viewed achievable at higher concentrations; interestingly, with the above points, it was shown achievable at lower concentrations (≤ 2 mg/mL). Therefore, appropriate SAR estimation is indeed important.

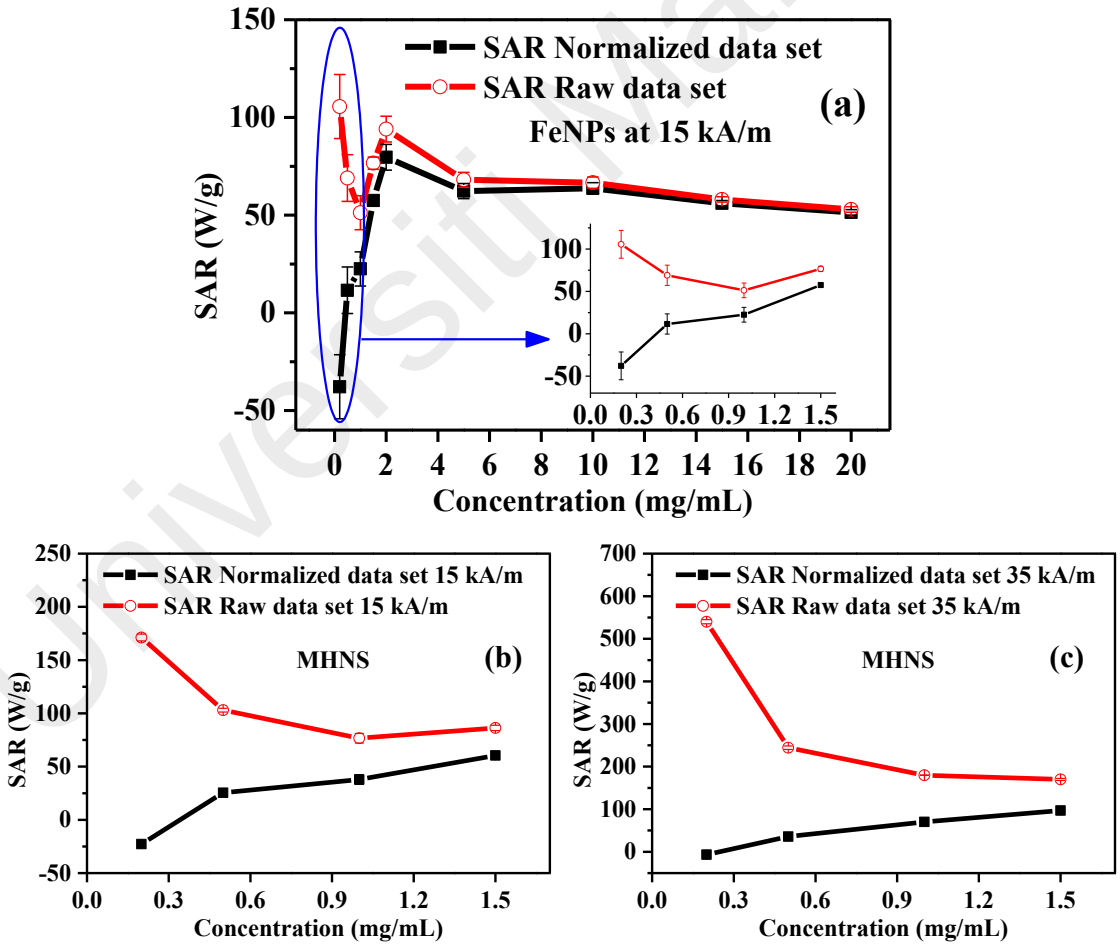

Figure 4.12: SAR-concentration dependence for FeNPs at 15 kA/m (a) and MHNS at 15 and 35 kA/m (b and c).

In a nutshell, these variations highlighted in Figure 4.12 could be explained by observing Figure 4.13. As shown therein, higher heating curves were obtained from raw data sets, and their associated rate change of temperature (as the concentration approach 1.5 mg/mL) is relatively higher compared to the normalized data sets. Since SAR, rate change of temperature, and mass fraction of FeNPs in the heating medium (which extends to the concentration) have a combined variation relating them, the SAR estimated from the normalized data set should have a rising pattern as observed.

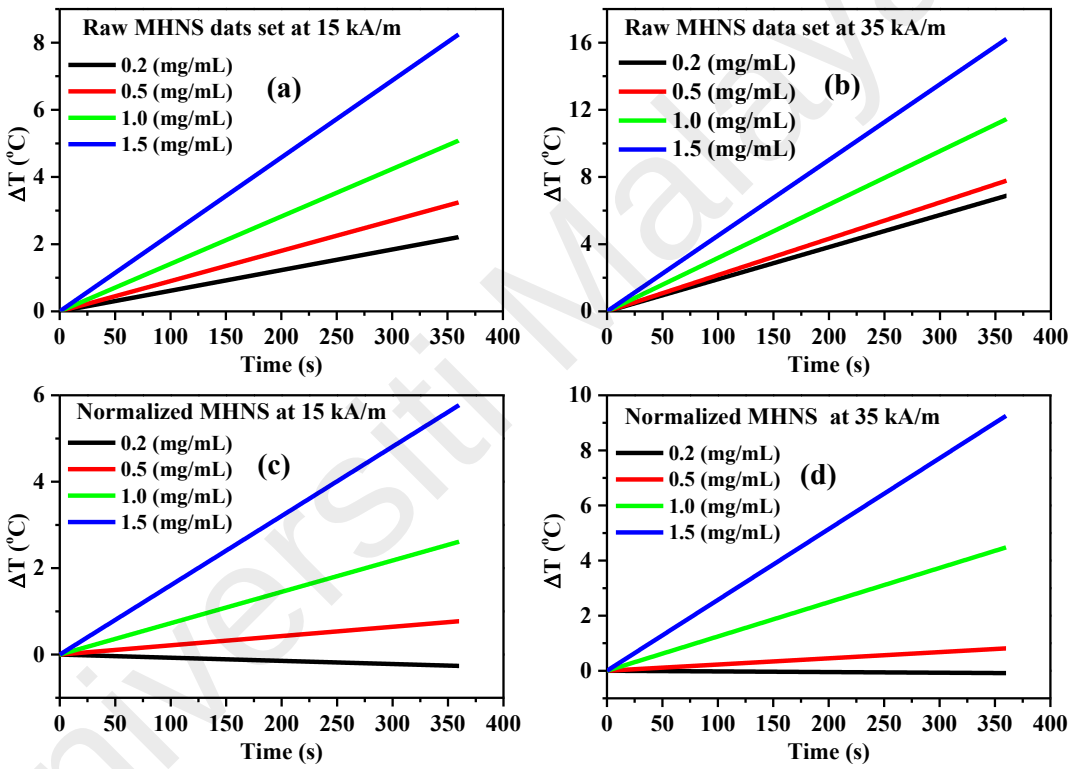

Figure 4.13: Heating curves for the effect of concentration, heating medium, and background warming on MHNS. Measurements were done at 15 and 35 kA/m for both raw and normalized data set. For bare FeNPs, see Appendix E.

In essence, SAR of MHT material is accurately estimated from a normalized data set (data set without the impact of the heating medium and background warming). In such estimation, it rises with the concentration and reaches its peak at 2 mg/mL before slightly dropping and remains roughly constant afterward (even up to 20 mg/mL). Thus, observing the rising, decreasing and constant SAR-concentration patterns herein (which

are the contradicting patterns reported in the literature) buttresses the above explanations. Since there is limited consensus on the role of interparticle interaction on SAR-concentration dependence, as a suggestion for further experimental studies, probing these interactions using normalized data sets is therefore of particular importance.

4.3.2.4 effect of pH on SAR

A tumor microenvironment is more acidic than a healthy cell microenvironment (tumor acidosis) due to its peculiar metabolism (Gerweck & Seetharaman, 1996; Rodrigues et al., 2018); the Warburg effect and poor waste clearance (Gatenby & Gillies, 2004; Onyango et al., 2015). Moreover, when an MHT material is deposited within the cancer cells matrix, an endosome/lysosome is formed, the pH of such vicinity becomes more acidic than the tumor microenvironment (J. Liu et al., 2016). The pH of normal tissue (healthy cells), tumor microenvironment, and intracellular tumor endosome/lysosome ranges between 7.20 – 7.50, 6.50 – 6.98, and 4.50 – 5.50, respectively (Gao et al., 2012; J. Liu et al., 2016). Estimating the effect of pH on SAR (SAR-pH dependence) has been a gap in the literature. Therefore, a magnetic field-induced study was carried out herein at four different pH scales, ca. 4, 5, 7, and 9 (4 and 9 as the control boundaries), to fill up the gap and, thus, mimic the heating at different cellular environments.

The outcome of the SAR-pH dependence measurement is shown in Figure 4.14. Although the heating curve of all the plain solvents (heating media) remained roughly the same (Figure 4.14 d), interestingly, Figure 4.14 a – c shows SAR-pH dependence which could be attributed to the behavior of the magnetic NPs under the influence of magnetic flux: at the desired intracellular endosome/lysosome pH, the SAR of MHNS was the highest, 60 W/g, it continued dropping at a faster rate compared to FeNPs as the normal tissue pH was approached and was least at the extreme basic boundary (2-fold lesser than

intracellular endosome/lysosome pH region). These imply that thermal energy dispensed at the healthy cell environment (pH > 6.98) is lower compared to the cancer cells environment (4.5 ≤ pH ≤ 6.98) and thus ensures the required thermal sensitization instead of thermal ablation. In a nutshell, this smart self-control attribute points out the potentials of the proposed MHNS, especially at the target environmental conditions. The SAR-pH dependence established herein is the first of its kind and can be furthermore harnessed in pH-responsive applications such as thermo-chemotherapy (Işıklan et al., 2021; Rodrigues et al., 2018; Saepudin, Fadhilah, & Khalil, 2020).

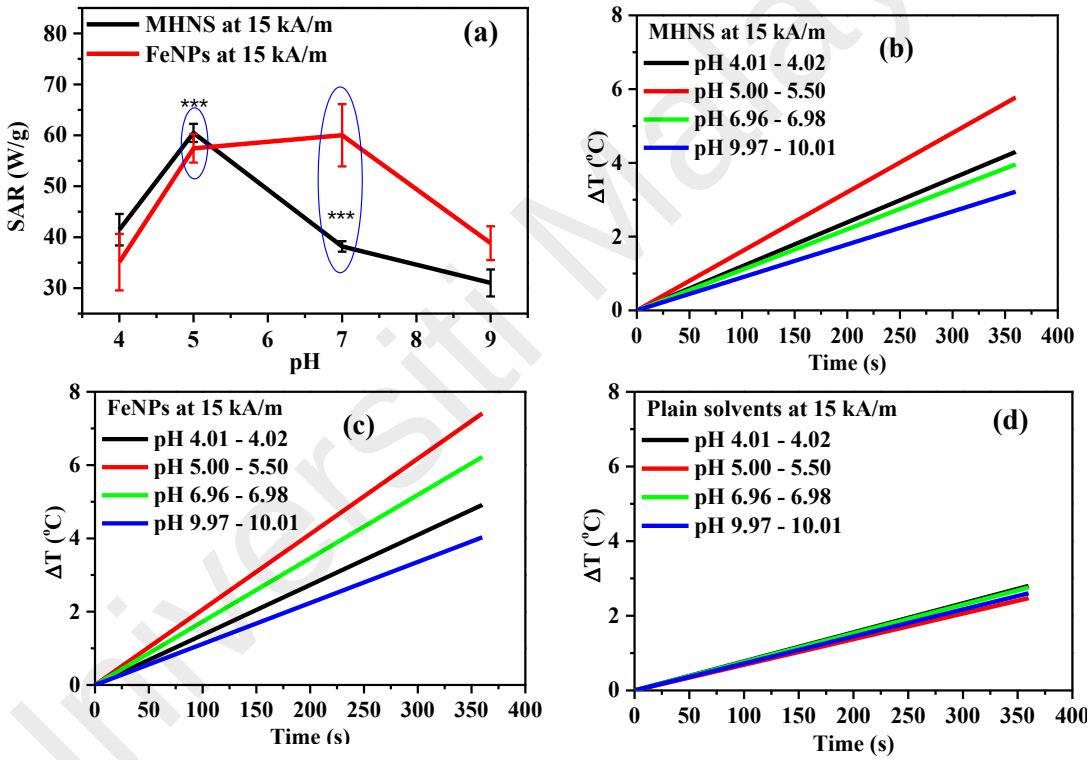

Figure 4.14: (a) FeNPs and MHNS SAR-pH dependence. (b – d) The heating curves for the effect of pH on MHNS, FeNPs and plain heating media (i.e., without any MHT material).

4.3.2.5 effect of heating medium viscosity on SAR

Brown relaxation, Néel relaxation, hysteresis loss and eddy current are generally the different heating mechanisms for NPs absorbing radio-frequency power (Deatsch & Evans, 2014; Moroz et al., 2002; Prasad et al., 2013; Rosensweig, 2002). The last two are impactful at centimeter or larger scale and for non-superparamagnetic materials, making

them insignificant for the MHT materials synthesized herein (they are all superparamagnetic and < 13 nm). Néel relaxation (internal rotation of the magnetic moment between 0 – 180^{o}) and Brownian relaxation (rotational friction of the particles within a heating medium) could co-occur and either may perhaps dominate at different size scales (Fortin et al., 2007). The former is peculiar to the superparamagnetic regime, while the latter could exceed 250 nm (Ganesan et al., 2019).

Varying the viscosity of the heating medium is a significant parameter relevant to Brownian relaxation; as the viscosity rises, Brownian motion is hindered, resulting in a significant drop in SAR if the heating mechanism is dominated by the Brownian mechanism (Liang et al., 2017). Herein, the influence of heating medium viscosity (distilled water was used as the heating medium, and a desired amount of glycerol was added to control its viscosity) on SAR is presented in Figure 4.15. It could be seen that MHNS SAR only drops with an intense rise in viscosity (760-fold) and remains roughly constant at lower viscosities ($\eta < 34$ mPa.s), an indication that the heating mechanism for MHNS is dominated by Néel relaxation. Similar dominance has been reported for some NPs within the size range reported herein (Fortin et al., 2007; Liang et al., 2017). Nevertheless, the Brownian contribution is not totally ruled out.

The general implication of these results is that the MHNS can perform in body fluids (e.g., blood, lymph and Cerebro Spinal Fluid: $\eta < 6$ mPa.s), agar-based tissue-mimicking phantoms ($\eta < 100$ mPa.), and in complex media including cell lines wherein the restriction of particle orientation (viscosity) which translates to rotational friction of the particles (Brownian motion) rises substantially (Baskurt & Meiselman, 2003; Bloomfield, Johnston, & Bilston, 1998; Bouta et al., 2014; Molcan et al., 2020; Rother, Nöding, Mey, & Janshoff, 2014; Zupančič Valant, Žiberna, Papaharilaou, Anayiotos, & Georgiou, 2011).

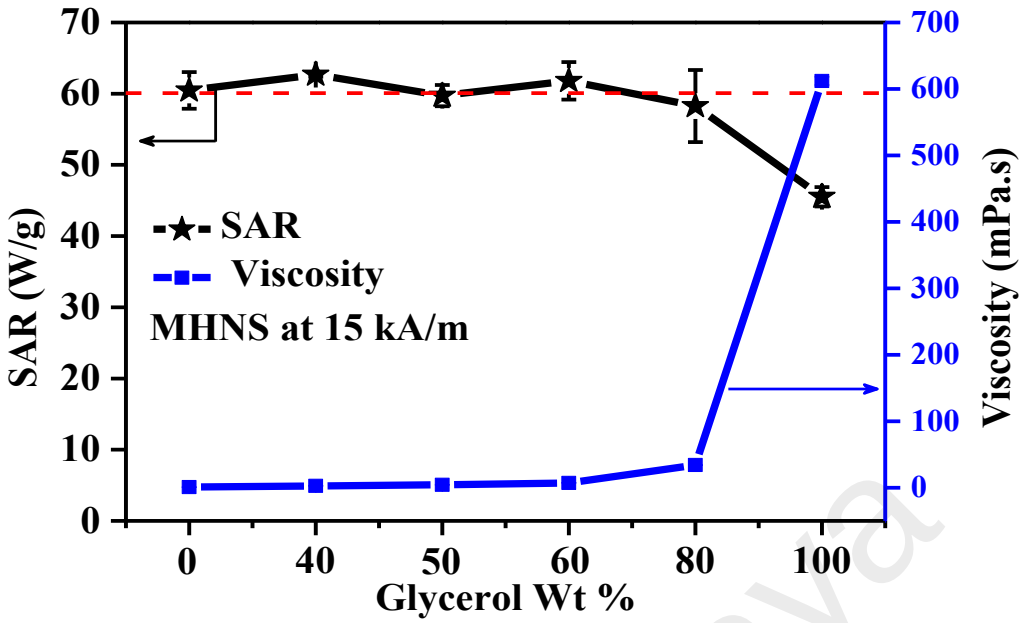

Figure 4.15: The influence of heating medium viscosity on SAR. The viscosity of the heating medium was varied between 0.8 to 600 mPa.s by adding different Wt% of glycerol. This ensures colloidal stability, unlike using sol-gel transition.

CHAPTER 5: CONCLUSIONS AND FUTURE WORK

5.1 Conclusions

This study is devoted to improving the heating ability of functionalized Fe_3O_4 nanoparticles (FeNPs) by developing a new magnetic hybrid nanostructure (MHNS) which is superparamagnetic and could generate heat under the influence of Alternating Current Magnetic Field (ACMF). Such heat will raise the temperature of its immediate vicinity and within a range, 5 – 10 ^oC above physiological temperature (37 ^oC), the retained thermal energy can selectively destroy cancer cells by exploring their susceptibility to heat; this is the basic concept of magnetic hyperthermia therapy (MHT), a very promising modality for treating various cancers and malignant tumors.

The desired MHNS has been successfully synthesized. It is mainly composed of FeNPs, Polyethylene glycol (PEG) and Graphene oxide (GO). Accordingly, a facile four-step *ex-situ* approach was trailed in fabricating the MHNS: (i) Synthesizing bare FeNPs (ii) silanization of the bare FeNPs with APTES denoted as FA (iii) functionalizing the FA with PEG denoted as FAP (iv) and finally grafting the FAP onto GO nanoplatform denoted as MHNS. Natural atmospheric conditions were maintained in these stagewise syntheses. The approach allows logical modifications and optimization by systematically varying FeNPs, APTES, PEG and GO loading to obtain products with different compositions. The GO functions as a nanoplatform to support clustering the functionalized FeNPs and coupled with the PEG (which was facilitated by APTES), improved heating ability and MHT applicability could be ensured. The embedded FeNPs is primarily responsible for the magnetic behavior; as a result of Néel and Brown relaxations, it acts as a heat dispenser under the influence of radiofrequency power created by ACMF generator.

Various analytical techniques such as VSM, XRD, FTIR and FESEM-EDX were used to study morphology, chemical, physical and magnetic behavior of the stagewise products obtained. Some observations noticed from these techniques, and the magnetic field-induced heating measurements include:

(1) The FESEM image of FeNPs, FA, FAP, and MHNS showed similar morphologies that indicate a single-phase structure formation. More so, the detection of Fe, N, Si, C and O elements by EDX as the stagewise syntheses progress (which also correlates with the FTIR spectra and the XRD pattern) indicates the formation of purely FeNPs-APTES-PEG-GO magnetic hybrid nanostructure (MHNS).

(2) Varying FeNPs, FA, FAP and MHNS loading reflected on the magnetic properties and was exploited in fine-tuning the stagewise syntheses; precisely, the M_S decreases. The patterns are different at all stages; two opposite curvilinear patterns appeared during the functionalization (modifications with APTES and PEG, respectively), whereas a linear pattern was observed during grafting. On average, M_S values of 68.36 emu/g, 64.67 emu/g, 60.89 emu/g and 40.76 emu/g were recorded for FeNPs, FA, FAP and MHNS, respectively. These affirm successful functionalization and grafting.

(3) All the VSM hysteresis loops overlapped completely and followed a sigmoidal pattern (S-shape). These confirm that the fabricated MHT materials are superparamagnetic.

(4) The sizes of FeNPs, FA, FAP and MHNS were found to be ca. 9.24, 10.37, 11.97 and 12.25 nm, respectively. These sizes are much less than the critical size (~26 nm); therefore, they are within the safe limit to exhibit superparamagnetic behavior observed from the VSM measurement. Furthermore, the increase in size shows incorporation of other particles and implies that FeNPs are embedded in three layers which favors MHT.

(5) The heating capacity of the synthesized MHT materials quantified by SAR was found to depend on FeNPs concentration, MHNS composition, magnetic field strength *H*, background warming, the type of heating media used and its viscosity. More so, for the first time, it was shown to depend on the microenvironment pH. To improve the amount of thermal energy dispensed by the MHT materials, this study modulates these factors. Accordingly, it can be deduced that: (i) The impacts of heating medium and background warming were a possible root cause of contradicting reports on the effect of sample concentration on SAR. These impacts are highly significant especially at lower concentration (< 1.5 mg/mL); (ii) SAR is accurately estimated from normalized data set (data set without the impact of the heating medium and background warming); (iii) SAR increases with sample concentration and reach peak value at around 2mg/mL before dropping; (iv) SAR also drops upon functionalizing bare FeNPs with surfactants; (v) Grafting functionalized FeNPs (FAP C) onto GO nanoplatform at 4:1 loading to form MHNS improves heating efficiency (SAR at 4:1 > 0.5:1 > 3:1 > 2:1 > 1:1 at optimum heating parameters) and dispensed 2-fold heat at simulated tumor microenvironment pH (4.5 - 6.98) compared to healthy cells microenvironment pH (> 7); (vi) The optimum heating parameters are f = 316 kHz, H = 15 kA/m and 360 s; (vii) Besides its optimal heating ability, MHNS E also has a smart self-control attribute considering its maximum temperature rise reached (10 ^{o}C) and pH-sensitivity which could only lead to the required thermal sensitization; (viii) Lastly, SAR of MHNS only drops slightly with an intense rise in heating medium viscosity (760-fold), indicating that Néel relaxation dominates the heating mechanism.

These observations suggest that the MHNS can perform in complex media. Thus, this new nanostructured MHT material offers enhanced heating efficiency, a prerequisite for

stable performance in MHT. In a nutshell, this study provides a new opportunity for developing functional MHNS for cancer therapy at the cellular level.

5.2 Future Work

The FeNPs embedded in MHNS has been reported to have photo effects that could be exploited in heat generation. In this regard, could ACMF and NIR provide synergistic effects? We will appreciate collaboration to explore this and take the work to *in vivo* stage and beyond. On a similar note, besides magnetic hyperthermia therapy, the MHNS synthesized in this work has other prospective applications such as drug delivery vehicle, MRI contrast agent, water treatment, membrane separation, anti-wear additive and heat transfer fluids in heat exchangers; it will be worthwhile to explore them.

REFERENCES

Ahn, T., Kim, J. H., Yang, H.-M., Lee, J. W., & Kim, J.-D. (2012). Formation Pathways of Magnetite Nanoparticles by Coprecipitation Method. *The Journal of Physical Chemistry C, 116*(10), 6069-6076. doi:https://doi.org/10.1021/jp211843g

Aksu Demirezen, D., Yıldız, Y. Ş., Yılmaz, Ş., & Demirezen Yılmaz, D. (2019). Green synthesis and characterization of iron oxide nanoparticles using Ficus carica (common fig) dried fruit extract. *Journal of Bioscience and Bioengineering, 127*(2), 241-245. doi:https://doi.org/10.1016/j.jbiosc.2018.07.024

Alam, S. N., Sharma, N., & Kumar, L. (2017). Synthesis of graphene oxide (GO) by modified hummers method and its thermal reduction to obtain reduced graphene oxide (rGO). *Graphene, 6*(01), 1-18. doi:10.4236/graphene.2017.61001

Alazmi, A., Rasul, S., Patole, S. P., & Costa, P. M. F. J. (2016). Comparative study of synthesis and reduction methods for graphene oxide. *Polyhedron, 116*, 153-161. doi:https://doi.org/10.1016/j.poly.2016.04.044

Albarqi, H. A., Wong, L. H., Schumann, C., Sabei, F. Y., Korzun, T., Li, X., . . . Taratula, O. (2019). Biocompatible nanoclusters with high heating efficiency for systemically delivered magnetic hyperthermia. *ACS nano, 13*(6), 6383-6395. doi:10.1021/acsnano.8b06542

Albert, E. L., Abdullah, C. A. C., & Shiroshaki, Y. (2018). Synthesis and characterization of graphene oxide functionalized with magnetic nanoparticle via simple emulsion method. *Results in Physics, 11*, 944-950. doi:https://doi.org/10.1016/j.rinp.2018.10.054

Alegret, N., Criado, A., & Prato, M. (2017). Recent advances of graphene-based hybrids with magnetic nanoparticles for biomedical applications. *Current medicinal chemistry, 24*(5), 529-536. doi:10.2174/0929867323666161216144218

Ali, A., Zafar, H., Zia, M., Ul Haq, I., Phull, A. R., Ali, J. S., & Hussain, A. (2016). Synthesis, characterization, applications, and challenges of iron oxide nanoparticles. *Nanotechnology, science and applications, 9*, 49-67. doi:10.2147/NSA.S99986

Altaf, F., Niazi, M. B. K., Jahan, Z., Ahmad, T., Akram, M. A., Safdar, A., . . . Sher, F. (2021). Synthesis and characterization of PVA/starch hydrogel membranes incorporating essential oils aimed to be used in wound dressing applications. *Journal of Polymers and the Environment, 29*(1), 156-174. doi:10.1007/s10924-020-01866-w

Amani, A., Begdelo, J. M., Yaghoubi, H., & Motallebinia, S. (2019). Multifunctional magnetic nanoparticles for controlled release of anticancer drug, breast cancer cell targeting, MRI/fluorescence imaging, and anticancer drug delivery. *Journal of Drug Delivery Science and Technology, 49*, 534-546. doi:https://doi.org/10.1016/j.jddst.2018.12.034

Amendola, V., & Meneghetti, M. (2013). What controls the composition and the structure of nanomaterials generated by laser ablation in liquid solution? *Physical Chemistry Chemical Physics, 15*(9), 3027-3046. doi:https://doi.org/10.1039/C2CP42895D

Amir, M. N. I., Halilu, A., Julkapli, N. M., & Ma'Amor, A. (2020). Gold-graphene oxide nanohybrids: A review on their chemical catalysis. *J Ind Eng Chem, 83*, 1-13. doi:10.1016/j.jiec.2019.11.029

Anbarasu, M., Anandan, M., Chinnasamy, E., Gopinath, V., & Balamurugan, K. (2015). Synthesis and characterization of polyethylene glycol (PEG) coated Fe_3O_4 nanoparticles by chemical co-precipitation method for biomedical applications. *Spectrochimica Acta Part A: Molecular and Biomolecular Spectroscopy, 135*, 536-539. doi:https://doi.org/10.1016/j.saa.2014.07.059

Andrés Vergés, M., Costo, R., Roca, A. G., Marco, J. F., Goya, G. F., Serna, C. J., & Morales, M. P. (2008). Uniform and water stable magnetite nanoparticles with diameters around the monodomain–multidomain limit. *Journal of Physics D: Applied Physics, 41*(13), 134003. doi:10.1088/0022-3727/41/13/134003

Anin Vincely, D., & Natarajan, E. (2016). Experimental investigation of the solar FPC performance using graphene oxide nanofluid under forced circulation. *Energy Conversion and Management, 117*, 1-11. doi:https://doi.org/10.1016/j.enconman.2016.03.015

Arias, L., Pessan, J., Vieira, A., Lima, T., Delbem, A., & Monteiro, D. (2018). Iron oxide nanoparticles for biomedical applications: A perspective on synthesis, drugs, antimicrobial activity, and toxicity. *Antibiotics, 7*(2), 46. doi:https://doi.org/10.3390/antibiotics7020046

Arsalani, S., Guidelli, E. J., Silveira, M. A., Salmon, C. E., Araujo, J. F., Bruno, A. C., & Baffa, O. (2019). Magnetic Fe3O4 nanoparticles coated by natural rubber latex as MRI contrast agent. *Journal of Magnetism and Magnetic Materials, 475*, 458-464. doi:https://doi.org/10.1016/j.jmmm.2018.11.132

Bai, S., & Shen, X. (2012). Graphene–inorganic nanocomposites. *Rsc Advances, 2*(1), 64-98. doi:10.1039/C1RA00260K

Bandi, S., Ravuri, S., Peshwe, D. R., & Srivastav, A. K. (2019). Graphene from discharged dry cell battery electrodes. *Journal of hazardous materials, 366*, 358-369. doi:https://doi.org/10.1016/j.jhazmat.2018.12.005

Barrera, G., Coisson, M., Celegato, F., Martino, L., Tiwari, P., Verma, R., . . . Tiberto, P. (2020). Specific Loss Power of Co/Li/Zn-Mixed Ferrite Powders for Magnetic Hyperthermia. *Sensors, 20*(7), 2151. doi:10.3390/s20072151

Baskurt, O. K., & Meiselman, H. J. (2003). Blood rheology and hemodynamics. *Semin Thromb Hemost, 29*(5), 435-450. doi:10.1055/s-2003-44551

Beik, J., Abed, Z., Ghoreishi, F. S., Hosseini-Nami, S., Mehrzadi, S., Shakeri-Zadeh, A., & Kamrava, S. K. (2016). Nanotechnology in hyperthermia cancer therapy: From

fundamental principles to advanced applications. *Journal of Controlled Release, 235*, 205-221.

Bennett, J. E., Stevens, G. A., Mathers, C. D., Bonita, R., Rehm, J., Kruk, M. E., . . . Ezzati, M. (2018). NCD Countdown 2030: worldwide trends in non-communicable disease mortality and progress towards Sustainable Development Goal target 3.4. *The Lancet, 392*(10152), 1072-1088. doi:10.1016/s0140-6736(18)31992-5

Beola, L., Gutiérrez, L., Grazú, V., & Asín, L. (2019). A roadmap to the standardization of in vivo magnetic hyperthermia. In R. M. Fratila & J. M. De La Fuente (Eds.), *Nanomaterials for magnetic and optical hyperthermia applications* (pp. 317-337). Cambridge, Massachusetts, United States: Elsevier.

Berry, C. C., Wells, S., Charles, S., & Curtis, A. S. (2003). Dextran and albumin derivatised iron oxide nanoparticles: influence on fibroblasts in vitro. *Biomaterials, 24*(25), 4551-4557. doi:https://doi.org/10.1016/S0142-9612(03)00237-0

Bielas, R., Hornowski, T., Paulovičová, K., Rajňák, M., & Józefczak, A. (2020). The effect of magnetic particles covering the droplets on the heating rate of Pickering emulsions in the AC magnetic field. *Journal of Molecular Liquids, 320*, 114388. doi:https://doi.org/10.1016/j.molliq.2020.114388

Blanco-Andujar, C., Ortega, D., Pankhurst, Q. A., & Thanh, N. T. K. (2012). Elucidating the morphological and structural evolution of iron oxide nanoparticles formed by sodium carbonate in aqueous medium. *Journal of Materials Chemistry, 22*(25), 12498-12506. doi:10.1039/C2JM31295F

Blanco-Andujar, C., Teran, F., & Ortega, D. (2018). Current outlook and perspectives on nanoparticle-mediated magnetic hyperthermia. In M. Mahmoudi & S. Laurent (Eds.), *Iron oxide nanoparticles for biomedical applications* (pp. 197-245). London, United Kingdom: Elsevier.

Bloomfield, I. G., Johnston, I. H., & Bilston, L. E. (1998). Effects of proteins, blood cells and glucose on the viscosity of cerebrospinal fluid. *Pediatric Neurosurgery, 28*(5), 246-251. doi:10.1159/000028659

Bomatí-Miguel, O., Zhao, X., Martelli, S., Di Nunzio, P., & Veintemillas-Verdaguer, S. (2010). Modeling of the laser pyrolysis process by means of the aerosol theory: Case of iron nanoparticles. *Journal of Applied Physics, 107*(1), 014906. doi:https://doi.org/10.1063/1.3273483

Bouta, E. M., Wood, R. W., Brown, E. B., Rahimi, H., Ritchlin, C. T., & Schwarz, E. M. (2014). In vivo quantification of lymph viscosity and pressure in lymphatic vessels and draining lymph nodes of arthritic joints in mice. *The Journal of Physiology, 592*(6), 1213-1223. doi:10.1113/jphysiol.2013.266700

Bunge, A., Porav, A. S., Borodi, G., Radu, T., Pîrnău, A., Berghian-Grosan, C., & Turcu, R. (2019). Correlation between synthesis parameters and properties of magnetite clusters prepared by solvothermal polyol method. *Journal of Materials Science, 54*(4), 2853-2875. doi:https://doi.org/10.1007/s10853-018-3030-9

Cabrera, L., Gutierrez, S., Menendez, N., Morales, M. P., & Herrasti, P. (2008). Magnetite nanoparticles: electrochemical synthesis and characterization. *Electrochimica Acta, 53*(8), 3436-3441. doi:https://doi.org/10.1016/j.electacta.2007.12.006

Cao, Z.-f., Wen, X., Wang, J., Yang, F., Zhong, H., Wang, S., & Wu, Z.-k. (2019). In situ nano-Fe_3O_4/triisopropanolamine functionalized graphene oxide composites to enhance Pb^{2+} ions removal. *Colloids Surf. A Physicochem. Eng. Asp., 561*, 209-217. doi:https://doi.org/10.1016/j.colsurfa.2018.10.084

Cervantes, O., Casillas, N., Knauth, P., Lopez, Z., Virgen-Ortiz, A., Lozano, O., . . . Cano, M. E. (2020). An easily prepared ferrofluid with high power absorption density and low cytotoxicity for biomedical applications. *Materials Chemistry and Physics, 245*, 122752. doi:https://doi.org/10.1016/j.matchemphys.2020.122752

Chang, D., Lim, M., Goos, J. A. C. M., Qiao, R., Ng, Y. Y., Mansfeld, F. M., . . . Kavallaris, M. (2018). Biologically targeted magnetic hyperthermia: potential and limitations. *Frontiers in pharmacology, 9*, 831-831. doi:10.3389/fphar.2018.00831

Chen, M.-L., Gao, Z.-W., Chen, X.-M., Pang, S.-C., & Zhang, Y. (2018). Laser-assisted in situ synthesis of graphene-based magnetic-responsive hybrids for multimodal imaging-guided chemo/photothermal synergistic therapy. *Talanta, 182*, 433-442. doi:https://doi.org/10.1016/j.talanta.2018.02.030

Chen, W., Wen, X., Zhen, G., & Zheng, X. (2015). Assembly of Fe_3O_4 nanoparticles on PEG-functionalized graphene oxide for efficient magnetic imaging and drug delivery. *Rsc Advances, 5*(85), 69307-69311. doi:https://doi.org/10.1039/C5RA09901C

Chen, W., Yan, L., & Bangal, P. R. (2010). Preparation of graphene by the rapid and mild thermal reduction of graphene oxide induced by microwaves. *Carbon, 48*(4), 1146-1152. doi:https://doi.org/10.1016/j.carbon.2009.11.037

Cornell, R. M., & Schwertmann, U. (2003). *The iron oxides: structure, properties, reactions, occurrences and uses*. Weinheim, Germany: John Wiley & Sons.

Crivellaro, S., Guadagnini, A., Arboleda, D. M., Schinca, D., & Amendola, V. (2019). A system for the synthesis of nanoparticles by laser ablation in liquid that is remotely controlled with PC or smartphone. *Review of Scientific Instruments, 90*(3), 033902. doi:https://doi.org/10.1063/1.5083811

D'Souza, A. J. M., Schowen, R. L., & Topp, E. M. (2004). Polyvinylpyrrolidone–drug conjugate: synthesis and release mechanism. *Journal of controlled release, 94*(1), 91-100. doi:https://doi.org/10.1016/j.jconrel.2003.09.014

da Silva Júnior, W. F., de Oliveira Pinheiro, J. G., Moreira, C. D. L. F. A., de Souza, F. J. J., & de Lima, Á. A. N. (2017). Chapter 15 - Alternative technologies to improve solubility and stability of poorly water-soluble drugs. In A. M. Grumezescu (Ed.), *Multifunctional systems for combined delivery, biosensing and diagnostics* (pp. 281-305). Philadelphia, United States: Elsevier.

Dabbagh, A., Hedayatnasab, Z., Karimian, H., Sarraf, M., Yeong, C. H., Madaah Hosseini, H. R., . . . Rahman, N. A. (2019). Polyethylene glycol-coated porous magnetic nanoparticles for targeted delivery of chemotherapeutics under magnetic hyperthermia condition. *Int J Hyperthermia, 36*(1), 104-114. doi:10.1080/02656736.2018.1536809

Dadfar, S. M., Roemhild, K., Drude, N. I., von Stillfried, S., Knüchel, R., Kiessling, F., & Lammers, T. (2019). Iron oxide nanoparticles: diagnostic, therapeutic and theranostic applications. *Advanced Drug Delivery Reviews, 138*, 302-325. doi:https://doi.org/10.1016/j.addr.2019.01.005

Dalal, M., Greneche, J.-M., Satpati, B., Ghzaiel, T. B., Mazaleyrat, F., Ningthoujam, R. S., & Chakrabarti, P. K. (2017). Microwave Absorption and the Magnetic Hyperthermia Applications of $Li_{0.3}Zn_{0.3}Co_{0.1}Fe_{2.3}O_4$ Nanoparticles in Multiwalled Carbon Nanotube Matrix. *ACS applied materials & interfaces, 9*(46), 40831-40845. doi:10.1021/acsami.7b12091

Das, S., Hendry, M. J., & Essilfie-Dughan, J. (2011). Transformation of two-line ferrihydrite to goethite and hematite as a function of pH and temperature. *Environmental Science & Technology, 45*(1), 268-275. doi:10.1021/es101903y

de la Presa, P., Luengo, Y., Multigner, M., Costo, R., Morales, M. P., Rivero, G., & Hernando, A. (2012). Study of heating efficiency as a function of concentration, size, and applied field in γ-Fe_2O_3 nanoparticles. *The Journal of Physical Chemistry C, 116*(48), 25602-25610. doi:10.1021/jp310771p

Deatsch, A. E., & Evans, B. A. (2014). Heating efficiency in magnetic nanoparticle hyperthermia. *Journal of Magnetism and Magnetic Materials, 354*, 163-172. doi:https://doi.org/10.1016/j.jmmm.2013.11.006

Deng, L., Li, Q., Al-Rehili, S. a., Omar, H., Almalik, A., Alshamsan, A., . . . interfaces. (2016). Hybrid iron oxide–graphene oxide–polysaccharides microcapsule: a micro-matryoshka for on-demand drug release and antitumor therapy in vivo. *8*(11), 6859-6868. Retrieved from https://pubs.acs.org/doi/pdfplus/10.1021/acsami.6b00322

Dennis, C. L., Jackson, A. J., Borchers, J. A., Hoopes, P. J., Strawbridge, R., Foreman, A. R., . . . Ivkov, R. (2009). Nearly complete regression of tumors via collective behavior of magnetic nanoparticles in hyperthermia. *Nanotechnology, 20*(39), 395103. doi:10.1088/0957-4484/20/39/395103

Depan, D., Girase, B., Shah, J. S., & Misra, R. D. K. (2011). Structure–process–property relationship of the polar graphene oxide-mediated cellular response and stimulated growth of osteoblasts on hybrid chitosan network structure nanocomposite scaffolds. *Acta biomaterialia, 7*(9), 3432-3445. doi:https://doi.org/10.1016/j.actbio.2011.05.019

Diana, C.-R., Humberto, H.-S., & Jorge, Y.-F. (2019). Structural characterization and rheological properties of dextran produced by native strains isolated of Agave salmiana. *Food Hydrocolloids, 90*, 1-8. doi:https://doi.org/10.1016/j.foodhyd.2018.11.052

Disch, S., Wetterskog, E., Hermann, R. P., Wiedenmann, A., Vainio, U., Salazar-Alvarez, G., . . . Brückel, T. (2012). Quantitative spatial magnetization distribution in iron oxide nanocubes and nanospheres by polarized small-angle neutron scattering. *New journal of physics, 14*(1), 013025. doi:https://doi.org/10.1088/1367-2630/14/1/013025

Domenech, M., Marrero-Berrios, I., Torres-Lugo, M., & Rinaldi, C. (2013). Lysosomal membrane permeabilization by targeted magnetic nanoparticles in alternating magnetic fields. *ACS nano, 7*(6), 5091-5101. doi:10.1021/nn4007048

Dutta, B., Shetake, N. G., Gawali, S. L., Barick, B., Barick, K., Babu, P., . . . Hassan, P. (2018). PEG mediated shape-selective synthesis of cubic Fe_3O_4 nanoparticles for cancer therapeutics. *Journal of Alloys and Compounds, 737*, 347-355. doi:https://doi.org/10.1016/j.jallcom.2017.12.028

Eda, G., & Chhowalla, M. (2010). Chemically derived graphene oxide: towards large-area thin-film electronics and optoelectronics. *Advanced materials, 22*(22), 2392-2415. doi:https://doi.org/10.1002/adma.200903689

Eivazzadeh-Keihan, R., Maleki, A., de la Guardia, M., Bani, M. S., Chenab, K. K., Pashazadeh-Panahi, P., . . . Hamblin, M. R. (2019). Carbon based nanomaterials for tissue engineering of bone: Building new bone on small black scaffolds: A review. *Journal of Advanced Research, 18*, 185-201. doi:https://doi.org/10.1016/j.jare.2019.03.011

Elbialy, N. S., Fathy, M. M., & Khalil, W. M. (2014). Preparation and characterization of magnetic gold nanoparticles to be used as doxorubicin nanocarriers. *Physica Medica, 30*(7), 843-848. doi:https://doi.org/10.1016/j.ejmp.2014.05.012

Elbialy, N. S., Fathy, M. M., & Khalil, W. M. (2015). Doxorubicin loaded magnetic gold nanoparticles for in vivo targeted drug delivery. *International Journal of Pharmaceutics, 490*(1), 190-199. doi:https://doi.org/10.1016/j.ijpharm.2015.05.032

Elbialy, N. S., Fathy, M. M., Reem, A.-W., Darwesh, R., Abdel-dayem, U. A., Aldhahri, M., . . . AL-ghamdi, A. A. (2019). Multifunctional magnetic-gold nanoparticles for efficient combined targeted drug delivery and interstitial photothermal therapy. *International journal of pharmaceutics, 554*, 256-263. doi:https://doi.org/10.1016/j.ijpharm.2018.11.021

Espinosa, A., Di Corato, R., Kolosnjaj-Tabi, J., Flaud, P., Pellegrino, T., & Wilhelm, C. (2016). Duality of iron oxide nanoparticles in cancer therapy: amplification of heating efficiency by magnetic hyperthermia and photothermal bimodal treatment. *ACS nano, 10*(2), 2436-2446. doi:10.1021/acsnano.5b07249

Farazi, R., Vaezi, M., Molaei, M., Saeidifar, M., & Behnam-Ghader, A. (2018). Effect of pH and temperature on doxorubicin hydrochloride release from magnetite/graphene oxide nanocomposites. *Materials Today: Proceedings, 5*(7), 15726-15732. doi:https://doi.org/10.1016/j.matpr.2018.04.184

Fatemi, M., Mollania, N., Momeni-Moghaddam, M., & Sadeghifar, F. (2018). Extracellular biosynthesis of magnetic iron oxide nanoparticles by Bacillus cereus

strain HMH1: Characterization and in vitro cytotoxicity analysis on MCF-7 and 3T3 cell lines. *Journal of Biotechnology, 270*, 1-11. doi:https://doi.org/10.1016/j.jbiotec.2018.01.021

Fatima, H., Lee, D.-W., Yun, H. J., & Kim, K.-S. (2018). Shape-controlled synthesis of magnetic Fe_3O_4 nanoparticles with different iron precursors and capping agents. *Rsc Advances, 8*(41), 22917-22923. doi:https://doi.org/10.1039/C8RA02909A

Feng, B., Hong, R., Wang, L., Guo, L., Li, H., Ding, J., . . . Wei, D. (2008). Synthesis of Fe_3O_4/APTES/PEG diacid functionalized magnetic nanoparticles for MR imaging. *Colloids and Surfaces A: Physicochemical and Engineering Aspects, 328*(1-3), 52-59. doi:https://doi.org/10.1016/j.colsurfa.2008.06.024

Feng, Q., Liu, Y., Huang, J., Chen, K., Huang, J., & Xiao, K. (2018). Uptake, distribution, clearance, and toxicity of iron oxide nanoparticles with different sizes and coatings. *Scientific reports, 8*(1), 2082. doi:10.1038/s41598-018-19628-z

Feng, X.-J., He, X., Lai, L., Lu, Q., Cheng, L., & Wu, J. (2021). Polydopamine-anchored polyether on Fe_3O_4 as magnetic recyclable nanoparticle-demulsifiers. *Colloids Surf. A Physicochem. Eng. Asp., 617*, 126142. doi:10.1016/j.colsurfa.2021.126142

Field, S. B., & Bleehen, N. M. (1979). Hyperthermia in the treatment of cancer. *Cancer Treatment Reviews, 6*(2), 63-94. doi:https://doi.org/10.1016/S0305-7372(79)80043-2

Fortin, J.-P., Wilhelm, C., Servais, J., Ménager, C., Bacri, J.-C., & Gazeau, F. (2007). Size-sorted anionic iron oxide nanomagnets as colloidal mediators for magnetic hyperthermia. *Journal of the American Chemical Society, 129*(9), 2628-2635. doi:10.1021/ja067457e

Fotukian, S. M., Barati, A., Soleymani, M., & Alizadeh, A. M. (2020). Solvothermal synthesis of $CuFe_2O_4$ and Fe_3O_4 nanoparticles with high heating efficiency for magnetic hyperthermia application. *Journal of Alloys and Compounds, 816*, 152548. doi:https://doi.org/10.1016/j.jallcom.2019.152548

Fu, R., Yan, Y., Roberts, C., Liu, Z., & Chen, Y. (2018). The role of dipole interactions in hyperthermia heating colloidal clusters of densely-packed superparamagnetic nanoparticles. *Scientific reports, 8*(1), 4704-4704. doi:10.1038/s41598-018-23225-5

Ganesan, V., Lahiri, B., Louis, C., Philip, J., & Damodaran, S. P. (2019). Size-controlled synthesis of superparamagnetic magnetite nanoclusters for heat generation in an alternating magnetic field. *Journal of Molecular Liquids, 281*, 315-323. doi:https://doi.org/10.1016/j.molliq.2019.02.095

Gangwar, A., Singh, G., Shaw, S. K., Mandal, R. K., Sharma, A., Meena, S. S., . . . Prasad, N. K. (2019). Synthesis and structural characterization of $Co_xFe_{3-x}C$ ($0 \leq x \leq 0.3$) magnetic nanoparticles for biomedical applications. *New Journal of Chemistry, 43*(8), 3536-3544. doi:10.1039/C8NJ05240A

Gao, Y., Yang, C., Liu, X., Ma, R., Kong, D., & Shi, L. (2012). A Multifunctional nanocarrier based on nanogated mesoporous silica for enhanced tumor-specific uptake and intracellular delivery. *Macromolecular Bioscience, 12*(2), 251-259. doi:10.1002/mabi.201100208

García-Peña, N.-G., Díaz, D., Rodriguez-Gattorno, G., Betancourt, I., & Zumeta-Dube, I. (2018). Facile synthesis of rod-shaped bismuth sulfide@graphene oxide (Bi_2S_3@GO) composite. *Materials Chemistry and Physics, 219*, 376-389. doi:https://doi.org/10.1016/j.matchemphys.2018.08.052

Gatenby, R. A., & Gillies, R. J. (2004). Why do cancers have high aerobic glycolysis? *Nature Reviews Cancer, 4*(11), 891-899. doi:10.1038/nrc1478

Gawali, S. L., Barick, B. K., Barick, K. C., & Hassan, P. A. (2017). Effect of sugar alcohol on colloidal stabilization of magnetic nanoparticles for hyperthermia and drug delivery applications. *Journal of Alloys and Compounds, 725*, 800-806. doi:https://doi.org/10.1016/j.jallcom.2017.07.206

Gerweck, L. E., & Seetharaman, K. (1996). Cellular pH gradient in tumor *versus* normal tissue: potential exploitation for the treatment of cancer. *Cancer Research, 56*(6), 1194-1198.

Ghavami, M., Mohammadi, R., Koohi, M., & Kassaee, M. (2014). Visible light photocatalytic activity of reduced graphene oxide synergistically enhanced by successive inclusion of γ-Fe_2O_3, TiO_2, and Ag nanoparticles. *Materials Science in Semiconductor Processing, 26*, 69-78. doi:https://doi.org/10.1016/j.mssp.2014.04.007

Gil, S., Castro, E., & Mano, J. F. (2013). Synthesis and characterization of stable dicarboxylic pegylated magnetite nanoparticles. *Materials Letters, 100*, 266-270. doi:https://doi.org/10.1016/j.matlet.2013.03.058

Goodship, V., & Jacobs, D. (2009). *Polyvinyl alcohol: materials, processing and applications* (Vol. 16): Smithers Rapra Technology.

Goossens, V., Wielant, J., Van Gils, S., Finsy, R., & Terryn, H. (2006). Optical properties of thin iron oxide films on steel. *Surface and Interface Analysis, 38*(4), 489-493. doi:10.1002/sia.2219

Gupta, A. K., & Curtis, A. S. (2004). Surface modified superparamagnetic nanoparticles for drug delivery: interaction studies with human fibroblasts in culture. *Journal of Materials Science: Materials in Medicine, 15*(4), 493-496. doi:https://doi.org/10.1023/B:JMSM.0000021126.32934.20

Gupta, A. K., & Gupta, M. (2005). Synthesis and surface engineering of iron oxide nanoparticles for biomedical applications. *Biomaterials, 26*(18), 3995-4021. doi:https://doi.org/10.1016/j.biomaterials.2004.10.012

Halilu, A., Ali, T. H., Atta, A. Y., Sudarsanam, P., Bhargava, S. K., & Abd Hamid, S. B. (2016). Highly selective hydrogenation of biomass-derived furfural into furfuryl alcohol using a novel magnetic nanoparticles catalyst. *Energy & Fuels, 30*(3), 2216-2226. doi:https://doi.org/10.1021/acs.energyfuels.5b02826

Halilu, A., Hayyan, M., Aroua, M. K., Yusoff, R., Hizaddin, H. F., & Basirun, W. J. (2021). Hybridized Fe/Ru-SiMWCNT-ionic liquid nanofluid for CO_2 conversion into carbamate using superoxide ion. *J. Environ. Chem. Eng., 9*(4), 105285. doi:10.1016/j.jece.2021.105285

Halilu, A., Umar, A. A., Balarabe, Y. U., Haniffa, M. A. C. M., Munawar, K., Sunku, K., & Sudarsanam, P. (2020). Advances in single-atom catalysts for lignin conversion. In *Advanced heterogeneous catalysts volume 2: Applications at the single-atom scale* (Vol. 1360, pp. 93-125): American Chemical Society.

Han, J., Luo, P., Wang, Y., Wang, L., Li, C., Zhang, W., . . . Ni, L. (2018). The development of nanobiocatalysis via the immobilization of cellulase on composite magnetic nanomaterial for enhanced loading capacity and catalytic activity. *International journal of biological macromolecules, 119*, 692-700. doi:https://doi.org/10.1016/j.ijbiomac.2018.07.176

Han, J., Wang, L., Wang, Y., Dong, J., Tang, X., Ni, L., & Wang, L. (2018). Preparation and characterization of Fe_3O_4-NH_2@ 4-arm-PEG-NH_2, a novel magnetic four-arm polymer-nanoparticle composite for cellulase immobilization. *Biochemical Engineering Journal, 130*, 90-98. doi:https://doi.org/10.1016/j.bej.2017.11.008

Hasany, S., Ahmed, I., Rajan, J., & Rehman, A. (2012). Systematic review of the preparation techniques of iron oxide magnetic nanoparticles. *Nanosci. Nanotechnol, 2*(6), 148-158. doi:10.5923/j.nn.20120206.01

Hashemi, M., Omidi, M., Muralidharan, B., Tayebi, L., Herpin, M. J., Mohagheghi, M. A., . . . Milner, T. E. (2018). Layer-by-layer assembly of graphene oxide on thermosensitive liposomes for photo-chemotherapy. *Acta biomaterialia, 65*, 376-392. doi:https://doi.org/10.1016/j.actbio.2017.10.040

Hawkins, C., & Williams, J. M. (1992). A mössbauer study of the superparamagnetic properties of reconstituted E. Coli BFR. In J. L. Dormann & D. Fiorani (Eds.), *Magnetic properties of fine particles* (pp. 417-422). Oxford, United Kingdom: Elsevier.

He, F., Fan, J., Ma, D., Zhang, L., Leung, C., & Chan, H. L. (2010). The attachment of Fe_3O_4 nanoparticles to graphene oxide by covalent bonding. *Carbon, 48*(11), 3139-3144. doi:https://doi.org/10.1016/j.carbon.2010.04.052

Hergt, R., & Dutz, S. (2007). Magnetic particle hyperthermia—biophysical limitations of a visionary tumour therapy. *Journal of Magnetism and Magnetic Materials, 311*(1), 187-192. doi:https://doi.org/10.1016/j.jmmm.2006.10.1156

Hergt, R., Dutz, S., & Röder, M. (2008). Effects of size distribution on hysteresis losses of magnetic nanoparticles for hyperthermia. *Journal of Physics: Condensed Matter, 20*(38), 385214. doi:10.1088/0953-8984/20/38/385214

Hergt, R., Hiergeist, R., Zeisberger, M., Glöckl, G., Weitschies, W., Ramirez, L. P., . . . Kaiser, W. A. (2004). Enhancement of AC-losses of magnetic nanoparticles for heating applications. *Journal of Magnetism and Magnetic Materials, 280*(2), 358-368. doi:https://doi.org/10.1016/j.jmmm.2004.03.034

Holzwarth, U., & Gibson, N. (2011). The Scherrer equation versus the 'Debye-Scherrer equation'. *Nature Nanotechnology, 6*(9), 534-534. doi:10.1038/nnano.2011.145

Hong, R. Y., Li, J. H., Li, H. Z., Ding, J., Zheng, Y., & Wei, D. G. (2008). Synthesis of Fe_3O_4 nanoparticles without inert gas protection used as precursors of magnetic fluids. *Journal of Magnetism and Magnetic Materials, 320*(9), 1605-1614. doi:https://doi.org/10.1016/j.jmmm.2008.01.015

Hong, Y. L., Ryu, S., Jeong, H. S., & Kim, Y.-K. (2019). Surface functionalization effect of graphene oxide on its liquid crystalline and assembly behaviors. *Applied Surface Science, 480*, 514-522. doi:https://doi.org/10.1016/j.apsusc.2019.03.023

Hossain, M. Z., Johns, J. E., Bevan, K. H., Karmel, H. J., Liang, Y. T., Yoshimoto, S., . . . Hersam, M. C. (2012). Chemically homogeneous and thermally reversible oxidation of epitaxial graphene. *Nature Chemistry, 4*, 305. doi:https://doi.org/10.1038/nchem.1269

Hsan, N., Dutta, P., Kumar, S., Bera, R., & Das, N. (2019). Chitosan grafted graphene oxide aerogel: Synthesis, characterization and carbon dioxide capture study. *International journal of biological macromolecules, 125*, 300-306. doi:https://doi.org/10.1016/j.ijbiomac.2018.12.071

Hu, J., Youssefian, S., Obayemi, J., Malatesta, K., Rahbar, N., & Soboyejo, W. (2018). Investigation of adhesive interactions in the specific targeting of Triptorelin-conjugated PEG-coated magnetite nanoparticles to breast cancer cells. *Acta biomaterialia, 71*, 363-378. doi:https://doi.org/10.1016/j.actbio.2018.02.011

Huang, N., Lim, H., Chia, C. H., Yarmo, M. A., & Muhamad, M. (2011). Simple room-temperature preparation of high-yield large-area graphene oxide. *International journal of nanomedicine, 6*, 3443. doi:10.2147/IJN.S26812

Huang, Y., Xiao, C.-f., Huang, Q.-l., Liu, H.-l., Hao, J.-q., & Song, L. (2018). Magnetic field induced orderly arrangement of Fe_3O_4/GO composite particles for preparation of Fe_3O_4/GO/PVDF membrane. *Journal of Membrane Science, 548*, 184-193. doi:https://doi.org/10.1016/j.memsci.2017.11.027

Iannazzo, D., Pistone, A., Salamò, M., Galvagno, S., Romeo, R., Giofré, S. V., . . . Di Pietro, A. (2017). Graphene quantum dots for cancer targeted drug delivery. *International journal of pharmaceutics, 518*(1-2), 185-192. doi:https://doi.org/10.1016/j.ijpharm.2016.12.060

Iravani, S. (2019). Bio-based synthesis of magnetic nanoparticles and their applications. In K. A. Abd-Elsalam, M. A. Mohamed, & R. Prasad (Eds.), *Magnetic nanostructures : environmental and agricultural applications* (pp. 13-31). Cham, Switzerland: Springer International Publishing.

Işıklan, N., Hussien, N. A., & Türk, M. (2021). Synthesis and drug delivery performance of gelatin-decorated magnetic graphene oxide nanoplatform. *Colloids Surf. A Physicochem. Eng. Asp., 616*, 126256. doi:https://doi.org/10.1016/j.colsurfa.2021.126256

Ito, A., Kuga, Y., Honda, H., Kikkawa, H., Horiuchi, A., Watanabe, Y., & Kobayashi, T. (2004). Magnetite nanoparticle-loaded anti-HER2 immunoliposomes for combination of antibody therapy with hyperthermia. *Cancer Letters, 212*(2), 167-175. doi:https://doi.org/10.1016/j.canlet.2004.03.038

Jadhav, S. V., Shewale, P. S., Shin, B. C., Patil, M. P., Kim, G. D., Rokade, A. A., . . . Yu, Y. S. (2019). Study of structural and magnetic properties and heat induction of gadolinium-substituted manganese zinc ferrite nanoparticles for in vitro magnetic fluid hyperthermia. *Journal of Colloid and Interface Science, 541*, 192-203. doi:https://doi.org/10.1016/j.jcis.2019.01.063

Jana, N. R., Chen, Y., & Peng, X. (2004). Size-and shape-controlled magnetic (Cr, Mn, Fe, Co, Ni) oxide nanocrystals via a simple and general approach. *Chemistry of materials, 16*(20), 3931-3935. doi:https://doi.org/10.1021/cm049221k

Jang, J., Hong, J., & Cha, C. (2017). Effects of precursor composition and mode of crosslinking on mechanical properties of graphene oxide reinforced composite hydrogels. *Journal of the mechanical behavior of biomedical materials, 69*, 282-293. doi:https://doi.org/10.1016/j.jmbbm.2017.01.025

Jordan, A., Scholz, R., Wust, P., Fähling, H., & Roland, F. (1999). Magnetic fluid hyperthermia (MFH): cancer treatment with AC magnetic field induced excitation of biocompatible superparamagnetic nanoparticles. *Journal of Magnetism and Magnetic Materials, 201*(1), 413-419. doi:https://doi.org/10.1016/S0304-8853(99)00088-8

Jordan, A., Scholz, R., Wust, P., Schirra, H., Thomas, S., Schmidt, H., & Felix, R. (1999). Endocytosis of dextran and silan-coated magnetite nanoparticles and the effect of intracellular hyperthermia on human mammary carcinoma cells in vitro. *Journal of Magnetism and Magnetic Materials, 194*(1), 185-196. doi:https://doi.org/10.1016/S0304-8853(98)00558-7

Jordan, A., Wust, P., Fählin, H., John, W., Hinz, A., & Felix, R. (1993). Inductive heating of ferrimagnetic particles and magnetic fluids: Physical evaluation of their potential for hyperthermia. *International Journal of Hyperthermia, 9*(1), 51-68. doi:10.3109/02656739309061478

Karaman, S., Karaipekli, A., Sarı, A., & Biçer, A. (2011). Polyethylene glycol (PEG)/diatomite composite as a novel form-stable phase change material for thermal energy storage. *Solar Energy Materials and Solar Cells, 95*(7), 1647-1653. doi:https://doi.org/10.1016/j.solmat.2011.01.022

Kesse, X., Adam, A., Begin-Colin, S., Mertz, D., Larquet, E., Gacoin, T., . . . Nedelec, J.-M. (2020). Elaboration of Superparamagnetic and Bioactive Multicore–Shell Nanoparticles (γ-Fe2O3@SiO2-CaO): A Promising Material for Bone Cancer Treatment. *ACS applied materials & interfaces, 12*(42), 47820-47830. doi:10.1021/acsami.0c12769

Khan, W. S., Hamadneh, N. N., & Khan, W. A. (2017). Prediction of thermal conductivity of polyvinylpyrrolidone (PVP) electrospun nanocomposite fibers using artificial neural network and prey-predator algorithm. *PloS one, 12*(9), e0183920. doi:https://doi.org/10.1371/journal.pone.0183920

Kharat, P. B., Somvanshi, S. B., Khirade, P. P., & Jadhav, K. M. (2020). Induction heating analysis of surface-functionalized nanoscale $CoFe_2O_4$ for magnetic fluid hyperthermia toward noninvasive cancer treatment. *ACS Omega, 5*(36), 23378-23384. doi:10.1021/acsomega.0c03332

Kharisov, B. I., Rasika Dias, H. V., Kharissova, O. V., Manuel Jiménez-Pérez, V., Olvera Pérez, B., & Muñoz Flores, B. (2012). Iron-containing nanomaterials: synthesis, properties, and environmental applications. *Rsc Advances, 2*(25), 9325-9358. doi:10.1039/C2RA20812A

Khoee, S., Saadatinia, A., & Bafkary, R. (2017). Ultrasound-assisted synthesis of pH-responsive nanovector based on PEG/chitosan coated magnetite nanoparticles for 5-FU delivery. *Ultrasonics Sonochemistry, 39*, 144-152. doi:https://doi.org/10.1016/j.ultsonch.2017.04.025

Kim, D. K., Zhang, Y., Voit, W., Rao, K. V., & Muhammed, M. (2001). Synthesis and characterization of surfactant-coated superparamagnetic monodispersed iron oxide nanoparticles. *Journal of Magnetism and Magnetic Materials, 225*(1), 30-36. doi:https://doi.org/10.1016/S0304-8853(00)01224-5

Kim, H. J., & Choi, H. (2019). Effect of plasma treatment on magnetic properties and heating efficiency of Ni-Zn nanoparticles. *Journal of Magnetism and Magnetic Materials, 484*, 14-20. doi:https://doi.org/10.1016/j.jmmm.2019.03.102

Kim, J., Cote, L. J., Kim, F., Yuan, W., Shull, K. R., & Huang, J. (2010). Graphene oxide sheets at interfaces. *Journal of the American Chemical Society, 132*(23), 8180-8186. doi:10.1021/ja102777p

Kim, S.-W., Kim, H.-K., Lee, K., Roh, K. C., Han, J. T., Kim, K.-B., . . . Jung, M.-H. (2019). Studying the reduction of graphene oxide with magnetic measurements. *Carbon, 142*, 373-378. doi:https://doi.org/10.1016/j.carbon.2018.10.068

Kobayashi, T., Kimura, N., Chi, J., Hirata, S., & Hobara, D. (2010). Channel-length-dependent field-effect mobility and carrier concentration of reduced graphene oxide thin-film transistors. *Small, 6*(11), 1210-1215. doi:https://doi.org/10.1002/smll.200902407

Köçkar, H., Karaagac, O., & Özel, F. (2019). Effects of biocompatible surfactants on structural and corresponding magnetic properties of iron oxide nanoparticles coated by hydrothermal process. *Journal of Magnetism and Magnetic Materials, 474*, 332-336. doi:https://doi.org/10.1016/j.jmmm.2018.11.053

Kolhatkar, A. G., Jamison, A. C., Litvinov, D., Willson, R. C., & Lee, T. R. (2013). Tuning the magnetic properties of nanoparticles. *International journal of molecular sciences, 14*(8), 15977-16009. doi:10.3390/ijms140815977

Koushkbaghi, S., Jafari, P., Rabiei, J., Irani, M., & Aliabadi, M. (2016). Fabrication of PET/PAN/GO/Fe_3O_4 nanofibrous membrane for the removal of Pb (II) and Cr (VI) ions. *Chemical Engineering Journal, 301*, 42-50. doi:https://doi.org/10.1016/j.cej.2016.04.076

Krupskaya, Y., Mahn, C., Parameswaran, A., Taylor, A., Krämer, K., Hampel, S., . . . Klingeler, R. (2009). Magnetic study of iron-containing carbon nanotubes: Feasibility for magnetic hyperthermia. *Journal of Magnetism and Magnetic Materials, 321*(24), 4067-4071. doi:https://doi.org/10.1016/j.jmmm.2009.08.005

Kumar, R., Chauhan, A., Jha, S. K., & Kuanr, B. K. (2018). Localized cancer treatment by radio-frequency hyperthermia using magnetic nanoparticles immobilized on graphene oxide: from novel synthesis to in vitro studies. *Journal of Materials Chemistry B, 6*(33), 5385-5399. doi:https://doi.org/10.1039/C8TB01365A

LaGrow, A. P., Besenhard, M. O., Hodzic, A., Sergides, A., Bogart, L., Gavriilidis, A., & Thanh, N. T. K. (2019). Unravelling the growth mechanism of the Co-precipitation of iron oxide nanoparticles with the aid of synchrotron X-ray diffraction in solution. *Nanoscale*. doi:https://doi.org/10.1039/C9NR00531E

Lahiri, B. B., Ranoo, S., & Philip, J. (2017). Magnetic hyperthermia study in water based magnetic fluids containing TMAOH coated Fe_3O_4 using infrared thermography. *Infrared Physics & Technology, 80*, 71-82. doi:https://doi.org/10.1016/j.infrared.2016.11.015

Lanier, O. L., Korotych, O. I., Monsalve, A. G., Wable, D., Savliwala, S., Grooms, N. W. F., . . . Dobson, J. (2019). Evaluation of magnetic nanoparticles for magnetic fluid hyperthermia. *International Journal of Hyperthermia, 36*(1), 687-701. doi:10.1080/02656736.2019.1628313

Layek, R. K., & Nandi, A. K. (2013). A review on synthesis and properties of polymer functionalized graphene. *Polymer, 54*(19), 5087-5103. doi:https://doi.org/10.1016/j.polymer.2013.06.027

Li, M., Gu, H., & Zhang, C. (2012). Highly sensitive magnetite nano clusters for MR cell imaging. *Nanoscale Research Letters, 7*(1), 204. doi:10.1186/1556-276X-7-204

Liang, Y.-J., Fan, F., Ma, M., Sun, J., Chen, J., Zhang, Y., & Gu, N. (2017). Size-dependent electromagnetic properties and the related simulations of Fe_3O_4 nanoparticles made by microwave-assisted thermal decomposition. *Colloids and Surfaces A: Physicochemical and Engineering Aspects, 530*, 191-199. doi:https://doi.org/10.1016/j.colsurfa.2017.06.059

Lin, G., Chen, T., Pan, Y., Yang, Z., Li, L., Yong, K.-T., . . . Xu, G. (2020). Biodistribution and acute toxicity of cadmium-free quantum dots with different surface functional groups in mice following intratracheal inhalation. *Nanotheranostics, 4*(3), 173-183. doi:10.7150/ntno.42786

Liu, J., Luo, Z., Zhang, J., Luo, T., Zhou, J., Zhao, X., & Cai, K. (2016). Hollow mesoporous silica nanoparticles facilitated drug delivery via cascade pH stimuli in tumor microenvironment for tumor therapy. *Biomaterials, 83*, 51-65. doi:https://doi.org/10.1016/j.biomaterials.2016.01.008

Liu, S., Guo, D., & Xie, G. (2012). Nanoscale lubricating film formation by linear polymer in aqueous solution. *Journal of Applied Physics, 112*(10), 104309. doi:10.1063/1.4765674

Liu, X., Peng, M., Li, G., Miao, Y., Luo, H., Jing, G., . . . Fan, H. (2019). Ultrasonication-triggered ubiquitous assembly of magnetic janus amphiphilic nanoparticles in cancer theranostic applications. *Nano Letters, 19*(6), 4118-4125. doi:10.1021/acs.nanolett.9b01524

Liu, X., Yan, B., Li, Y., Ma, X., Jiao, W., Shi, K., . . . Fan, H. (2020). Graphene oxide-grafted magnetic nanorings mediated magnetothermodynamic therapy favoring reactive oxygen species-related immune response for enhanced antitumor efficacy. *ACS nano, 14*(2), 1936-1950. doi:10.1021/acsnano.9b08320

Liu, X. H., Liu, W., & Zhang, Z. D. (2017). Evolution of magnetic properties in the vicinity of the Verwey transition in Fe_3O_4 thin films. *Physical Review B, 96*(9). doi:10.1103/physrevb.96.094405

Liu, Y., Li, Y., Li, X.-M., & He, T. (2013). Kinetics of (3-Aminopropyl)triethoxylsilane (APTES) silanization of superparamagnetic iron oxide nanoparticles. *Langmuir, 29*(49), 15275-15282. doi:10.1021/la403269u

Low, F. W., Lai, C. W., Abd Hamid, S. B., Chong, S. W., & Liu, W. W. (2015). High yield preparation of graphene oxide film using improved Hummer's technique for current-voltage characteristic. *Advanced Materials Research, 1109*, 385-389. doi:https://doi.org/10.4028/www.scientific.net/AMR.1109.385

Lozano, I., Casillas, N., de León, C. P., Walsh, F., & Herrasti, P. (2017). New insights into the electrochemical formation of magnetite nanoparticles. *Journal of The Electrochemical Society, 164*(4), D184-D191. doi:10.1149/2.1091704jes

Ma, M., Wu, Y., Zhou, J., Sun, Y., Zhang, Y., & Gu, N. (2004). Size dependence of specific power absorption of Fe_3O_4 particles in AC magnetic field. *Journal of Magnetism and Magnetic Materials, 268*(1), 33-39. doi:https://doi.org/10.1016/S0304-8853(03)00426-8

Ma, X., Tao, H., Yang, K., Feng, L., Cheng, L., Shi, X., . . . Liu, Z. (2012). A functionalized graphene oxide-iron oxide nanocomposite for magnetically targeted drug delivery, photothermal therapy, and magnetic resonance imaging. *Nano Research, 5*(3), 199-212. doi:https://doi.org/10.1007/s12274-012-0200-y

Ma, X., Wang, Y., Liu, X.-L., Ma, H., Li, G., Li, Y., . . . Liang, X.-J. (2019). Fe_3O_4–Pd Janus nanoparticles with amplified dual-mode hyperthermia and enhanced ROS generation for breast cancer treatment. *Nanoscale Horizons, 4*(6), 1450-1459. doi:10.1039/C9NH00233B

Mahanta, N. K., & Abramson, A. R. (2012, 30 May-1 June 2012). *Thermal conductivity of graphene and graphene oxide nanoplatelets.* Paper presented at the 13th InterSociety Conference on Thermal and Thermomechanical Phenomena in Electronic Systems.

Mahmoudi, K., Bouras, A., Bozec, D., Ivkov, R., & Hadjipanayis, C. (2018). Magnetic hyperthermia therapy for the treatment of glioblastoma: a review of the therapy's history, efficacy and application in humans. *International Journal of Hyperthermia, 34*(8), 1316-1328. doi:10.1080/02656736.2018.1430867

Mai, B. T., Balakrishnan, P. B., Barthel, M. J., Piccardi, F., Niculaes, D., Marinaro, F., . . . Pellegrino, T. (2019). Thermoresponsive iron oxide nanocubes for an effective clinical translation of magnetic hyperthermia and heat-mediated chemotherapy. *ACS applied materials & interfaces, 11*(6), 5727-5739. doi:10.1021/acsami.8b16226

Maity, D., Chandrasekharan, P., Feng, S., & Jun, D. (2010, 22-26 Feb. 2010). *Synthesis and studies of APTES functionalized magnetite nanoparticles.* Paper presented at the 2010 International Conference on Nanoscience and Nanotechnology.

Maity, D., Chandrasekharan, P., Pradhan, P., Chuang, K.-H., Xue, J.-M., Feng, S.-S., & Ding, J. (2011). Novel synthesis of superparamagnetic magnetite nanoclusters for biomedical applications. *Journal of Materials Chemistry, 21*(38), 14717-14724. doi:https://doi.org/10.1039/C1JM11982F

Manohar, A., & Krishnamoorthi, C. (2017). Low curie-transition temperature and superparamagnetic nature of Fe_3O_4 nanoparticles prepared by colloidal nanocrystal synthesis. *Materials Chemistry and Physics, 192*, 235-243. doi:https://doi.org/10.1016/j.matchemphys.2017.01.039

Manoukian, O. S., Sardashti, N., Stedman, T., Gailiunas, K., Ojha, A., Penalosa, A., . . . Kumbar, S. G. (2019). Biomaterials for tissue engineering and regenerative medicine. In R. Narayan (Ed.), *Encyclopedia of biomedical engineering* (pp. 462-482). Oxford: Elsevier.

Marcano, D. C., Kosynkin, D. V., Berlin, J. M., Sinitskii, A., Sun, Z., Slesarev, A., . . . Tour, J. M. (2010). Improved synthesis of graphene oxide. *ACS nano, 4*(8), 4806-4814. doi:10.1021/nn1006368

Martinez-Boubeta, C., Simeonidis, K., Makridis, A., Angelakeris, M., Iglesias, O., Guardia, P., . . . Baldomir, D. (2013). Learning from nature to improve the heat generation of iron-oxide nanoparticles for magnetic hyperthermia applications. *Scientific reports, 3*(1), 1652. doi:10.1038/srep01652

Masotti, A., & Caporali, A. (2013). Preparation of magnetic carbon nanotubes (Mag-CNTs) for biomedical and biotechnological applications. *International journal of molecular sciences, 14*(12), 24619-24642. doi:https://doi.org/10.3390/ijms141224619

Mbugua, S. N., Njenga, L. W., Odhiambo, R. A., Wandiga, S. O., & Onani, M. O. (2021). Beyond DNA-targeting in cancer chemotherapy. emerging frontiers - a review. *Current Topics in Medicinal Chemistry, 21*(1), 28-47. doi:10.2174/1568026620666200819160213

McGuire, S. (2016). World cancer report 2014. Geneva, Switzerland: World Health Organization, international agency for research on cancer, WHO Press, 2015. In: Oxford University Press.

Metin, Ö., Aydoğan, Ş., & Meral, K. (2014). A new route for the synthesis of graphene oxide–Fe_3O_4 (GO–Fe_3O_4) nanocomposites and their Schottky diode applications. *Journal of Alloys and Compounds, 585*, 681-688. doi:https://doi.org/10.1016/j.jallcom.2013.09.159

Mohanta, S. C., Saha, A., & Devi, P. S. (2018). PEGylated iron oxide nanoparticles for pH responsive drug delivery application. *Materials Today: Proceedings, 5*(3), 9715-9725. doi:https://doi.org/10.1016/j.matpr.2017.10.158

Molcan, M., Kaczmarek, K., Kubovcikova, M., Gojzewski, H., Kovac, J., Timko, M., & Józefczak, A. (2020). Magnetic hyperthermia study of magnetosome chain systems in tissue-mimicking phantom. *Journal of Molecular Liquids, 320*, 114470. doi:https://doi.org/10.1016/j.molliq.2020.114470

Mondal, P., Anweshan, A., & Purkait, M. K. (2020). Green synthesis and environmental application of iron-based nanomaterials and nanocomposite: A review. *Chemosphere, 259*, 127509. doi:10.1016/j.chemosphere.2020.127509

Moroz, P., Jones, S. K., & Gray, B. N. (2002). Magnetically mediated hyperthermia: current status and future directions. *International Journal of Hyperthermia, 18*(4), 267-284. doi:10.1080/02656730110108785

Mourdikoudis, S., Pallares, R. M., & Thanh, N. T. K. (2018). Characterization techniques for nanoparticles: comparison and complementarity upon studying nanoparticle properties. *Nanoscale, 10*(27), 12871-12934. doi:10.1039/C8NR02278J

Muela, A., Muñoz, D., Martín-Rodríguez, R., Orue, I., Garaio, E., Abad Díaz de Cerio, A., . . . Fdez-Gubieda, M. L. (2016). Optimal parameters for hyperthermia treatment using biomineralized magnetite nanoparticles: theoretical and experimental approach. *The Journal of Physical Chemistry C, 120*(42), 24437-24448. doi:10.1021/acs.jpcc.6b07321

Muhammad, W., Khan, M. A., Nazir, M., Siddiquah, A., Mushtaq, S., Hashmi, S. S., & Abbasi, B. H. (2019). Papaver somniferum L. mediated novel bioinspired lead oxide (PbO) and iron oxide (Fe_2O_3) nanoparticles: In-vitro biological applications, biocompatibility and their potential towards HepG2 cell line. *Materials Science and Engineering: C, 103*, 109740. doi:https://doi.org/10.1016/j.msec.2019.109740

Mukhopadhyay, A., Joshi, N., Chattopadhyay, K., & De, G. (2012). A facile synthesis of PEG-coated magnetite (Fe_3O_4) nanoparticles and their prevention of the reduction of cytochrome C. *ACS applied materials & interfaces, 4*(1), 142-149. doi:10.1021/am201166m

Mürbe, J., Rechtenbach, A., & Töpfer, J. (2008). Synthesis and physical characterization of magnetite nanoparticles for biomedical applications. *Materials Chemistry and Physics, 110*(2-3), 426-433. doi:https://doi.org/10.1016/j.matchemphys.2008.02.037

Muthurasu, A., Dhandapani, P., & Ganesh, V. (2016). Facile and simultaneous synthesis of graphene quantum dots and reduced graphene oxide for bio-imaging and supercapacitor applications. *New Journal of Chemistry, 40*(11), 9111-9124. doi:10.1039/C6NJ00586A

Niederberger, M. (2007). Nonaqueous sol–gel routes to metal oxide nanoparticles. *Accounts of Chemical Research, 40*(9), 793-800. doi:10.1021/ar600035e

Nielsen, O. S., Horsman, M., & Overgaard, J. (2001). A future for hyperthermia in cancer treatment? *European Journal of Cancer, 37*(13), 1587-1589. doi:https://doi.org/10.1016/S0959-8049(01)00193-9

Nikitin, A., Khramtsov, M., Garanina, A., Mogilnikov, P., Sviridenkova, N., Shchetinin, I., . . . Majouga, A. (2019). Synthesis of iron oxide nanorods for enhanced magnetic hyperthermia. *Journal of Magnetism and Magnetic Materials, 469*, 443-449. doi:https://doi.org/10.1016/j.jmmm.2018.09.014

Noh, S.-h., Na, W., Jang, J.-t., Lee, J.-H., Lee, E. J., Moon, S. H., . . . Cheon, J. (2012). Nanoscale magnetism control via surface and exchange anisotropy for optimized ferrimagnetic hysteresis. *Nano Letters, 12*(7), 3716-3721. doi:10.1021/nl301499u

Noqta, O. A., Aziz, A. A., Usman, I. A., & Bououdina, M. (2019). Recent advances in iron oxide nanoparticles (IONPs): synthesis and surface modification for biomedical applications. *Journal of Superconductivity and Novel Magnetism, 32*(4), 779-795. doi:https://doi.org/10.1007/s10948-018-4939-6

Obaidat, I. M., Issa, B., & Haik, Y. (2015). Magnetic properties of magnetic nanoparticles for efficient hyperthermia. *Nanomaterials (Basel, Switzerland), 5*(1), 63-89. doi:10.3390/nano5010063

Onyango, J. O., Chung, M. S., Eng, C.-H., Klees, L. M., Langenbacher, R., Yao, L., & An, M. (2015). Noncanonical amino acids to improve the pH response of pHLIP insertion at tumor acidity. *Angewandte Chemie International Edition, 54*(12), 3658-3663. doi:10.1002/anie.201409770

Parvez, K., Wu, Z.-S., Li, R., Liu, X., Graf, R., Feng, X., & Müllen, K. (2014). Exfoliation of graphite into graphene in aqueous solutions of inorganic salts. *Journal of the American Chemical Society, 136*(16), 6083-6091. doi:https://doi.org/10.1021/ja5017156

Pearce, J., Giustini, A., Stigliano, R., & Jack Hoopes, P. (2013). Magnetic heating of nanoparticles: the importance of particle clustering to achieve therapeutic temperatures. *Journal of nanotechnology in engineering and medicine, 4*(1), 110071-1100714. doi:10.1115/1.4024904

Pedersen, H. D. (2006). *The transformation of Fe (III) oxides catalysed by Fe^{2+} and the fate of arsenate during transformation and reduction of Fe (III) oxides*. Kgs. Lyngby: DTU Environment.

Pillai, K., Akhter, J., Chua, T. C., Shehata, M., Alzahrani, N., Al-Alem, I., & Morris, D. L. (2015). Heat sink effect on tumor ablation characteristics as observed in monopolar radiofrequency, bipolar radiofrequency, and microwave, using ex vivo calf liver model. *Medicine, 94*(9). doi:10.1097/MD.0000000000000580

Piñeiro-Redondo, Y., Bañobre-López, M., Pardiñas-Blanco, I., Goya, G., López-Quintela, M. A., & Rivas, J. (2011). The influence of colloidal parameters on the specific power absorption of PAA-coated magnetite nanoparticles. *Nanoscale Research Letters, 6*(1), 383. doi:10.1186/1556-276X-6-383

Prasad, A. I., Parchur, A. K., Juluri, R. R., Jadhav, N., Pandey, B. N., Ningthoujam, R. S., & Vatsa, R. K. (2013). Bi-functional properties of Fe_3O_4@YPO_4:Eu hybrid nanoparticles: hyperthermia application. *Dalton Transactions, 42*(14), 4885-4896. doi:10.1039/C2DT32508J

Qian, T., Li, J., Feng, W., & Nian, H. e. (2017). Single-walled carbon nanotube for shape stabilization and enhanced phase change heat transfer of polyethylene glycol phase change material. *Energy Conversion and Management, 143*, 96-108. doi:https://doi.org/10.1016/j.enconman.2017.03.065

Radini, I. A., Hasan, N., Malik, M. A., & Khan, Z. (2018). Biosynthesis of iron nanoparticles using Trigonella foenum-graecum seed extract for photocatalytic methyl orange dye degradation and antibacterial applications. *Journal of Photochemistry and Photobiology B: Biology, 183*, 154-163. doi:https://doi.org/10.1016/j.jphotobiol.2018.04.014

Rahimdad, N., Khalaj, A., Azarian, G., & Nematollahi, D. (2019). Electrochemical device for the synthesis of Fe_3O_4 magnetic nanoparticles. *Journal of The Electrochemical Society, 166*(2), E1. doi:https://doi.org/10.1149/2.0231902jes

Rajan, A., Sharma, M., & Sahu, N. K. (2020). Assessing magnetic and inductive thermal properties of various surfactants functionalised Fe_3O_4 nanoparticles for hyperthermia. *Scientific reports, 10*(1), 15045. doi:10.1038/s41598-020-71703-6

Rajan S, A., & Sahu, N. K. (2020). Inductive calorimetric assessment of iron oxide nano-octahedrons for magnetic fluid hyperthermia. *Colloids Surf. A Physicochem. Eng. Asp., 603*, 125210. doi:https://doi.org/10.1016/j.colsurfa.2020.125210

Ramezanzadeh, B., Ghasemi, E., Mahdavian, M., Changizi, E., & Moghadam, M. M. (2015). Characterization of covalently-grafted polyisocyanate chains onto graphene oxide for polyurethane composites with improved mechanical properties. *Chemical Engineering Journal, 281*, 869-883. doi:https://doi.org/10.1016/j.cej.2015.07.027

Ramya, C., Selvasekarapandian, S., Savitha, T., Hirankumar, G., Baskaran, R., Bhuvaneswari, M., & Angelo, P. (2006). Conductivity and thermal behavior of proton conducting polymer electrolyte based on poly (N-vinyl pyrrolidone). *European polymer journal, 42*(10), 2672-2677. doi:https://doi.org/10.1016/j.eurpolymj.2006.05.020

Ranjan, P., Shankar, S., Popovitz-Biro, R., Cohen, S. R., Kaplan-Ashiri, I., Dadosh, T., . . . van der Boom, M. E. (2018). Decoration of Inorganic nanostructures by metallic nanoparticles to induce fluorescence, enhance solubility, and tune band gap. *The Journal of Physical Chemistry C, 122*(12), 6748-6759. doi:10.1021/acs.jpcc.8b00510

Ranoo, S., Lahiri, B. B., Vinod, S., & Philip, J. (2019). Effect of initial susceptibility and relaxation dynamics on radio frequency alternating magnetic field induced heating in superparamagnetic nanoparticle dispersions. *Journal of Magnetism and Magnetic Materials, 486*, 165267. doi:https://doi.org/10.1016/j.jmmm.2019.165267

Raouf, I., Khalid, S., Khan, A., Lee, J., Kim, H. S., & Kim, M.-H. (2020). A review on numerical modeling for magnetic nanoparticle hyperthermia: Progress and challenges. *Journal of Thermal Biology, 91*, 102644. doi:https://doi.org/10.1016/j.jtherbio.2020.102644

Rasheed, T., Hassan, A. A., Kausar, F., Sher, F., Bilal, M., & Iqbal, H. M. N. (2020). Carbon nanotubes assisted analytical detection – Sensing/delivery cues for environmental and biomedical monitoring. *TRAC Trends in Analytical Chemistry, 132*, 116066. doi:10.1016/j.trac.2020.116066

Rask, M. B., Knopp, M. M., Olesen, N. E., Holm, R., & Rades, T. (2016). Influence of PVP/VA copolymer composition on drug–polymer solubility. *European Journal of Pharmaceutical Sciences, 85*, 10-17. doi:https://doi.org/10.1016/j.ejps.2016.01.026

Rego, G. N. d. A., Mamani, J. B., Souza, T. K. F., Nucci, M. P., Silva, H. R. d., & Gamarra, L. F. (2019). Therapeutic evaluation of magnetic hyperthermia using Fe_3O_4-aminosilane-coated iron oxide nanoparticles in glioblastoma animal model. *Einstein (Sao Paulo, Brazil), 17*(4), eAO4786. doi:10.31744/einstein_journal/2019AO4786

Revathy, R., Varma, M. R., & Surendran, K. P. (2021). Observation of cluster glass and griffiths-like phase in Fe_3O_4 nanostructures. *Phys. Status Solidi B Basic Res., 258*(2), 2000341. doi:https://doi.org/10.1002/pssb.202000341

Revia, R. A., & Zhang, M. (2016). Magnetite nanoparticles for cancer diagnosis, treatment, and treatment monitoring: recent advances. *Materials Today, 19*(3), 157-168. doi:https://doi.org/10.1016/j.mattod.2015.08.022

Rodio, M., Coluccino, L., Romeo, E., Genovese, A., Diaspro, A., Garau, G., & Intartaglia, R. (2017). Facile fabrication of bioactive ultra-small protein–hydroxyapatite nanoconjugates via liquid-phase laser ablation and their enhanced osteogenic differentiation activity. *Journal of Materials Chemistry B, 5*(2), 279-288. doi:https://doi.org/10.1039/C6TB02023B

Rodrigues, R. O., Baldi, G., Doumett, S., Garcia-Hevia, L., Gallo, J., Bañobre-López, M., . . . Lima, R. (2018). Multifunctional graphene-based magnetic nanocarriers for combined hyperthermia and dual stimuli-responsive drug delivery. *Materials Science and Engineering: C, 93*, 206-217. doi:https://doi.org/10.1016/j.msec.2018.07.060

Rodrigues, R. O., Bañobre-López, M., Gallo, J., Tavares, P. B., Silva, A. M., Lima, R., & Gomes, H. T. (2016). Haemocompatibility of iron oxide nanoparticles synthesized for theranostic applications: a high-sensitivity microfluidic tool. *Journal of Nanoparticle Research, 18*(7), 194. doi:https://doi.org/10.1007/s11051-016-3498-7

Rodríguez-Rodríguez, H., Salas, G., & Arias-Gonzalez, J. R. (2020). Heat generation in single magnetic nanoparticles under near-infrared irradiation. *The Journal of Physical Chemistry Letters*, 2182-2187. doi:10.1021/acs.jpclett.0c00143

Rosensweig, R. E. (2002). Heating magnetic fluid with alternating magnetic field. *Journal of Magnetism and Magnetic Materials, 252*, 370-374. doi:https://doi.org/10.1016/S0304-8853(02)00706-0

Rosso, K. M., Yanina, S. V., Gorski, C. A., Larese-Casanova, P., & Scherer, M. M. (2010). Connecting observations of hematite (α-Fe_2O_3) growth catalyzed by Fe(II). *Environmental Science & Technology, 44*(1), 61-67. doi:10.1021/es901882a

Rother, J., Nöding, H., Mey, I., & Janshoff, A. (2014). Atomic force microscopy-based microrheology reveals significant differences in the viscoelastic response between malign and benign cell lines. *Open Biology, 4*(5), 140046. doi:10.1098/rsob.140046

Saepudin, E., Fadhilah, H. R., & Khalil, M. (2020). The influence of carboxylate moieties for efficient loading and pH-controlled release of doxorubicin in Fe_3O_4 magnetic nanoparticles. *Colloids Surf. A Physicochem. Eng. Asp., 602*, 125137. doi:https://doi.org/10.1016/j.colsurfa.2020.125137

Sahne, F., Mohammadi, M., & Najafpour, G. D. (2019). Single-layer assembly of multifunctional carboxymethylcellulose on graphene oxide nanoparticles for improving in vivo curcumin delivery into tumor cells. *ACS Biomaterials Science & Engineering*. doi:10.1021/acsbiomaterials.8b01628

Salas, G., Veintemillas-Verdaguer, S., & Morales, M. d. P. (2013). Relationship between physico-chemical properties of magnetic fluids and their heating capacity. *International Journal of Hyperthermia, 29*(8), 768-776. doi:10.3109/02656736.2013.826824

Sánchez, J., Rodríguez-Reyes, M., Cortés-Hernández, D. A., Ávila-Orta, C. A., & Reyes-Rodríguez, P. Y. (2021). Heating capacity and biocompatibility of Pluronic-coated manganese gallium ferrites for magnetic hyperthermia treatment. *Colloids Surf. A Physicochem. Eng. Asp., 612*, 125986. doi:10.1016/j.colsurfa.2020.125986

Santoyo Salazar, J., Perez, L., de Abril, O., Truong Phuoc, L., Ihiawakrim, D., Vazquez, M., . . . Pourroy, G. (2011). Magnetic iron oxide nanoparticles in 10−40 nm range: composition in terms of magnetite/maghemite ratio and effect on the magnetic properties. *Chemistry of Materials, 23*(6), 1379-1386. doi:10.1021/cm103188a

Sarı, A., Biçer, A., & Alkan, C. (2020). Thermal energy storage properties of polyethylene glycol grafted styrenic copolymer as novel solid-solid phase change materials. *Int. J. Energy Res., 44*(5), 3976-3989. doi:https://doi.org/10.1002/er.5208

Schrand, A. M., Stacy, B. M., Payne, S., Dosser, L., & Hussain, S. M. (2011). Fundamental examination of nanoparticle heating kinetics upon near infrared (NIR) irradiation. *ACS applied materials & interfaces, 3*(10), 3971-3980. doi:10.1021/am2008536

Schwamb, T., Burg, B. R., Schirmer, N. C., & Poulikakos, D. (2009). An electrical method for the measurement of the thermal and electrical conductivity of reduced

graphene oxide nanostructures. *Nanotechnology, 20*(40), 405704. doi:10.1088/0957-4484/20/40/405704

Seger, B., & Kamat, P. V. (2009). Electrocatalytically active graphene-platinum nanocomposites. role of 2-D carbon support in PEM fuel cells. *The Journal of Physical Chemistry C, 113*(19), 7990-7995. doi:10.1021/jp900360k

Setyawan, H., & Widiyastuti, W. (2019). Progress in the preparation of magnetite nanoparticles through the electrochemical method. *KONA Powder and Particle Journal*, 2019011.

Shafaei, F., Babaei, S. E., Shahvelayati, A. S., & Honarmand Janatabadi, F. (2019). Biosynthesis of Fe_3O_4-magnetic nanoparticles using clover leaf aqueous extract: Green synthesis of 1, 3-benzoxazole derivatives. *Journal of the Chinese Chemical Society*. doi:https://doi.org/10.1002/jccs.201800489

Shaghaghi, B., Khoee, S., & Bonakdar, S. (2019). Preparation of multifunctional Janus nanoparticles on the basis of SPIONs as targeted drug delivery system. *International journal of pharmaceutics, 559*, 1-12. doi:https://doi.org/10.1016/j.ijpharm.2019.01.020

Shan, G.-b., Xing, J.-m., Luo, M.-f., Liu, H.-z., & Chen, J.-y. (2003). Immobilization of Pseudomonas delafieldii with magnetic polyvinyl alcohol beads and its application in biodesulfurization. *Biotechnology letters, 25*(23), 1977-1981. doi:https://doi.org/10.1023/B:BILE.0000004388.15751.8c

Shen, S., Liu, Y., Wang, F., Yao, G., Xie, L., & Xu, B. (2018). Graphene oxide regulates root development and influences iaa concentration in rice. *Journal of Plant Growth Regulation V 38*(1), 241-248. doi:https://doi.org/10.1007/s00344-018-9836-5

Shen, Z., Wu, A., & Chen, X. (2016). Iron oxide nanoparticle based contrast agents for magnetic resonance imaging. *Molecular Pharmaceutics, 14*(5), 1352-1364. doi:https://doi.org/10.1021/acs.molpharmaceut.6b00839

Shi, D., Bedford, N. M., & Cho, H.-S. (2011). Engineered multifunctional nanocarriers for cancer diagnosis and therapeutics. *Small, 7*(18), 2549-2567. doi:10.1002/smll.201100436

Shi, D., Sadat, M. E., Dunn, A. W., & Mast, D. B. (2015). Photo-fluorescent and magnetic properties of iron oxide nanoparticles for biomedical applications. *Nanoscale, 7*(18), 8209-8232. doi:10.1039/C5NR01538C

Silva, V., Andrade, P., Silva, M., Valladares, L. D. L. S., & Aguiar, J. A. (2013). Synthesis and characterization of Fe_3O_4 nanoparticles coated with fucan polysaccharides. *Journal of Magnetism and Magnetic Materials, 343*, 138-143. doi:https://doi.org/10.1016/j.jmmm.2013.04.062

Skumiel, A., Kaczmarek, K., Flak, D., Rajnak, M., Antal, I., & Brząkała, H. (2020). The influence of magnetic nanoparticle concentration with dextran polymers in agar gel on heating efficiency in magnetic hyperthermia. *Journal of Molecular Liquids, 304*, 112734. doi:https://doi.org/10.1016/j.molliq.2020.112734

Soetaert, F., Kandala, S. K., Bakuzis, A., & Ivkov, R. (2017). Experimental estimation and analysis of variance of the measured loss power of magnetic nanoparticles. *Scientific reports, 7*(1), 6661. doi:10.1038/s41598-017-07088-w

Soleymani, M., Khalighfard, S., Khodayari, S., Khodayari, H., Kalhori, M. R., Hadjighassem, M. R., . . . Alizadeh, A. M. (2020). Effects of multiple injections on the efficacy and cytotoxicity of folate-targeted magnetite nanoparticles as theranostic agents for MRI detection and magnetic hyperthermia therapy of tumor cells. *Scientific reports, 10*(1). doi:10.1038/s41598-020-58605-3

Soukup, D., Moise, S., Céspedes, E., Dobson, J., & Telling, N. D. (2015). In situ measurement of magnetization relaxation of internalized nanoparticles in live cells. *ACS nano, 9*(1), 231-240. doi:10.1021/nn503888j

Stojanovic, B. D., Dzunuzovic, A. S., & Ilic, N. I. (2018). 17 - Review of methods for the preparation of magnetic metal oxides. In B. D. Stojanovic (Ed.), *Magnetic, Ferroelectric, and Multiferroic Metal Oxides* (pp. 333-359). United States: Elsevier.

Sugumaran, P. J., Liu, X.-L., Herng, T. S., Peng, E., & Ding, J. (2019). Go-functionalized large magnetic iron oxide nanoparticles with enhanced colloidal stability and hyperthermia performance. *ACS applied materials & interfaces, 11*(25), 22703-22713. doi:10.1021/acsami.9b04261

Suk, J. S., Xu, Q., Kim, N., Hanes, J., & Ensign, L. M. (2016). PEGylation as a strategy for improving nanoparticle-based drug and gene delivery. *Advanced Drug Delivery Reviews, 99*, 28-51. doi:https://doi.org/10.1016/j.addr.2015.09.012

Sun, J., Zhou, S., Hou, P., Yang, Y., Weng, J., Li, X., & Li, M. (2007). Synthesis and characterization of biocompatible Fe_3O_4 nanoparticles. *Journal of biomedical materials research Part A, 80*(2), 333-341. doi:https://doi.org/10.1002/jbm.a.30909

Sun, X., Liu, Z., Welsher, K., Robinson, J. T., Goodwin, A., Zaric, S., & Dai, H. (2008). Nano-graphene oxide for cellular imaging and drug delivery. *Nano Research, 1*(3), 203-212. doi:10.1007/s12274-008-8021-8

Syed, I., Garg, S., & Sarkar, P. (2018). 5 - Entrapment of essential oils in hydrogels for biomedical applications. In K. Pal & I. Banerjee (Eds.), *Polymeric Gels* (pp. 125-141). Cambridge, United Kingdom: Woodhead Publishing.

Szabó, T., Tombácz, E., Illés, E., & Dékány, I. (2006). Enhanced acidity and pH-dependent surface charge characterization of successively oxidized graphite oxides. *Carbon, 44*(3), 537-545. doi:https://doi.org/10.1016/j.carbon.2005.08.005

Tai, M. F., Lai, C. W., & Abdul Hamid, S. B. (2016). Facile synthesis polyethylene glycol coated magnetite nanoparticles for high colloidal stability. *Journal of Nanomaterials, 2016*, 7. doi:10.1155/2016/8612505

Tan, Y., Zhuang, Z., Peng, Q., & Li, Y. (2008). Room-temperature soft magnetic iron oxide nanocrystals: synthesis, characterization, and size-dependent magnetic properties. *Chemistry of Materials, 20*(15), 5029-5034. doi:10.1021/cm801082p

Tang, L.-S., Yang, J., Bao, R.-Y., Liu, Z.-Y., Xie, B.-H., Yang, M.-B., & Yang, W. (2017). Polyethylene glycol/graphene oxide aerogel shape-stabilized phase change materials for photo-to-thermal energy conversion and storage via tuning the oxidation degree of graphene oxide. *Energy Conversion and Management, 146*, 253-264. doi:https://doi.org/10.1016/j.enconman.2017.05.037

Thalib, N. B., Mustapha, S. N. H., Feng, C. K., & Mustapha, R. (2020). Tailoring graphene reinforced thermoset and biothermoset composites. *Reviews in Chemical Engineering, 36*(5), 623-652. doi:https://doi.org/10.1515/revce-2017-0091

Tiwari, A., Verma, N. C., Turkkan, S., Debnath, A., Singh, A., Draeger, G., . . . Randhawa, J. K. (2020). Graphitic carbon coated magnetite nanoparticles for dual mode imaging and hyperthermia. *ACS Applied Nano Materials, 3*(1), 896-904. doi:10.1021/acsanm.9b02501

Tuček, J., Sofer, Z., Bouša, D., Pumera, M., Holá, K., Malá, A., . . . Zbořil, R. (2016). Air-stable superparamagnetic metal nanoparticles entrapped in graphene oxide matrix. *Nature communications, 7*(1), 12879. doi:10.1038/ncomms12879

Unsoy, G., Gunduz, U., Oprea, O., Ficai, D., Sonmez, M., Radulescu, M., . . . Ficai, A. (2015). Magnetite: from synthesis to applications. *Current topics in medicinal chemistry, 15*(16), 1622-1640.

Upadhyay, R. K., Soin, N., & Roy, S. S. (2014). Role of graphene/metal oxide composites as photocatalysts, adsorbents and disinfectants in water treatment: a review. *Rsc Advances, 4*(8), 3823-3851. doi:https://doi.org/10.1039/C3RA45013A

Urtizberea, A., Natividad, E., Arizaga, A., Castro, M., & Mediano, A. (2010). Specific absorption rates and magnetic properties of ferrofluids with interaction effects at low concentrations. *The Journal of Physical Chemistry C, 114*(11), 4916-4922. doi:10.1021/jp912076f

Vayssieres, L., Chanéac, C., Tronc, E., & Jolivet, J. P. (1998). Size tailoring of magnetite particles formed by aqueous precipitation: an example of thermodynamic stability of nanometric oxide particles. *Journal of colloid and interface science, 205*(2), 205-212. doi:https://doi.org/10.1006/jcis.1998.5614

Wang, G., Zhao, D., Ma, Y., Zhang, Z., Che, H., Mu, J., . . . Zhang, Z. (2018). Synthesis and characterization of polymer-coated manganese ferrite nanoparticles as controlled drug delivery. *Applied Surface Science, 428*, 258-263. doi:https://doi.org/10.1016/j.apsusc.2017.09.096

Wang, J.-W., Zhang, Y.-N., Sze, S., van de Weg, S., Vernooij, F., Schoneveld, A., . . . Lam, C. (2018). Lowering low-density lipoprotein particles in plasma using dextran sulphate co-precipitates procoagulant extracellular vesicles. *International journal of molecular sciences, 19*(1), 94. doi:https://doi.org/10.3390/ijms19010094

Wang, N., Zhu, L., Wang, D., Wang, M., Lin, Z., & Tang, H. (2010). Sono-assisted preparation of highly-efficient peroxidase-like Fe_3O_4 magnetic nanoparticles for

catalytic removal of organic pollutants with H_2O_2. *Ultrasonics Sonochemistry, 17*(3), 526-533. doi:https://doi.org/10.1016/j.ultsonch.2009.11.001

Wild, C., Weiderpass, E., & Stewart, B. (2020). World cancer report: cancer research for cancer prevention. *World Cancer Reports. Lyon: International Agency for Research on Cancer*.

Wildeboer, R., Southern, P., & Pankhurst, Q. (2014). On the reliable measurement of specific absorption rates and intrinsic loss parameters in magnetic hyperthermia materials. *Journal of Physics D: Applied Physics, 47*(49), 495003. doi:https://doi.org/10.1088/0022-3727/47/49/495003

Wu, X., Sprinkle, M., Li, X., Ming, F., Berger, C., & de Heer, W. A. (2008). Epitaxial-Graphene/Graphene-Oxide Junction: An Essential Step towards Epitaxial Graphene Electronics. *Physical Review Letters, 101*(2), 026801. doi:10.1103/PhysRevLett.101.026801

Wu, X., Xu, G., & Zhu, J.-J. (2019). Sonochemical synthesis of Fe_3O_4/carbon nanotubes using low frequency ultrasonic devices and their performance for heterogeneous sono-persulfate process on inactivation of Microcystis aeruginosa. *Ultrasonics Sonochemistry, 58*, 104634. doi:https://doi.org/10.1016/j.ultsonch.2019.104634

Wust, P., Hildebrandt, B., Sreenivasa, G., Rau, B., Gellermann, J., Riess, H., . . . Schlag, P. M. (2002). Hyperthermia in combined treatment of cancer. *The Lancet Oncology, 3*(8), 487-497. doi:https://doi.org/10.1016/S1470-2045(02)00818-5

Xie, P., Du, P., Li, J., & Liu, P. (2019). Stimuli-responsive hybrid cluster bombs of PEGylated chitosan encapsulated DOX-loaded superparamagnetic nanoparticles enabling tumor-specific disassembly for on-demand drug delivery and enhanced MR imaging. *Carbohydrate polymers, 205*, 377-384. doi:https://doi.org/10.1016/j.carbpol.2018.10.076

Xu, Z., Peng, L., Liu, Y., Liu, Z., Sun, H., Gao, W., & Gao, C. (2016). Experimental guidance to graphene macroscopic wet-spun fibers, continuous papers, and ultralightweight aerogels. *Chemistry of Materials, 29*(1), 319-330. doi:https://doi.org/10.1021/acs.chemmater.6b02882

Xue, G., Zhong, J., Gao, S., & Wang, B. (2016). Correlation between the free volume and thermal conductivity of porous poly(vinyl alcohol)/reduced graphene oxide composites studied by positron spectroscopy. *Carbon, 96*, 871-878. doi:https://doi.org/10.1016/j.carbon.2015.10.041

Yamaura, M., Camilo, R. L., Sampaio, L. C., Macêdo, M. A., Nakamura, M., & Toma, H. E. (2004). Preparation and characterization of (3-aminopropyl)triethoxysilane-coated magnetite nanoparticles. *Journal of Magnetism and Magnetic Materials, 279*(2), 210-217. doi:https://doi.org/10.1016/j.jmmm.2004.01.094

Yang, D., Velamakanni, A., Bozoklu, G., Park, S., Stoller, M., Piner, R. D., . . . Ruoff, R. S. (2009). Chemical analysis of graphene oxide films after heat and chemical treatments by X-ray photoelectron and Micro-Raman spectroscopy. *Carbon, 47*(1), 145-152. doi:https://doi.org/10.1016/j.carbon.2008.09.045

Yang, J., Zou, P., Yang, L., Cao, J., Sun, Y., Han, D., . . . Wang, B. (2014). A comprehensive study on the synthesis and paramagnetic properties of PEG-coated Fe_3O_4 nanoparticles. *Applied Surface Science, 303*, 425-432. doi:https://doi.org/10.1016/j.apsusc.2014.03.018

Yang, X., Yang, K., Wu, L., Yang, J., & He, Y. (2020). Fe_3O_4 nanoparticles functionalized with poly(ethylene glycol) for the selective separation and enrichment of Au(iii). *New Journal of Chemistry, 44*(4), 1313-1319. doi:10.1039/C9NJ05551G

Yang, Y., Cao, J., Wei, N., Meng, D., Wang, L., Ren, G., . . . Zhang, N. (2019). Thermal conductivity of defective graphene oxide: a molecular dynamic study. *Molecules, 24*(6), 1103. doi:https://doi.org/10.3390/molecules24061103

Yang, Y., Huang, M., Qian, J., Gao, D., & Liang, X. (2020). Tunable Fe_3O_4 nanorods for enhanced magnetic hyperthermia performance. *Scientific reports, 10*(1). doi:10.1038/s41598-020-65095-w

Yin, P. T., Shah, S., Chhowalla, M., & Lee, K.-B. (2015). Design, synthesis, and characterization of graphene–nanoparticle hybrid materials for bioapplications. *Chemical Reviews, 115*(7), 2483-2531. doi:10.1021/cr500537t

You, L., Liu, X., Fang, Z., Xu, Q., & Zhang, Q. (2019). Synthesis of multifunctional Fe_3O_4@ PGA-PEG nano-niosomes as a targeting carrier for treatment of cervical cancer. *Materials Science and Engineering: C, 94*, 291-302. doi:https://doi.org/10.1016/j.msec.2018.09.044

Yu, X., Yang, R., Wu, C., Zhang, W., Deng, D., Zhang, X., & Li, Y. (2020). *The Preparation of Smart Magnetic Nanoparticles for Intracellular Hyperthermia*, Singapore.

Zahedi, E., Ansari, S., Wu, B. M., Bencharit, S., & Moshaverinia, A. (2017). 4 - Hydrogels in craniofacial tissue engineering. In L. Tayebi & K. Moharamzadeh (Eds.), *Biomaterials for oral and dental tissue engineering* (pp. 47-64). Cambridge, United Kingdom: Woodhead Publishing.

Zandiatashbar, A., Lee, G.-H., An, S. J., Lee, S., Mathew, N., Terrones, M., . . . Koratkar, N. (2014). Effect of defects on the intrinsic strength and stiffness of graphene. *Nature communications, 5*(1), 3186. doi:10.1038/ncomms4186

Zhang, H., Fonseca, A. F., & Cho, K. (2014). Tailoring Thermal Transport Property of Graphene through Oxygen Functionalization. *The Journal of Physical Chemistry C, 118*(3), 1436-1442. doi:10.1021/jp4096369

Zhang, L., Xia, J., Zhao, Q., Liu, L., & Zhang, Z. (2010). Functional graphene oxide as a nanocarrier for controlled loading and targeted delivery of mixed anticancer drugs. *Small, 6*(4), 537-544. doi:10.1002/smll.200901680

Zhang, Q., Liu, J., Yuan, K., Zhang, Z., Zhang, X., & Fang, X. (2017). A multi-controlled drug delivery system based on magnetic mesoporous Fe_3O_4 nanopaticles and a phase change material for cancer thermo-chemotherapy. *Nanotechnology, 28*(40), 405101. doi:https://doi.org/10.1088/1361-6528/aa883f

Zhang, Q., Wu, Z., Li, N., Pu, Y., Wang, B., Zhang, T., & Tao, J. (2017). Advanced review of graphene-based nanomaterials in drug delivery systems: Synthesis, modification, toxicity and application. *Materials Science and Engineering: C, 77*, 1363-1375. doi:https://doi.org/10.1016/j.msec.2017.03.196

Zhang, X.-F., Liu, Z.-G., Shen, W., & Gurunathan, S. (2016). Silver nanoparticles: synthesis, characterization, properties, applications, and therapeutic approaches. *International journal of molecular sciences, 17*(9), 1534. doi:10.3390/ijms17091534

Zhao, D.-L., Zeng, X.-W., Xia, Q.-S., & Tang, J.-T. (2009). Preparation and coercivity and saturation magnetization dependence of inductive heating property of Fe_3O_4 nanoparticles in an alternating current magnetic field for localized hyperthermia. *Journal of Alloys and Compounds, 469*(1), 215-218. doi:https://doi.org/10.1016/j.jallcom.2008.01.083

Zhou, H., Belzile, O., Zhang, Z., Wagner, J., Ahn, C., Richardson, J. A., . . . Mason, R. P. (2019). The effect of flow on blood oxygen level dependent (R^*_2) MRI of orthotopic lung tumors. *Magnetic resonance in medicine, 81*(6), 3787-3797. doi:https://doi.org/10.1002/mrm.27661

Zhou, Q., Feng, F., Yang, Y., Zhao, F., Du, R., Zhou, Z., & Han, Y. (2018). Characterization of a dextran produced by Leuconostoc pseudomesenteroides XG5 from homemade wine. *International journal of biological macromolecules, 107*, 2234-2241. doi:https://doi.org/10.1016/j.ijbiomac.2017.10.098

Zhu, M., Lerum, M. Z., & Chen, W. (2012). How to prepare reproducible, homogeneous, and hydrolytically stable aminosilane-derived layers on silica. *Langmuir, 28*(1), 416-423. doi:10.1021/la203638g

Zhu, Q., Bao, B., Zhang, Q., Yu, J., & Lu, W. (2018). Maleimidation of dextran and the application in designing a dextran–camptothecin conjugate. *Rsc Advances, 8*(5), 2818-2823. doi:https://doi.org/10.1039/C7RA12954H

Zubir, N. A., Yacou, C., Motuzas, J., Zhang, X., & Diniz da Costa, J. C. (2014). Structural and functional investigation of graphene oxide–Fe_3O_4 nanocomposites for the heterogeneous Fenton-like reaction. *Scientific reports, 4*, 4594. doi:10.1038/srep04594

Zuo, X., Wu, C., Zhang, W., & Gao, W. (2018). Magnetic carbon nanotubes for self-regulating temperature hyperthermia. *Rsc Advances, 8*(22), 11997-12003. doi:10.1039/C7RA13256E

Zupančič Valant, A., Žiberna, L., Papaharilaou, Y., Anayiotos, A., & Georgiou, G. C. (2011). The influence of temperature on rheological properties of blood mixtures with different volume expanders—implications in numerical arterial hemodynamics simulations. *Rheologica Acta, 50*(4), 389-402. doi:10.1007/s00397-010-0518-x